

DE81023795

Final Report

on

Iron-Induced Deactivation of Supported  
Nickel Methanation Catalysts

Department of Energy/Fossil Energy Program  
University Coal Conversion Research Award - 1978

Contract No. ET-78-G-01-3380

James A. Dumesic/Principal Investigator  
Department of Chemical Engineering  
University of Wisconsin  
Madison, Wisconsin 53706

**DISCLAIMER**  
This report was prepared as an account of work sponsored by an agency of the United States Government. It is the policy of the United States Government neither to recommend nor to endorse the views or conclusions expressed herein, nor to assume any liability for the results therefrom, or to ensure that the information contained herein is accurate or complete. It is the policy of the United States Government not to distribute copies of this report to other than the individual or organization to whom it is specifically addressed. It is the policy of the United States Government not to distribute copies of this report to other than the individual or organization to whom it is specifically addressed. It is the policy of the United States Government not to distribute copies of this report to other than the individual or organization to whom it is specifically addressed. It is the policy of the United States Government not to distribute copies of this report to other than the individual or organization to whom it is specifically addressed.

FB 21-78 ET 12248



### ABSTRACT

A high pressure vessel has been tested and shown to be effective for the simultaneous collection of methanation kinetics and in situ Mössbauer spectra. Using this cell, the deactivation of an alumina-supported nickel catalyst ( $\text{Ni}/\text{Al}_2\text{O}_3$ ) was studied before, during and after the dosing of  $\text{Fe}(\text{CO})_5$  onto the sample under methanation reaction conditions. This iron-induced deactivation was initiated by passing CO at high pressure (4 MPa) over an iron catalyst (at 473 K) for the in situ production of  $\text{Fe}(\text{CO})_5$ , followed by mixing the CO with  $\text{H}_2$  and passing this synthesis gas mixture over the  $\text{Ni}/\text{Al}_2\text{O}_3$  catalyst at temperatures and pressures near 620 K and 0.2 MPa. The Mössbauer spectra collected under these methanation reaction conditions (with  $\text{H}_2/\text{CO}$  partial pressure ratios near 10) showed the iron on  $\text{Ni}/\text{Al}_2\text{O}_3$  to be present as an iron carbide. Treatment in hydrogen of the iron-deactivated catalyst at 620 K gave rise to a Mössbauer spectrum characteristic of metallic iron, indicating that the iron on  $\text{Ni}/\text{Al}_2\text{O}_3$  is not in direct contact with nickel (i.e. an FeNi alloy is not formed nor does iron form a monolayer coating over nickel crystallites). Furthermore, for Fe/Ni atomic ratios of approximately 0.03, the methanation kinetics over an iron-deactivated  $\text{Ni}/\text{Al}_2\text{O}_3$  catalyst approached those characteristic of iron alone. This sensitivity of the methanation kinetics to small amounts of iron, combined with the observation that iron and nickel are not in direct contact, indicates that iron deactivates supported nickel catalysts by depositing in and blocking the pore mouths of the support.

Magnetic relaxation phenomena in the Mössbauer spectra of iron-deactivated  $\text{Ni}/\text{Al}_2\text{O}_3$  were used to estimate the average

p

size of the iron particles as 7 nm. This size is comparable to the 15 nm average pore diameter of the alumina support. This pore mouth blocking may be made more severe by the propensity for iron to produce carbon deposits. In addition, it is found that these iron particles and defect sites on carbon may serve as nucleation centers for further decomposition of  $\text{Fe}(\text{CO})_5$ . This leads to continued deposition of iron in the pore mouths of the support; exacerbating the problem of iron-induced deactivation of nickel methanation catalysts.

TABLE OF CONTENTS

- I. Mössbauer Spectroscopy Cell for in situ Catalyst  
Characterization and Reaction Kinetics Studies at  
High Pressures
- I.A. Introduction
  - I.B. Apparatus
    - I.B.1. The High-Pressure Cell
    - I.B.2. The Prereactor and Postreactor
  - I.C. Performance
  - I.D. References
- II. Deactivation Studies of Ni/Al<sub>2</sub>O<sub>3</sub> Methanation Catalysts
- II.A. Experimental
  - II.B. Results
  - II.C. Discussion
  - II.D. Conclusions
  - II.E. References
- III. Appendix A. Criteria for Stable Ni Particle Size under  
Methanation Reaction Conditions: Nickel Transport and  
Particle Size Growth via Nickel Carbonyl
- III.A. Experimental
    - III.A.1. High Pressure Reaction System
    - III.A.2. Particle Size Determinations
    - III.A.3. Catalyst Preparation and Treatment
  - III.B. Results
  - III.C. Discussion
    - III.C.1. Nickel Transportation and Particle Size Growth
    - III.C.2. Kinetic and Thermodynamic Aspects of Ni(CO)<sub>4</sub>  
Formation
    - III.C.3. Blockage of Surface Sites
    - III.C.4. Methanation Kinetics

III.D. Conclusions

III.E. References

IV. Appendix B. Iron Pentacarbonyl Decomposition over Grafoil:

I. Production of Small Metallic Iron Particles

IV.A. Experimental

IV.A.1. Iron Pentacarbonyl Handling

IV.A.2. Mössbauer Spectroscopy

IV.A.3. Graphite Sample

IV.B. Results

IV.C. Discussion

IV.C.1. Fe(CO)<sub>5</sub> Adsorbed on Graphite - Spectrum 1

IV.C.2. Interaction of Metallic Iron with Graphite - Spectra 2, 3, and 4

IV.C.2.a. Active Sites on Graphite

IV.C.2.b. Orientation of Iron Particles on Graphite

IV.C.2.c. Particle Sintering and Possible Carbide Formation

IV.C.3. Quantitative Spectral Analysis - Spectra 2 and 3

IV.C.3.a. Relaxation Effects

IV.C.3.b. Hyperfine Field Distribution Effects

IV.C.4. Proposed Iron Morphology

IV.D. References

V. Appendix C. Iron Pentacarbonyl Decomposition over Grafoil:

II. Effect of Sample Outgassing on Decomposition Kinetics

V.A. Experimental

V.A.1. Graphite Sample

V.A.2. Mössbauer Spectroscopy

V.A.3. Volumetric Gas Phase Measurements

**V.B. Results****V.B.1. Mössbauer Spectroscopy****V.B.2. Volumetric Gas Phase Measurements****V.C. Discussion****V.C.1. Mössbauer Spectroscopy****V.C.2. Volumetric Gas Phase Measurements****V.C.2.a. Metallic Iron Morphology****V.C.2.b. Decomposition Kinetics****V.C.2.c. Effects of Grafoil Outgassing****V.D. Conclusions****V.E. References**

I. Mössbauer Spectroscopy Cell for in situ  
Catalyst Characterization and Reaction  
Kinetics Studies at High Pressures\*

\*Revised from a paper accepted for publication  
in Review of Scientific Instruments

## I.A. INTRODUCTION

The key problem in studying iron-induced deactivation of nickel methanation catalysts is to construct a high pressure vessel that allows methanation kinetics and in situ spectroscopic studies to be conducted on the same sample. Our previous report detailed preliminary data from such a high pressure Mössbauer spectroscopy cell. It has been found more recently, however, that temperature measurement in such a cell is critical when studying an exothermic reaction such as methanation. Yet, it is essential to be able to collect accurate kinetic data in this cell, since the objective of the present study is to relate catalyst deactivation to the information contained in the Mössbauer spectrum. For this reason, we have spent considerable time modifying the design of the Mössbauer spectroscopy cell. It should be noted that this is the first high pressure Mössbauer spectroscopy cell ever constructed for reaction kinetics studies. A detailed description of this cell is presented below.

Several designs of Mössbauer spectroscopy cells for in situ catalyst characterization have been described elsewhere (1-6). However, these cells cannot be used at pressures significantly higher than atmospheric pressure. Furthermore, the geometries involved allow the reactant gas mixture to flow over, but not through, a thin layer of catalyst or a catalyst wafer. The existence of a bulk gas phase concentration gradient in the direction perpendicular to the catalyst layer or wafer is very probable for these configurations. In this respect, the present study involved the construction of a simple Mössbauer spectroscopy cell that provides (i) the capability of operating at pressures up to 6.8 MPa and temperatures up to 773 K, and (ii) a flow arrangement



which allows a reactant gas mixture to flow downwards through the catalyst bed at a rate which minimizes gas phase concentration gradients. In addition, this cell facilitates studies of different layers of catalyst in a packed bed reactor. In this application, the cell is used in tandem with a "prereactor" and/or a "postreactor."

## I.B. APPARATUS

### I.B.1. The High-Pressure Cell

A schematic diagram of the high-pressure Mössbauer spectroscopy cell is shown in Figure 1. The cell is designed to operate with a vertical  $\gamma$ -ray beam. The cell body is constructed of 2.54 cm OD x 2.06 cm ID 316 stainless steel tubing. The ends of this tubing were welded to ConFlat flanges (Varian #954-5067). The use of type 316 stainless steel eliminates the formation of  $\text{Fe}(\text{CO})_5$  and minimizes the formation of  $\text{Ni}(\text{CO})_4$  at high carbon monoxide partial pressures (7). The upper portion of the cell was bored to create a seat for a quartz basket in which the catalyst was held. This basket was made of a 7.0 cm length of quartz tube with an outer diameter which was slightly smaller than the inner diameter of the bored stainless steel tubing but larger than the inner diameter of the original stainless steel tubing. Figure 2 is a photograph of this quartz basket (with the thermocouple used to measure the temperature of the catalyst bed, as discussed later). The upper 5.1 cm of this quartz tube had one quarter of its periphery cut out so that it would not block the flow of gases into the cell. At the lower end of the basket a coarse screen was fashioned from two mutually perpendicular sets of two parallel quartz rods, fastened to

one another and to the quartz tube. The diameter of these rods (1-2 mm) was kept small in order to maximize the open area for  $\gamma$ -ray transmission through the quartz screen. A thin layer of pressed quartz wool, upon which catalyst powder of interest can be evenly distributed, was then placed on the quartz screen. Two small holes in the wall of the upper portion of the basket facilitated its removal from the high pressure cell at the end of each experiment. A quartz hook was attached beneath each of these holes to fix the position of the thermocouple used to measure the temperature of the catalyst bed (see Figure 2). Two pieces of 0.64 cm OD 316 stainless steel tubing were welded to the cell body to provide for entrance and exit of reactant gases. The gas enters the cell through the upper tube, and the reactor operates with down-flow of gas through the catalyst sample. Heating of the cell is accomplished by passing electrical current through #25 Nichrome wire, with an overall resistance of 15.5  $\Omega$  at room temperature, wound around the cell in a manner such that no magnetic field was created in the cell during passage of current. This was done by folding the wire at its midpoint and wrapping the two halves around the cell in parallel with one another. An iron/constantan thermocouple was welded to the outer cell wall for cell temperature measurement and control. In addition, a flexible chromel/constantan thermocouple was introduced into the cell through a tee (Swagelok) in the gas entrance tube, wound around the hooks on the quartz tube, and then placed in direct contact with the catalyst powder. The pressure seal for introduction of this thermocouple through a

piece of 0.32 cm OD tubing into the tee in the gas entrance tube was made using a high strength epoxy (Devcon F). This thermocouple measures the temperature of the catalyst bed under reaction conditions.

Beryllium discs, mounted on ConFlat flanges, serve as  $\gamma$ -ray transparent windows when bolted onto the top and bottom of the Mössbauer spectroscopy cell. These Be discs (HIP-50) were supplied by Kawecki Berylco Industries, Inc. They were 3.48 cm in diameter and 0.23 cm thick. This thickness was chosen to provide high  $\gamma$ -ray transmission, yet allow high pressure operation. (The thickness was calculated using tabulated equations (8), mechanical properties of HIP-50 (9) and a safety factor of 2.) Indeed, the upper limit on the pressure at which the cell can be operated is set by the strength of the beryllium windows. The strength of the windows depends not only on the type and thickness of the material used, but also on the method used for mounting the beryllium windows. Good mechanical strength was achieved using HIP-50 beryllium, electron beam welded by Electrofusion Co. to ConFlat flanges. An aluminum/stainless steel transition ring between the beryllium disc and the ConFlat flange is required by the welding process, and standard copper gaskets are used for sealing the ConFlat flanges to the body of the cell. It should be noted that HIP-50 beryllium contains 600 ppm of iron impurity. The contribution of this iron to the Mössbauer spectrum will be discussed later.

Before sealing the Be window (with its associated ConFlat flange) to the Mössbauer spectroscopy cell, a thin (ca. 0.1 mm

thick) Kapton film (DuPont 500 F131) was placed between the copper gasket and the ConFlat flange welded to the cell body. The two flanges were then bolted together. Once the cell is pressurized, the Kapton film is sealed against the copper gasket thereby preventing any condensable component from reaching the beryllium window. This avoids the problems associated with cleaning the Be windows following studies of catalytic reactions involving species that may condense or deposit on the windows. Finally, the temperature of the Be windows can be regulated using two turns of water-cooled copper tubing at each end of the cell. Square copper tubing (0.64 cm each side, 0.32 cm ID), rather than round copper tubing, was used to provide larger contacting area between the copper cooling coil and the cell body. The tubings were mechanically wound around the ends of the cell.

#### I.B.2. The Prereactor and Postreactor

A prereactor and a postreactor were mounted on the Mössbauer spectroscopy cell inlet and outlet, respectively. These two reactors are identical and are made of 316 stainless steel tubing, 1.27 cm OD and 7.62 cm in length. They were connected to the Mössbauer spectroscopy cell using Swagelok fittings. To keep the catalyst powder in place within each reactor, pieces of 200 mesh screen were placed between the ends of the tubing and the Swagelok fittings. An iron/constantan thermocouple, soldered to the tip of a 0.32 cm OD thermocouple well, was placed at the center of the reactor through the reactor wall. The prereactor is located about 10 cm upstream of the Mössbauer spectroscopy cell, while the

postreactor is located about 10 cm downstream. This arrangement allows the relative amounts of catalyst in the prereactor and postreactor to be varied, while keeping constant the total amount of catalyst in both reactors plus the Mössbauer spectroscopy cell. In this way, Mössbauer spectroscopy studies of the longitudinal variation of catalyst states in a packed catalyst bed are made possible.

The addition of these two reactors to the Mössbauer spectroscopy cell allows one to vary over a wide range the reactant space velocity (i.e. reactant volumetric flow rate divided by weight of catalyst bed) and the extent of reactant conversion (to products) through the entire reactor network. For example, the reactor network can be operated at the low conversions typical of laboratory studies or at the high conversions of interest to industry. In fact, this is done keeping an "optimal" amount of Mössbauer isotope (e.g.  $^{57}\text{Fe}$ ) in the Mössbauer spectroscopy cell. Specifically, too much Mössbauer isotope in the cell results in broad spectral features that complicate data analysis (2).

#### I.C. PERFORMANCE

The ultimate pressure limit of the beryllium windows has not been studied, but the windows have passed static pressure tests at 6.8 MPa and 773 K carried out at Electrofusion Co. Cooling water flowing through the cooling coils at the ends of the Mössbauer spectroscopy cell was effective in keeping the beryllium windows at temperatures below 353 K even when the cell body was maintained at a temperature as high as 656 K. The thin

layer of pressed quartz wool in the quartz catalyst basket is capable of holding catalyst powder in this down-flow design. No powder was observed on the lower beryllium window after the experiments. The maximum temperature at which the cell can be operated is determined by the maximum electric current that the Nichrome wire winding can carry (ca. 4.5 A). The cell has never been operated at its limit. However, it is known that the cell can be heated to 1038 K with a power input of 200 W.

The high content of iron impurities in the beryllium windows (600 ppm) gives rise to a doublet in the Mössbauer spectrum. The computer-fitted quadrupole splitting was 0.576 mm/sec. It agrees with the published value of 0.58 mm/sec for an iron in beryllium solution (10). The peak positions, widths and dips were essentially constant in runs for which the temperature of the empty cell was varied from room temperature to 523 K. Theoretically, such a background correction should require, for example, a second-order Doppler shift adjustment. However, as mentioned earlier, water-cooling was used to keep the temperature of the beryllium windows lower than the cell temperature. The calculated change in isomer shift from room temperature (using the high temperature approximation (10)) is only ca. -0.040 mm/sec when the windows are at 353 K, the maximum temperature observed. The largest measured difference in isomer shifts among blank runs was ca. 0.010 mm/sec. In short, in computer-fitting in situ spectra of iron-containing catalysts at temperatures up to at least 523 K, the contribution from iron impurities in the beryllium windows can be constrained to be the same as that observed during room temperature blank runs of the cell itself.

Mössbauer spectroscopy relies on the well-defined Doppler velocity of the radioactive source with respect to the stationary absorber (i.e. the catalyst in the cell). This makes the Mössbauer spectrum sensitive to any vibrations of the catalyst powder in the Mössbauer spectroscopy cell. To test for such effects, sponge iron powder was studied as a model catalyst in the reactor. In particular, 110 mg of sponge iron powder (with granule sizes 5-32 $\mu$ ) was evenly distributed on the layer of quartz wool in the quartz catalyst basket. Four Mössbauer spectra were then collected in hydrogen under various flow conditions. The spectra are shown in Figure 3. The solid lines indicate computer-fitted absorption peaks. The experimental conditions and results are summarized in Table I. The superficial linear velocities were calculated on the basis of the cross-sectional area of the high pressure cell. Spectrum a was collected under static hydrogen pressure at room temperature. The line widths of this spectrum are used as standards for assessing the extent of catalyst vibration under various flow conditions. This is justified by the absence of both gas flow through the thin catalyst layer and cooling water running through the cooling coils. The line widths of spectra b through d are comparable with (but a little broader than) those of spectrum a. Thus, one may conclude that vibration of catalyst powder in this down-flow arrangement is minimal for the range of flow rates considered.

For catalyst temperature measurement in this cell, it is essential to have a thermocouple in contact with the catalyst bed, as shown for example in Figure 2. In particular, it has

been observed in this cell that the cell-wall temperature (measured by the thermocouple welded to the outer cell wall) can be 40 to 50 K higher than the catalyst temperature (measured by the thermocouple in contact with the catalyst bed) when the catalyst is under high pressure (ca. 1000 kPa) Fischer-Tropsch synthesis conditions (ca. 520 K). It has also been observed that the cell-wall temperature can be 50 K lower than the catalyst temperature when an exothermic reaction, e.g. methanation over a Ni catalyst, is carried out at high conversions. It should be noted that in addition to using a thermocouple in the catalyst bed, one can use the known temperature dependence of the isomer shift and/or the magnetic hyperfine field for well-defined materials (e.g. iron (11), magnetite (12) and copper ferrite (13)) to directly determine the temperature of the catalyst particles themselves. This method is potentially of value in studies of exothermic reactions where small particles of catalytic material may be at temperatures higher than the powdered support whose temperature is measured by the thermocouple immersed in the catalyst bed. The disadvantage of this method, however, is that the chemical state of the Mössbauer isotope in the catalyst under reaction conditions is not known a priori. In general, a temperature reading from a thermocouple in contact with the catalyst bed, in combination with the known temperature dependence of Mössbauer parameters, probably gives the most reliable means of temperature measurement. To conclude this discussion of temperature measurement, it is noted that the



Mössbauer spectra of Figure 3 indicate that significant radial temperature gradients were not present in the layer of catalyst in the quartz basket. A distribution of magnetic hyperfine fields resulting from a nonuniform temperature of the catalyst bed would give rise to a broadening of the Mössbauer spectrum, and this was not observed experimentally (see Figure 3 and Table I). Specifically, it can be calculated that the slightly broader lines of spectrum c, compared to spectrum a, indicate a radial temperature gradient of at most 10 K for the conditions reported in Table I.

Figure 4 shows in situ Mössbauer spectra of a promoted iron catalyst (Harshaw 689A-2-2-6G powder) under high pressure Fischer-Tropsch synthesis conditions. Spectrum a was collected from 0.1 g of catalyst in the Mössbauer spectroscopy cell, while spectrum b was obtained from 0.1 g of catalyst in the cell with 6.8 g of catalyst in the prereactor. For these two spectra, the samples in the Mössbauer spectroscopy cell thus correspond to the top and the bottom portion of a 6.9 g catalyst bed, respectively. The difference in the catalyst states between the top layer and the bottom layer of this iron catalyst bed is easily seen. The catalyst state of the top layer of this promoted iron catalyst bed can be identified as a  $\chi$ -carbide phase (14). The bottom layer of this promoted iron catalyst bed consists of a mixture of magnetite and  $\chi$ -carbide. In other experiments the composition of the bottom layer of the iron catalyst bed was found to depend on the extent of CO conversion.

The capability of this high pressure Mössbauer spectroscopy cell, with pre- and post-reactors, for kinetics studies has been established at both industrially important high conversion levels and research-oriented low conversion levels. As an example of the former application, the data listed in the caption of Figure 4 agree very well with published results from flow-reactors under similar reaction conditions (14). As an example of low-conversion (ca. 5%) data, the methanation kinetics observed over a Ni catalyst in a tubular, high pressure reactor (see Appendix A) have also been reproduced in the high pressure Mössbauer cell (with the pre- and post-reactors empty).

## I.D. REFERENCES

- (1) W.N. Delgass and M. Boudart, *Catal. Rev.* 2, 129 (1968).
- (2) J.A. Dumesic and H. Topsøe, *Adv. Catal.* 26, 121 (1976).
- (3) H. Topsøe, J.A. Dumesic and S. Mørup, in "Application of Mössbauer Spectroscopy" (R.L. Cohen, ed.), Vol. 2, p. 55, Academic Press, (1980).
- (4) P.R. Gray and F.E. Farha, in "Mössbauer Effect Methodology" (I.J. Gruverman and C.W. Seidel, Eds.), Vol. 10, p. 47, Plenum, New York, 1976.
- (5) J.A. Dumesic, Y.V. Maksimov and I.P. Suzdalev, in "Mössbauer Effect Methodology" (I.J. Gruverman and C.W. Seidel, eds.), Vol. 10, p. 31, Plenum, New York, 1976.
- (6) W.N. Delgass, L.Y. Chen and G. Vogel, *Rev. Sci. Instrum.* 47, 968 (1976).
- (7) H. Inouye and J.H. DeVan, *J. Macer. Energy Syst.* 1, 52 (1979).
- (8) W. Griffel, "Handbook of Formulas for Stress and Strain", Chap. 5, P. Ungar Publ. Co., New York, 1966.
- (9) Product data supplied by Kawecki Berylco Industries, Inc., File number 302 i9-PD1, 1977.
- (10) N.N. Greenwood and T.C. Gibb, "Mössbauer Spectroscopy" Chapman & Hall Ltd., London, 1971.
- (11) R.S. Preston, S.S. Hanna and J. Herberle, *Phys. Rev.* 128, 2207 (1962).
- (12) H. Topsøe and M. Boudart, *J. Catal.* 31, 346 (1973).

- (13) B.J. Evans and S.S. Hafner, *J. Phys. Chem. Solids* 29,  
1573 (1968).
- (14) R.J. Madon, E.R. Bucker, and W.F. Taylor, *Final Report*,  
Department of Energy, Contract E(46-1)-8008, July, 1977.

Table I. Results of Test Runs Using Sponge Iron Powder

Spectrum	Pressure (kPa)	H <sub>2</sub> flow rate 1) (liter/min)	Linear velocity (cm/sec)	Temperature (K)	Line width 3) (mm/sec)
a	303	0	0	298	0.347
b	310	0.22	0.83	656	0.374
c	1034	1.00	1.15	616	0.399
d	345	1.50	5.92	530	0.354

1. Referred to standard conditions, i.e. 273 K and atmospheric pressure.
2. Measured by the thermocouple welded to the outer cell wall.
3. Linewidth of the outermost resonant peaks.

## Figure Captions

Fig. 1. The high pressure Mössbauer cell with copper gaskets and Kapton protection films omitted.

- a. Beryllium window
- b. ConFlat flange
- c. Stainless steel to aluminum transition ring
- d. Copper tubing for cooling water
- e. Nichrome heating element
- f. Thermocouple
- g. Quartz catalyst basket
- h. Stainless steel cell body (2.54 cm OD)
- i. Stainless steel tubing (0.64 cm OD)
- j. Holes to facilitate basket removal at the end of each experiment.
- k. Quartz hooks for fixing the position of thermocouple.

Fig. 2. Photograph of quartz catalyst-basket.

Fig. 3. Mössbauer spectra of iron powder under various hydrogen flow conditions. The experimental conditions are summarized in Table I. The central doublet due to the iron impurities in the beryllium windows can be seen in spectrum a. In other spectra, the peak with positive Doppler velocity superimposes on line 4 (counting from left to right) of the iron sextuplet. The solid lines are computer-fitted resonant absorption peaks.

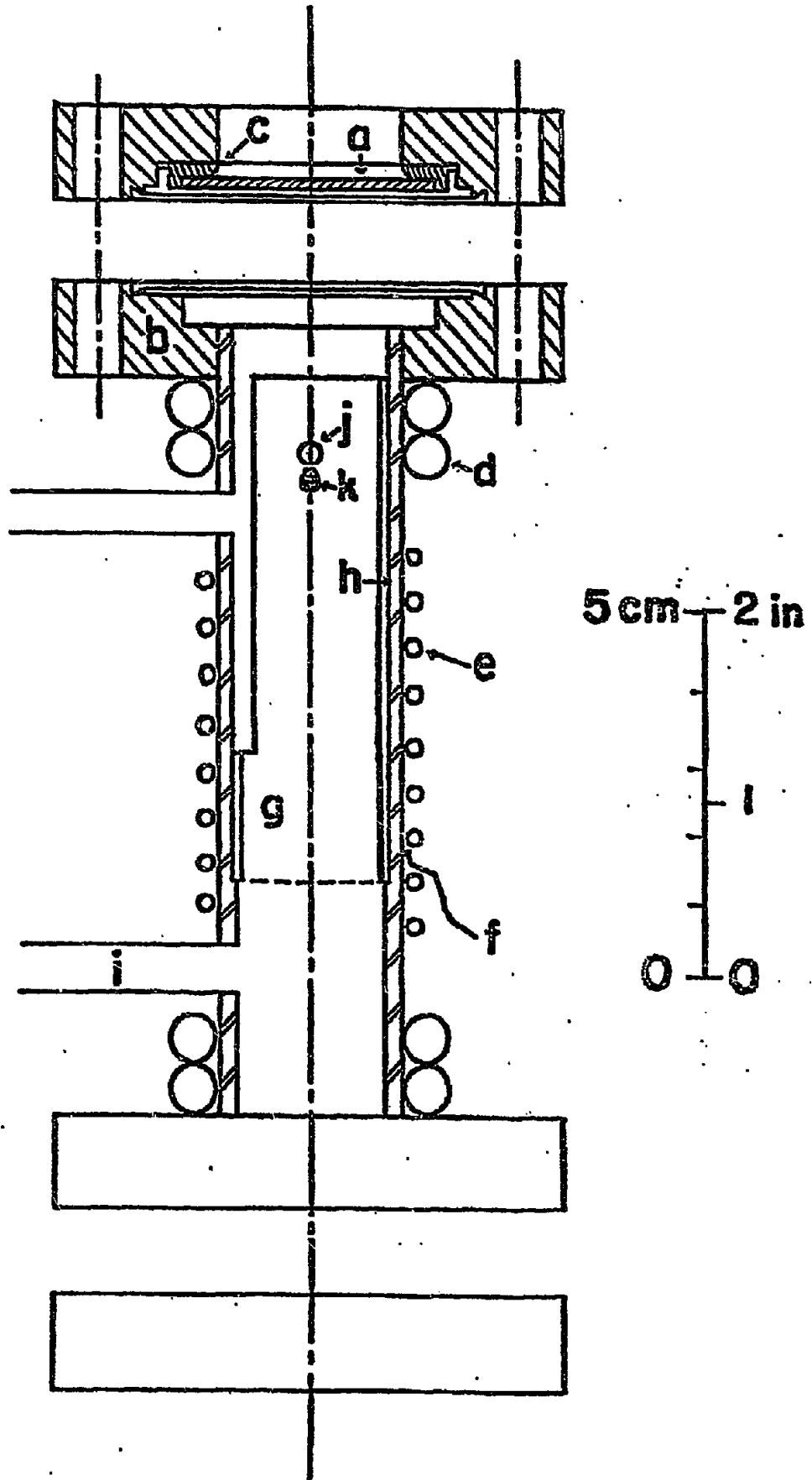
Fig. 4. In situ Mössbauer spectra of an iron-containing Fischer-Tropsch catalyst.

(a) The top layer of the iron catalyst bed.

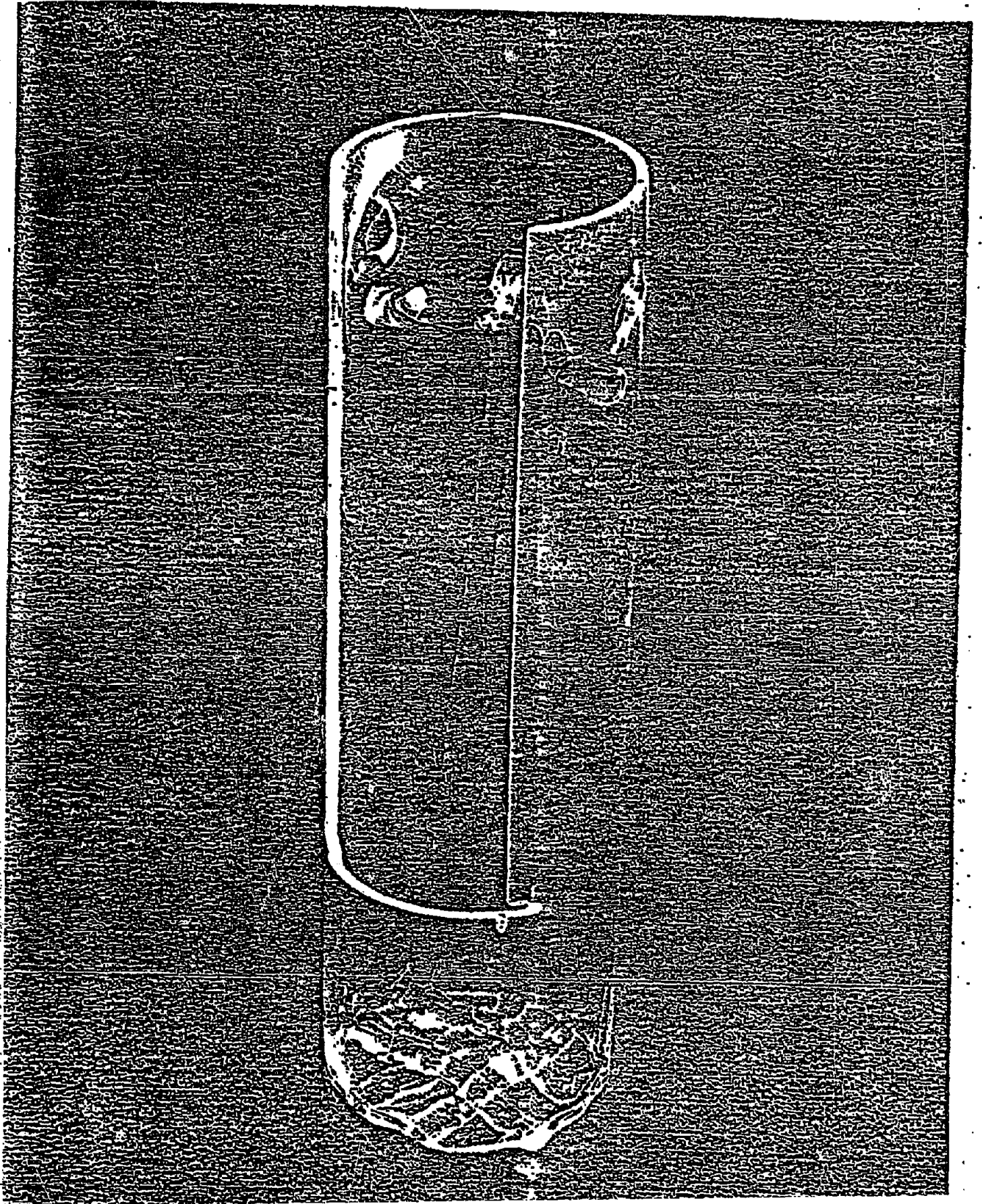
(b) The bottom layer of the iron catalyst bed.

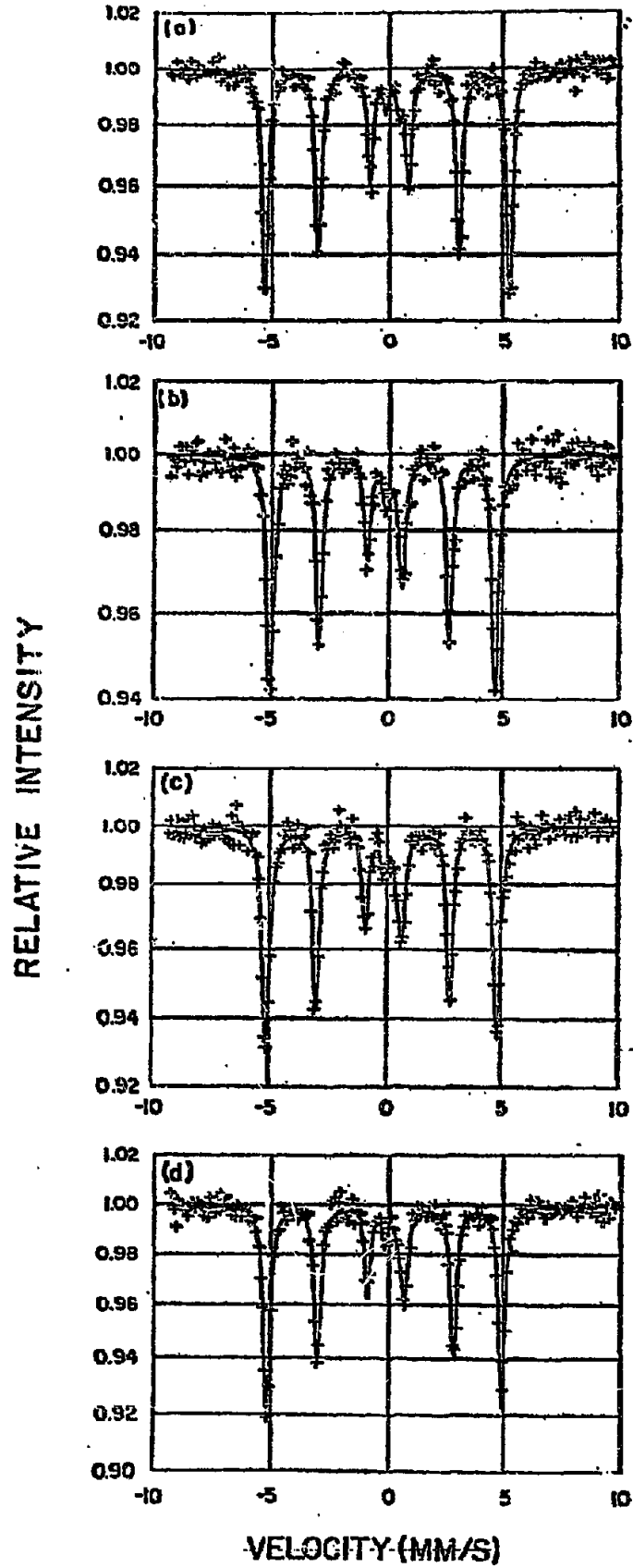
The spectra were collected under the following operating conditions:  $T = 570$  K,  $P = 994$  kPa,  $H_2$  flow rate =  $20$  cm<sup>3</sup>/min, and  $H_2/CO$  ratio = 1.54. These operating conditions resulted in 86.5% CO conversion, and 5.7% and 36.8% selectivities toward  $CH_4$  and  $CO_2$ , respectively. The solid lines are computer-fitted absorption peaks. The computer-fitted peak positions are shown by means of stick diagrams C and D, corresponding to absorption peaks from iron carbide and iron impurities in the beryllium windows, respectively. In spectrum b, A and B designate the tetrahedral and the octahedral sites in a close-packed oxide lattice, respectively.

Fig. 1

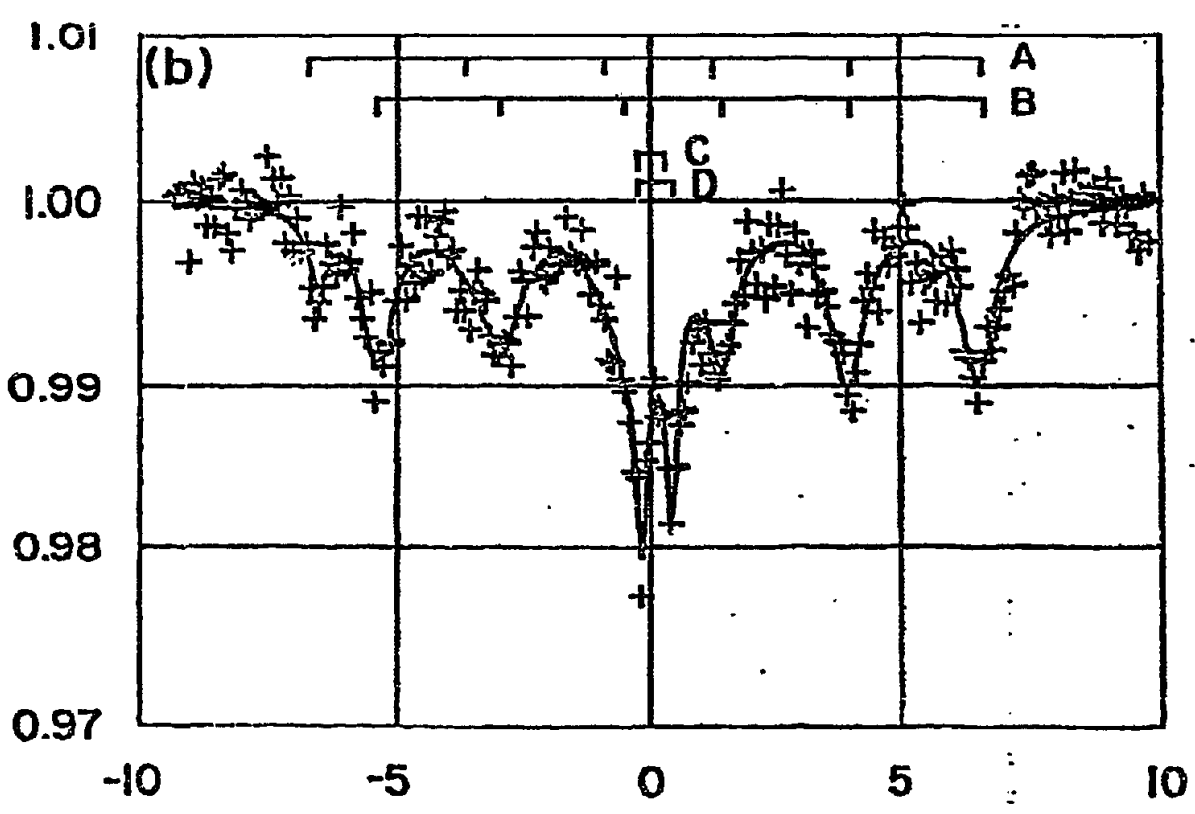
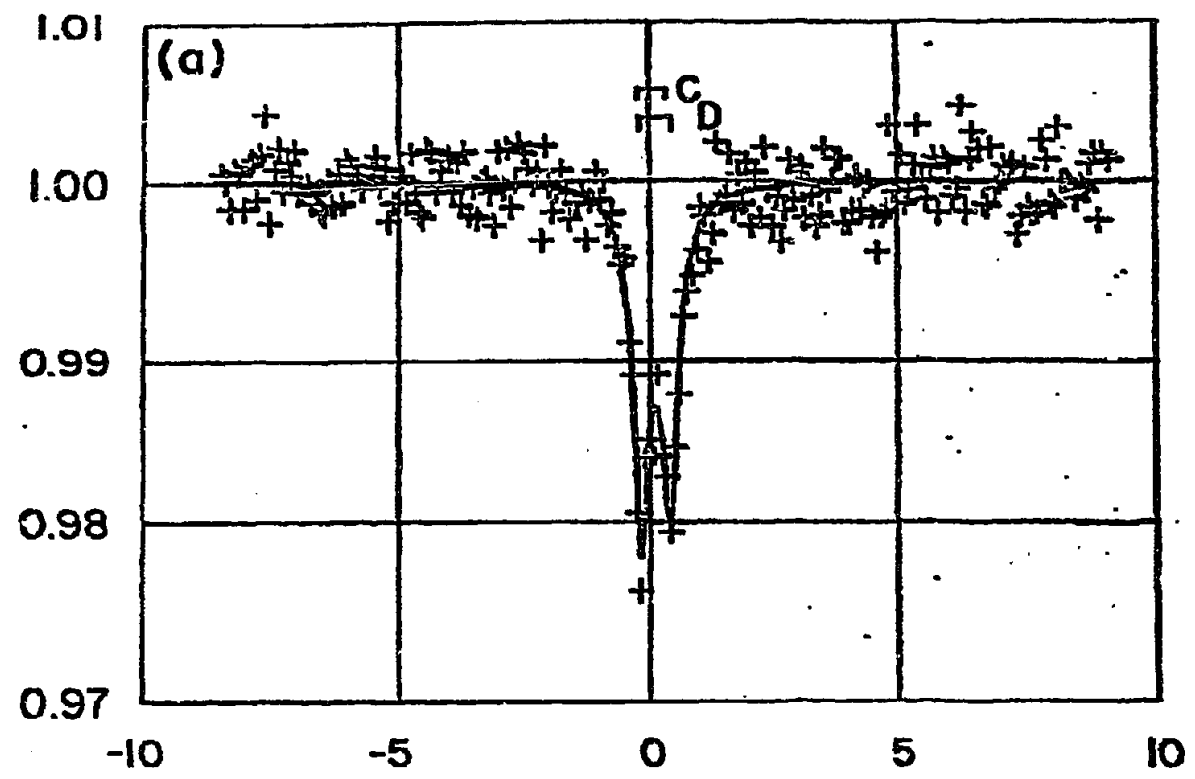








RELATIVE INTENSITY



**II. Deactivation Studies of Ni/Al<sub>2</sub>O<sub>3</sub> Methanation Catalysts**

## II.A. EXPERIMENTAL

The methanation reaction was carried out in the high pressure Mössbauer spectroscopy cell. The design and operation of this cell were described above. After the standard reduction (see Appendix A), the 5.74 wt. % Ni/ $\gamma$ -Al<sub>2</sub>O<sub>3</sub> catalyst was loaded into a quartz cell and sintered by heating it in flowing hydrogen at 1073 K for 14 h. This pretreatment prevented the reaction from igniting while studying kinetics at high temperatures (ca. 623 K). The range of carbon monoxide partial pressure studied requires the use of high reaction temperatures to avoid rapid deactivation of the Ni catalyst (see Appendix A). The sintered catalyst (ca. 0.25 g) was then loaded into the Mössbauer spectroscopy cell, followed by 2.5 h reduction at 723 K in flowing hydrogen ( $P_{H_2} = 308$  kPa).

The Fe(CO)<sub>5</sub> used in deactivation studies was produced in situ by reacting high pressure CO with iron supported on alumina in a "carbonyl reactor." This approach avoided the hazards associated with handling the highly toxic Fe(CO)<sub>5</sub> liquid. The carbonyl reactor was made of a piece of 316 stainless steel tubing, 1.27 cm OD x 1.02 cm ID and 7.62 cm in length, and located between the precision needle valve and back pressure regulator (see Appendix A). The reactor was operated at  $P_{CO} = 4.0$  MPa and  $T = 473$  K for in situ production of Fe(CO)<sub>5</sub>. After passing through this reactor, the Fe(CO)<sub>5</sub> entrained CO was then mixed with H<sub>2</sub> to produce synthesis gas of the desired composition. The Fe(CO)<sub>5</sub> was then carried into the Mössbauer cell by the reactant mixture, and decomposed on the catalyst at 623-633 K. The high pressure thermal conductivity cell for monitoring gas

phase composition changes (see Appendix A) was not used during this application to prevent  $\text{Fe}(\text{CO})_5$  from decomposing prematurely on the heated filaments.

The supported iron catalysts used in the "carbonyl reactor" (9.8 wt. % Fe on  $\alpha\text{-Al}_2\text{O}_3$ ) were prepared by multiple incipient wetness impregnation using 80/200 mesh low surface area  $\alpha\text{-Al}_2\text{O}_3$  and aqueous  $\text{Fe}(\text{NO}_3)_3$  solution. To synthesize a catalyst containing Fe with its natural abundance of  $^{57}\text{Fe}$ ,  $\text{Fe}(\text{NO}_3)_3 \cdot 9\text{H}_2\text{O}$  (Baker analyzed reagent) was used for preparation of the impregnation solution. The impregnation solution for synthesizing an  $^{57}\text{Fe}$ -enriched catalyst was prepared by first reducing  $^{57}\text{Fe}_2\text{O}_3$  powder (Oak Ridge National Lab.) in flowing  $\text{H}_2$  at 723 K for 24 h, then dissolving the reduced mass in 30 wt. %  $\text{HNO}_3$  (at room temperature) without exposure to air. (The use of iron enriched in  $^{57}\text{Fe}$  is essential for collecting in situ Mössbauer spectra at minimal concentrations of Fe.) The iron catalysts were dried at 388 K for, at least, 2 h after each impregnation. Once the desired metal loading was reached, the sample was then (i) dried overnight at 388 K, (ii) reduced in flowing  $\text{H}_2$  at 723 K for 24 h, (iii) cooled in flowing  $\text{H}_2$ , and (iv) flushed with He at room temperature. Passivation of the reduced samples was done by letting air diffuse into the He-filled reduction cell through a valve opened to the air. Approximately 0.5 g of this passivated catalyst was loaded into the "carbonyl reactor" for in situ production of  $\text{Fe}(\text{CO})_5$ .

The decreasing methanation activity of a Ni catalyst was monitored during exposure of the catalyst to a given  $\text{CO}/\text{H}_2$  gas mixture containing  $\text{Fe}(\text{CO})_5$ . The "carbonyl reactor" was then bypassed, and the deactivated catalyst was treated in flowing  $\text{H}_2$

until no  $\text{CH}_4$  could be observed in the effluent gas from the Mössbauer cell (ca. 2.5 h). The methanation kinetics of this partially deactivated catalyst were then studied using the procedures described earlier (see Appendix A). In situ Mössbauer spectra were collected either under methanation reaction conditions or at room temperature after quenching the catalyst in flowing hydrogen. The rationale for computer-fitting these Mössbauer spectra, in the presence of a spectral component from the iron impurities in the beryllium windows of the cell, was described earlier in this report.

## II.B. RESULTS

The methanation activity of a supported Ni catalyst before, during and after the introduction of  $^{57}\text{Fe}(\text{CO})_5$  are shown in Figure 1 as a function of time on-stream for Run 2. Similar results were observed for Run 1, where  $\text{Fe}(\text{CO})_5$  with the natural abundance of  $^{57}\text{Fe}$  was used. Before the introduction of  $\text{Fe}(\text{CO})_5$ , the fresh catalyst showed a 15% decrease in activity during the initial 3 h. Thereafter, the catalytic activity remained relatively constant, showing only a 15% decrease in activity over a period of 24 h. (All percentages will be normalized against the initial catalytic activity measured upon commencement of reaction conditions.) During the first  $\text{Fe}(\text{CO})_5$  treatment, there was an induction period of ca. 2.5 h, during which the activity of the catalyst decreased only slightly. The catalytic activity then dropped sharply by 50% within 8 h. No induction period was observed during the second exposure of the catalyst to  $\text{Fe}(\text{CO})_5$ . In particular, the catalyst showed an initial sharp decrease in activity by 50% within 8 h, followed by constant activity thereafter. The deactivation studies carried

out after completion of each  $\text{Fe}(\text{CO})_5$  dosing followed the same trend as that observed during the second  $\text{Fe}(\text{CO})_5$  treatment, no induction period was present. It should also be noted that ca. 30-50% of the lost catalytic activity for the iron-containing catalyst could be recovered by  $\text{H}_2$  treatment at reaction temperatures (623-633 K). No such activity regeneration was observed for the Fe-free catalyst.

Kinetic studies for the Fe-free catalyst and the catalyst after the first and second  $\text{Fe}(\text{CO})_5$  doses showed systematic changes in kinetic parameters, as shown in Figures 2-5. The kinetic parameters are summarized in Table 1. The published results (1) of methanation over  $\text{Fe}/\text{Al}_2\text{O}_3$  and  $\text{Ni}/\text{Al}_2\text{O}_3$  catalysts are also included in Table 1 for comparison. As easily seen therein, increasing the amount of Fe deposited on the Ni-catalyst (i) decreases the activation energy, (ii) increases the hydrogen partial pressure dependence of the rate, and (iii) does not affect the CO partial pressure dependence. It is also noted that the activity begins to approach a constant value at high hydrogen partial pressures (ca. 413 kPa) (see Figures 4 and 5).

Mössbauer spectra of the iron-containing catalysts after various treatments are shown in Figures 6-14. Stick diagrams are used to indicate the known positions of absorption peaks of specific iron-containing species. During hydrogen treatment, the in situ Mössbauer spectrum indicates the presence of metallic iron in both ferromagnetic and superparamagnetic states (Figure 6). The existence of ferromagnetic iron (6-peak pattern) is evidenced by the two small, outer-most absorption peaks at ca.  $\pm 5.0$  mm/s. The singlet with slightly negative isomer shift is attributed to superparamagnetic metallic iron. Additional information can



be seen in the room temperature spectra following hydrogen treatment (see Figures 7, 10, 13). In addition to ferromagnetic and superparamagnetic metallic iron, as observed in the in situ spectrum, the presence of a small amount of  $\text{Fe}^{2+}$  is manifested by the broad shoulder at +2.0 mm/s. The other absorption peak of the  $\text{Fe}^{2+}$  doublet is masked by the inner two absorption peaks of ferromagnetic metallic iron and the singlet of superparamagnetic metallic iron.

No ferromagnetic metallic iron can be seen in the in situ spectra of the catalyst under methanation reaction conditions (see Figures 8 and 14). The complexities involved in identifying the iron-containing phase(s) of the catalyst under reaction conditions will be discussed later. The room temperature spectra (Figures 9, 11 and 12) of the catalyst after reaction conditions indicate the presence of  $\text{Fe}^{2+}$  species and an iron-carbide phase. The partially collapsed, broad absorption peak is typical of an iron-carbide phase, while the absorption peak at +2.0 mm/s is the higher velocity peak of the  $\text{Fe}^{2+}$  doublet noted above.

### II.C. DISCUSSION

The kinetic parameters (i.e. the activation energy and the partial pressure dependencies of the rate) of the Fe-free Ni methanation catalyst (see Table 1) agree very well with those measured in a high pressure tubular reactor (see Appendix A). Such an agreement confirms that the high pressure Mössbauer spectroscopy cell is indeed capable of providing valid kinetic data, despite its vastly different configuration from the high pressure tubular reactor.

The kinetic parameters follow a systematic trend with increasing iron-content, i.e. the catalytic properties shift

from those of a Ni catalyst to those of an Fe catalyst. This is seen in Table 1 by comparing the kinetic parameters of the Ni catalyst after various  $\text{Fe}(\text{CO})_5$  doses with those parameters reported for Ni/ $\text{Al}_2\text{O}_3$  and Fe/ $\text{Al}_2\text{O}_3$  (1). Thus, the decomposition of  $\text{Fe}(\text{CO})_5$  on a supported Ni catalyst can convert the Ni catalyst to a pseudo-Fe catalyst. Such a conversion could be accomplished either by covering the Ni surface with, at least, a monolayer of Fe, or by forming Fe particles at the pore mouths of the catalyst support. The latter mechanism requires that the Fe particles (and any carbon deposits) formed have sizes comparable to the average diameter of the pores, in order to effectively diminish the accessibility of the Ni particles within the pores to the reactant gas molecules. These two models for the iron-induced deactivation of nickel under methanation reaction conditions will be discussed below.

The solid state properties of supported Fe-Ni alloy catalysts after Fischer-Tropsch synthesis at atmospheric pressures have recently been characterized using Mössbauer spectroscopy (2-5). The results obtained, however, were contradictory. Raupp and Delgass (2,3) found that no bulk carbides were formed on a 5% Fe - 5% Ni/ $\text{SiO}_2$  catalyst at synthesis conditions. Their particle size is sufficiently small that the room temperature spectrum shows a broad superparamagnetic singlet. On the other hand, Unmuth et al. (4,5) reported the formation of  $\epsilon$ - or  $\epsilon'$ -carbide on a 4% Fe - 1% Ni/ $\text{SiO}_2$  catalyst after temperature-programmed reaction in a  $3\text{H}_2$ :CO reaction mixture. However, their particle size (8.9-12.8 nm) is larger than that of Raupp and Delgass. Thus, the different catalyst states at similar reaction conditions may be attributed to the different Fe/Ni

ratios and/or the different particle sizes used by these two research groups.

The formation of carbides on supported and unsupported iron catalysts under Fischer-Tropsch synthesis conditions has been extensively studied (2-12). The formation of a specific carbide phase depends on particle size, support, and synthesis conditions.  $\epsilon'$ -carbide ( $\text{Fe}_{2.2}\text{C}$ ) has been observed on silica supported catalysts (3,5,6).  $\epsilon$ -Carbide ( $\text{Fe}_2\text{C}$ ) has been detected on silica supported catalysts (3,5), on promoted, fused iron catalysts (8,9,11), and on unpromoted, unsupported iron catalysts (7,12). The formation of  $\chi$ -carbide ( $\text{Fe}_5\text{C}_2$ ) has been evidenced on promoted, fused iron catalysts (9,10) and on various supported catalysts (3). While Mössbauer spectroscopy is a powerful tool in identifying iron carbide phase(s) that show magnetic hyperfine splitting (i.e. for iron carbide particles greater than ca. 10 nm in size), the Mössbauer parameters for superparamagnetic  $\epsilon'$ - and  $\epsilon$ -carbides (i.e. for particles smaller than ca. 10 nm in size) are similar to each other (see Table 2). Thus, the unambiguous identification of iron carbide phase(s) in the superparamagnetic state is difficult.

The phase diagram for Fe-Ni alloys (13) shows the existence of a bcc, iron-rich phase ( $\alpha$ -phase) and of a fcc, nickel-rich phase ( $\gamma$ -phase). The hyperfine magnetic fields of Fe-Ni alloys with various compositions have been measured at room temperature (14), and these are reproduced in Figure 15. In short, the composition of an Fe-Ni alloy formed on a Ni catalyst after  $\text{Fe}(\text{CO})_5$  treatment can be determined by comparing the measured hyperfine magnetic field to Figure 15. The room temperature spectra (Figures 7, 10, 13) show a broad sextuplet of ferromagnetic metallic iron with a

hyperfine magnetic field of 329-334 kOe. This is essentially identical to the 330 kOe magnetic field of bulk metallic iron. The spectrum in hydrogen at 623 K (Figure 6) shows this metallic iron to be predominantly in the superparamagnetic state. The temperature at which a ferromagnetic phase behaves superparamagnetically (i.e. the blocking temperature) is a function of the particle size and the magnetic anisotropic barrier energy,  $K$  (15,16). Thus, the particle size can be estimated, provided that the value of  $K$  and the blocking temperature are known. Accordingly, the size of the metallic iron particles is estimated to be 7.0 nm, assuming values for  $K$  and the blocking temperature of  $4.5 \times 10^5 \text{ erg/cm}^3$  and 623 K respectively. In short, it can be concluded that the decomposition of  $\text{Fe}(\text{CO})_5$  on an alumina-supported Ni catalyst does not lead to the formation of an Fe-Ni alloy, but instead, metallic iron particles with an average diameter of 7.0 nm are produced.

The Mössbauer spectra collected under reaction conditions (Figures 8 and 14) show an asymmetric doublet. The scarcity of published Mössbauer spectra for iron carbides at elevated temperatures and the similarity of Mössbauer spectra for superparamagnetic iron carbides (Table 2) make the in situ identification of the carbide phase impossible. The room temperature spectra following quenching from reaction conditions (Figures 9, 11, 12) show a partially collapsed spectrum due to small iron carbide particles. However, due to complications from superparamagnetism, it is not possible to unambiguously identify the carbide phase by determining its Curie temperature, as done in references 3 and 11. Despite the pending identification of the carbide phase, there is no doubt that the iron deposited via decomposition of  $\text{Fe}(\text{CO})_5$  forms a carbide under methanation conditions. This

suggests that either the Fe and Ni are not alloyed with each other (2,3) or an Fe-rich alloy is formed (4,5). This important question will be addressed below.

Assuming that the recoil-free fractions of iron-containing phases in the catalyst bed are equal to that of iron impurity in the Be windows, the amount of Fe deposited on the catalyst due to decomposition of  $\text{Fe}(\text{CO})_5$  can be estimated for Run 2 (where iron enriched in  $^{57}\text{Fe}$  was used. The total amount of iron deposited equals 0.51 mg after 11 h of  $\text{Fe}(\text{CO})_5$  dosing (estimated from Figure 7) and 0.55 mg after 24 h of  $\text{Fe}(\text{CO})_5$  dosing (estimated from Figure 13). This corresponds to a final Fe/Ni ratio of 3.3%. The results of chemical analyses for the used catalyst of Run 1 (where iron containing the natural abundance of  $^{57}\text{Fe}$  was used) indicate that 0.14 mg of Fe had been deposited on the  $\text{Ni}/\text{Al}_2\text{O}_3$  catalyst after 66 h of  $\text{Fe}(\text{CO})_5$  dosing. This corresponds to an Fe/Ni ratio of 0.84%. In view of the very small Fe/Ni ratios for both Runs, it is not possible to cover the Ni surface with a monolayer of Fe unless the average Ni particle size is as large as 20.0-80.0 nm. X-ray diffraction studies on the sintered Ni catalyst showed no evidence for the existence of such large particles. Thus the changes, induced by  $\text{Fe}(\text{CO})_5$  decomposition, in the kinetic properties of the Ni catalyst cannot be attributed to a covering of the Ni surface by an Fe deposit. In summary, a direct interaction between Fe and Ni, either with the formation of an Fe-Ni alloy or an iron monolayer over Ni, is not responsible for the changes in methanation kinetics when  $\text{Ni}/\text{Al}_2\text{O}_3$  is dosed with  $\text{Fe}(\text{CO})_5$ .

Having dismissed a direct interaction between Fe and Ni, the pore-mouth blocking model mentioned previously seems to be necessary in order to explain the results of this study. This model requires the formation of Fe particles (and associated carbon deposits) of size comparable to the average diameter of the  $\text{Al}_2\text{O}_3$  pores at the pore entrance. The  $\gamma\text{-Al}_2\text{O}_3$  support (Davison SMR-7) has a specific surface area of  $260 \text{ m}^2/\text{g}$  and pore volume of  $0.8 \text{ cm}^3/\text{g}$  (determined using  $\text{N}_2$ ) or  $1.1 \text{ cm}^3/\text{g}$  (determined using  $\text{H}_2\text{O}$ ) (17). The calculated average pore diameter, based on the above mentioned physical properties, is 12.3 nm or 17.0 nm. The size of the metallic iron particles was estimated above to be 7.0 nm. Thus the size of the Fe particle formed via  $\text{Fe}(\text{CO})_5$  decomposition is indeed comparable to the average pore diameter.

Carlton and Oxley (18) studied the kinetics of heterogeneous decomposition of  $\text{Fe}(\text{CO})_5$  on a heated filament (diameter = 0.32 cm). They found that the rate of decomposition is controlled by the diffusion of  $\text{Fe}(\text{CO})_5$  from the bulk gas phase to the gas-solid interface at temperatures higher than 473 K. At 623-633 K, the decomposition temperatures employed in this study, it may be anticipated that the rate of  $\text{Fe}(\text{CO})_5$  decomposition is severely limited by diffusion within the pores of the support. Indeed, it is shown in Appendix A that the decomposition of  $\text{Ni}(\text{CO})_4$  is diffusion-controlled in the same  $\gamma\text{-Al}_2\text{O}_3$  support and at similar temperatures. This is why most of the  $\text{Fe}(\text{CO})_5$  would decompose at the pore-mouths, forming Fe particles of comparable size to the average diameter of the pores. Studies of  $\text{Fe}(\text{CO})_5$  decomposition also suggest that pore-mouth blocking is the mode by which iron modifies the catalytic properties of supported Ni.

As shown in Appendix B,  $\text{Fe}(\text{CO})_5$  decomposition on carbon leads to the formation of highly dispersed metallic iron. Furthermore, the metallic iron particles formed in this manner serve as nucleation centers for the further decomposition of  $\text{Fe}(\text{CO})_5$ . This is another mechanism by which the iron is preferentially deposited near the pore-mouths of the catalyst. Moreover, the results of Appendix C show that the rate of  $\text{Fe}(\text{CO})_5$  decomposition is increased as the surface of carbon is outgassed at higher temperatures, or as the number of defect sites on the carbon surface is increased. Indeed, the carbon deposited on the catalyst under methanation reaction conditions is expected to have a high defect concentration (compared to graphite), and the reaction temperatures used in methanation serve to outgas this carbon deposit. This is the third mechanism by which the rate of  $\text{Fe}(\text{CO})_5$  decomposition is enhanced, leading to pore-mouth blocking of the supported Ni catalyst.

Direct evidence for the preferential decomposition of iron near the pore mouths is found in the Mössbauer spectra. It has been shown in the literature (19,20) that iron on alumina at loadings less than ca. 1 wt. % cannot be reduced to the metallic state. Instead,  $\text{Fe}^{2+}$  is stabilized by interaction with the support. Furthermore, we have very recently been studying the decomposition of  $\text{Fe}(\text{CO})_5$  on  $\text{Al}_2\text{O}_3$  and  $\text{TiO}_2$ . Here it is also found that at low iron loadings (less than ca. 1 wt. %),  $\text{Fe}^{2+}$  is formed upon decomposition of  $\text{Fe}(\text{CO})_5$ , and metallic iron is only formed at higher iron loadings. As noted earlier, however, the contribution of  $\text{Fe}^{2+}$  is of minor importance in the Mössbauer spectra of the iron-containing Ni catalyst. Since the average Fe loading in the catalyst is ca. 0.1 wt. %, the absence of a

significant spectral signal from  $Fe^{2+}$  indicates that the local concentration of iron must be at least ten times higher than the average concentration. Clearly, this high local concentration of iron must be present near the external surface of the alumina support, i.e. in the pore mouths.

Additional kinetic evidence for the validity of the pore-mouth model for iron-induced deactivation of nickel methanation catalysts can be found in the response of a deactivated catalyst to hydrogen treatment: 30-50% of the lost methanation activity can be restored by such a treatment. It has been reported in the literature that carbon is deposited on Fe much faster than on Ni in the same  $H_2/CO$  gas mixture (5). Thus, the carbon deposited on the iron-containing catalyst would be present preferentially near the pore mouths. In this way, the removal of this carbon during hydrogen treatment should significantly increase the activity of a deactivated catalyst, as observed experimentally.

#### II.D. CONCLUSIONS

The iron deposited on a supported Ni catalyst during exposure to  $Fe(CO)_5$  under methanation reaction conditions does not interact directly with nickel. That is, an Fe-Ni alloy is not formed and the iron does not form a monolayer coating over the nickel crystallites. Instead, the  $Fe(CO)_5$  induced deactivation of supported Ni methanation catalyst proceeds via the decomposition of  $Fe(CO)_5$  at the pore mouths of the support, diminishing the accessibility of the Ni surface to reactant species. This problem is exacerbated by the increased propensity of iron to form carbon deposits compared to nickel. These carbon deposits deactivate



the iron catalyst for methanation, and they further block the pore mouths. In addition, the presence of such carbon deposits (with high defect concentrations) and iron particles in the pore mouths creates nucleation centers for the further decomposition of  $\text{Fe}(\text{CO})_5$ , leading to continued deposition of iron near the external surface of the support.

## II.E. REFERENCES

- (1) Vannice, M. A., *J. Catal.* 37, 449 (1975).
- (2) Raupp, G. B., and Delgass, W. N., *J. Catal.* 58, 337 (1979).
- (3) Raupp, G. B., and Delgass, W. N., *J. Catal.* 58, 348 (1979).
- (4) Unmuth, E. E., Schwartz, L. H., and Butt, J. B., *J. Catal.* 61, 242 (1980).
- (5) Unmuth, E. E., Schwartz, L. H., and Butt, J. B., *J. Catal.* 63, 404 (1980).
- (6) Amelse, J. A., Butt, J. B., and Schwartz, L. H., *J. Phys. Chem.* 82, 558 (1978).
- (7) Le Caer, G., Simon, A., Lorenzo, A., and Génin, J. M., *Phys. Stat. Sol. (a)* 6, K97 (1971).
- (8) Maksimov, Yu. V., Suzdalev, I. P., Arents, R. A., and Loktev, S. M., *Kinet. Katal.* 15, 1293 (1974).
- (9) Hofer, L. J. E., Cohn, E. M., and Peebles, W. C., *J. Am. Chem. Soc.* 71, 189 (1949).
- (10) Maksimov, Yu. V., Suzdalev, I. P., Arents, R. A., Goncharov, I. V., Krautsov, A. V., and Loktev, S. M., *Kinet. Katal.* 13, 1600 (1972).
- (11) Loktev, S. M., Makarenkova, L. I., Slivinskii, E. V., and Entin, S. D., *Kinet. Katal.* 13, 1042 (1972).
- (12) Niemantsverdriet, J. W., van der Kraan, A. M., van Dijk, W. L., and van der Baan, J. *Phys. Chem.* 84, 3363 (1980).
- (13) Hansen, M., "Constitution of Binary Alloys", McGraw-Hill, New York (1958).
- (14) Johnson, C. E., Ridout, M. S., and Cranshaw, T. E., *Proc. Phys. Soc. (London)* 81, 1079 (1963).
- (15) Mørup, S., Topsøe, H., and Lipka, J., *J. Physique* 37, C-287 (1976).
- (16) Mørup, S., Topsøe, H., *Appl. Phys.* 11, 63 (1976).
- (17) Physical properties provided by manufacturer.
- (18) Carlton, H. E., and Oxley, J. H., *A.I.Ch.E. J.* 11, 79 (1965).
- (19) Dumesic, J. A., and Topsøe, H., *Adv. Catal.* 26, 121 (1971).
- (20) Topsøe, H., Dumesic, J. A., and Mørup, S., in "Application of Mössbauer Spectroscopy" (R. L. Cohen, ed.), Vol. 2, p. 55, Academic Press (1980).

Table 1: Summary of Kinetic Parameters<sup>(a)</sup> for Ni/Al<sub>2</sub>O<sub>3</sub> Before and After Fe(CO)<sub>5</sub> Dosing

	E <sub>A</sub> (kcal/mole)	x	y
Run 1			
Fresh Ni/Al <sub>2</sub> O <sub>3</sub> Catalyst	28.0	0.65	0.04
Catalyst after 22.5 h Fe(CO) <sub>5</sub> dosing (natural iron)	26.8	0.66	0.03
Catalyst after 66 h Fe(CO) <sub>5</sub> dosing (natural iron)	18.7	1.05	0.09
Run 2			
Fresh Ni/Al <sub>2</sub> O <sub>3</sub> Catalyst	28.2	0.65	0.11
Catalyst after 11 h <sup>57</sup> Fe(CO) <sub>5</sub> dosing	20.7	0.96	0.06
Catalyst after 24 h <sup>57</sup> Fe(CO) <sub>5</sub> dosing	18.6	1.04	0.06
5% Ni/Al <sub>2</sub> O <sub>3</sub> <sup>(b)</sup>	25.0	0.77	-0.31
15% Fe/Al <sub>2</sub> O <sub>3</sub> <sup>(b)</sup>	21.3	1.14	-0.05

$$(a) \quad r_{\text{CH}_4} = A e^{-\frac{E_A}{RT}} P_{\text{H}_2}^x P_{\text{CO}}^y$$

(b) Results of kinetic studies from reference (1).

Table 2: Mössbauer Parameters of Various Iron Phases

Phase	IS(mm/s)	QS(mm/s)	line position (mm/s)		Ref.
superparamagnetic $\epsilon^{\text{I}}\text{-Fe}_{2.2}\text{C}$	0.25	0.96	-0.23	0.73	(6)
superparamagnetic $\epsilon^{\text{I}}$ -carbide	0.25	0.9	-0.20	0.70	(8)
superparamagnetic $\epsilon\text{-Fe}_2\text{C}$ (a)	0.36	0.76	-0.40	0.74	(7)
$\text{Fe}^{2+}$ (b)	1.06	1.97	0.075	2.05	(2)
Fe impurities in Be windows (c)	0.124	0.588	-0.17	0.42	

(a) Particle size determined by electron microscopy is smaller than 10 nm.

(b) Particle size is smaller than 4.0 nm.

(c) Computer-fitted parameters of a blank run.

## Figure Captions

- Figure 1 Deactivation studies of Ni/Al<sub>2</sub>O<sub>3</sub> (Run 2) for P<sub>H<sub>2</sub></sub> = 130 kPa and, P<sub>CO</sub> = 18.6 kPa.
- : Fresh Ni/Al<sub>2</sub>O<sub>3</sub> catalyst at 613 K
  - : Ni/Al<sub>2</sub>O<sub>3</sub> catalyst at 613 K after the first deactivation study and kinetic studies
  - △: Ni/Al<sub>2</sub>O<sub>3</sub> catalyst at 623 K during the first <sup>57</sup>Fe(CO)<sub>5</sub> dosing
  - ▲: Ni/Al<sub>2</sub>O<sub>3</sub> catalyst at 623 K after 11 h <sup>57</sup>Fe(CO)<sub>5</sub> dosing
  - : Ni/Al<sub>2</sub>O<sub>3</sub> catalyst at 633 K during the second <sup>57</sup>Fe(CO)<sub>5</sub> dosing
  - : Ni/Al<sub>2</sub>O<sub>3</sub> catalyst at 633 K after 24 h (cumulative) <sup>57</sup>Fe(CO)<sub>5</sub> dosing
- The last point in each series of deactivation studies was collected after H<sub>2</sub> treatment at the respective deactivation temperature for at least 2 h.
- Figure 2 Arrhenius plots of Run 1 for P<sub>H<sub>2</sub></sub> = 282 kPa and P<sub>CO</sub> = 23.4 kPa.
- : Fresh Ni/Al<sub>2</sub>O<sub>3</sub> catalyst; E<sub>A</sub> = 28.0 kcal/mole
  - : Ni/Al<sub>2</sub>O<sub>3</sub> catalyst after 22.5 h Fe(CO)<sub>5</sub> dosing (natural iron); E<sub>A</sub> = 26.8 kcal/mole
  - △: Ni/Al<sub>2</sub>O<sub>3</sub> catalyst after 66 h Fe(CO)<sub>5</sub> dosing (natural iron); E<sub>A</sub> = 18.7 kcal/mole
- Figure 3 Arrhenius plots of Run 2 for P<sub>H<sub>2</sub></sub> = 281 kPa and P<sub>CO</sub> = 23.4 kPa.
- : Fresh Ni/Al<sub>2</sub>O<sub>3</sub> catalyst; E<sub>A</sub> = 28.2 kcal/mole
  - △: Ni/Al<sub>2</sub>O<sub>3</sub> catalyst after 11 h <sup>57</sup>Fe(CO)<sub>5</sub> dosing; E<sub>A</sub> = 20.7 kcal/mole
  - : Ni/Al<sub>2</sub>O<sub>3</sub> catalyst after 24 h <sup>57</sup>Fe(CO)<sub>5</sub> dosing; E<sub>A</sub> = 18.6 kcal/mole
- Figure 4 Partial pressure dependence of methanation rate from Run 1 ( $r_{CH_4} = kP_{H_2}^x P_{CO}^y$ ).
- : Fresh Ni/Al<sub>2</sub>O<sub>3</sub> catalyst at 623 K; x = 0.065, y = 0.04
  - : Ni/Al<sub>2</sub>O<sub>3</sub> catalyst at 633 K after 22.5 h Fe(CO)<sub>5</sub> dosing (natural iron); x = 0.66, y = 0.03
  - △: Ni/Al<sub>2</sub>O<sub>3</sub> catalyst at 643 K after 66 h Fe(CO)<sub>5</sub> dosing (natural iron); x = 1.05, y = 0.09
- Figure 5 Partial pressure dependence of methanation rate from Run 2 ( $r_{CH_4} = kP_{H_2}^x P_{CO}^y$ ).
- : Fresh Ni/Al<sub>2</sub>O<sub>3</sub> catalyst at 613 K; x = 0.65, y = 0.11
  - △: Ni/Al<sub>2</sub>O<sub>3</sub> catalyst at 623 K after 11 h <sup>57</sup>Fe(CO)<sub>5</sub> dosing; x = 0.96, y = 0.06
  - : Ni/Al<sub>2</sub>O<sub>3</sub> catalyst at 633 K after 24 h <sup>57</sup>Fe(CO)<sub>5</sub> dosing; x = 1.04, y = 0.06

- Figure 6 Mössbauer spectrum at 623 K in hydrogen after 11 h  $^{57}\text{Fe}(\text{CO})_5$  dosing and 2 h hydrogen flushing.
- Figure 7 Room temperature Mössbauer spectrum in hydrogen after quenching the sample following collection of Figure 6.
- Figure 8 In situ Mössbauer spectrum collected during the deactivation studies at 623 K after the first  $^{57}\text{Fe}(\text{CO})_5$  dose.
- Figure 9 Room temperature Mössbauer spectrum in hydrogen after quenching the sample in hydrogen following collection of Figure 8. The partially collapsed carbide has been computer-fitted with a broad singlet.
- Figure 10 Room temperature Mössbauer spectrum in hydrogen after heating the sample in hydrogen at 623 K for 40 min (until no  $\text{CH}_4$  was detected in the effluent from the cell) following collection of Figure 9.
- Figure 11 Room temperature Mössbauer spectrum in hydrogen after exposure of the sample to methanation reaction conditions for 0.5 h ( $P_{\text{H}_2} = 284$  kPa,  $P_{\text{CO}} = 35.8$  kPa,  $T = 623$  K) and quenching in hydrogen, following collection of Figure 10. The partially collapsed carbide has been computer-fitted with a broad singlet.
- Figure 12 Room temperature Mössbauer spectrum in hydrogen after second  $^{57}\text{Fe}(\text{CO})_5$  dose and quenching in hydrogen, following collection of Figure 11. The partially collapsed carbide has been computer-fitted with a broad singlet.
- Figure 13 Room temperature Mössbauer spectrum in hydrogen after heating the sample in hydrogen at 633 K for 30 min (until no  $\text{CH}_4$  can be measured in the effluent from the cell) following collection of Figure 12.
- Figure 14 In situ Mössbauer spectrum collected during the deactivation studies at 633 K after the second  $^{57}\text{Fe}(\text{CO})_5$  dose.
- Figure 15 Room temperature hyperfine magnetic fields for bulk Fe-Ni alloys (14).

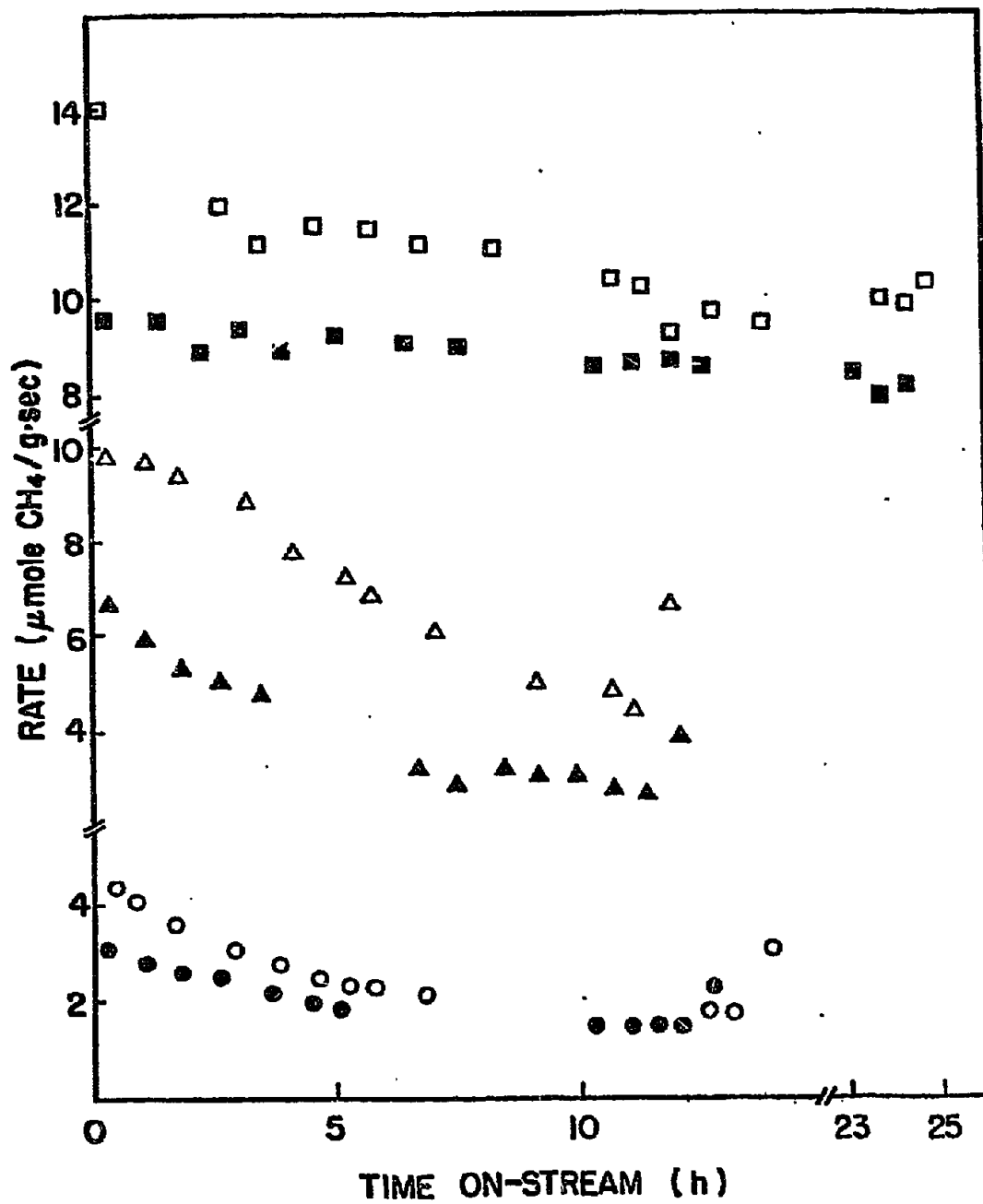


Figure 1

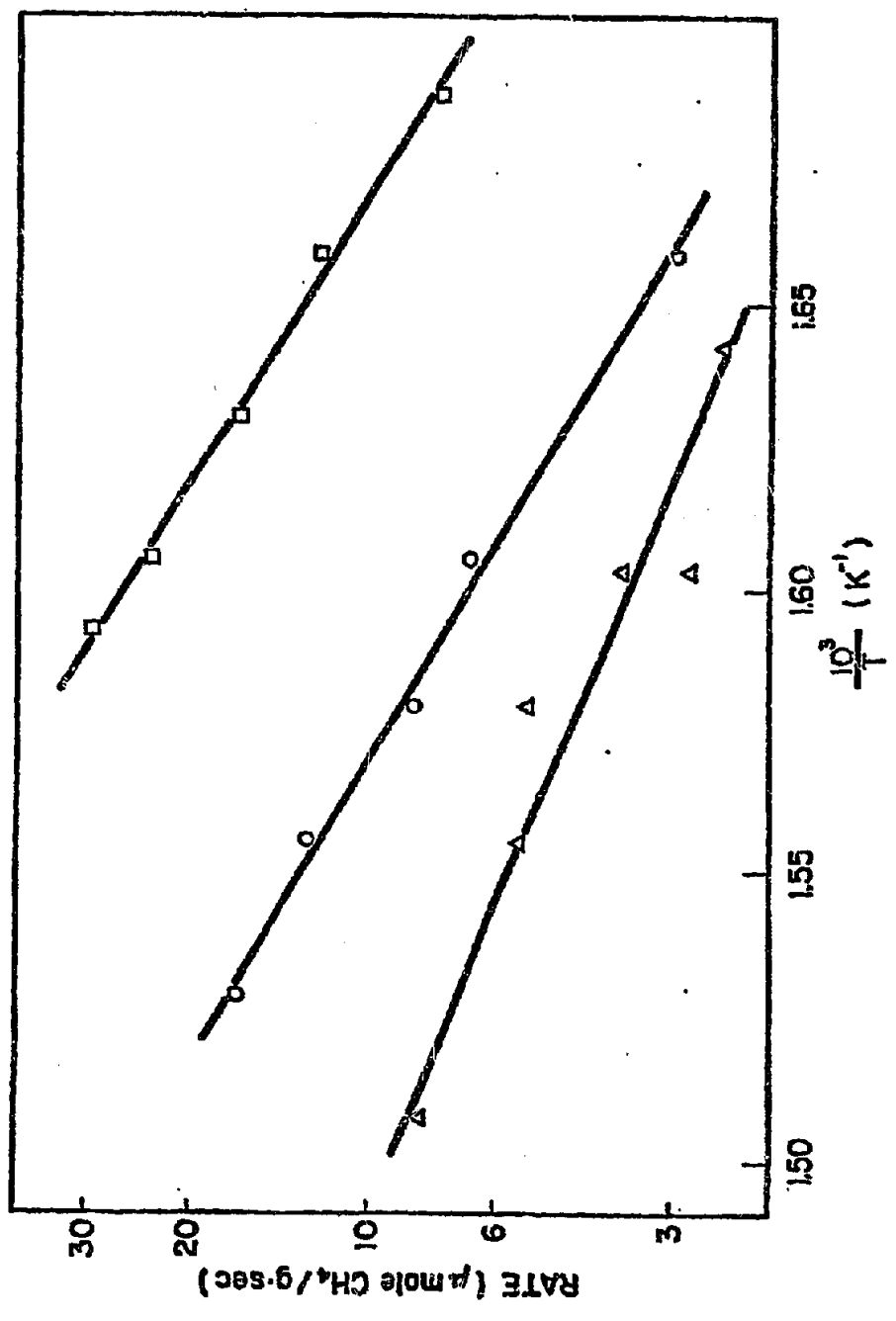


Figure 2



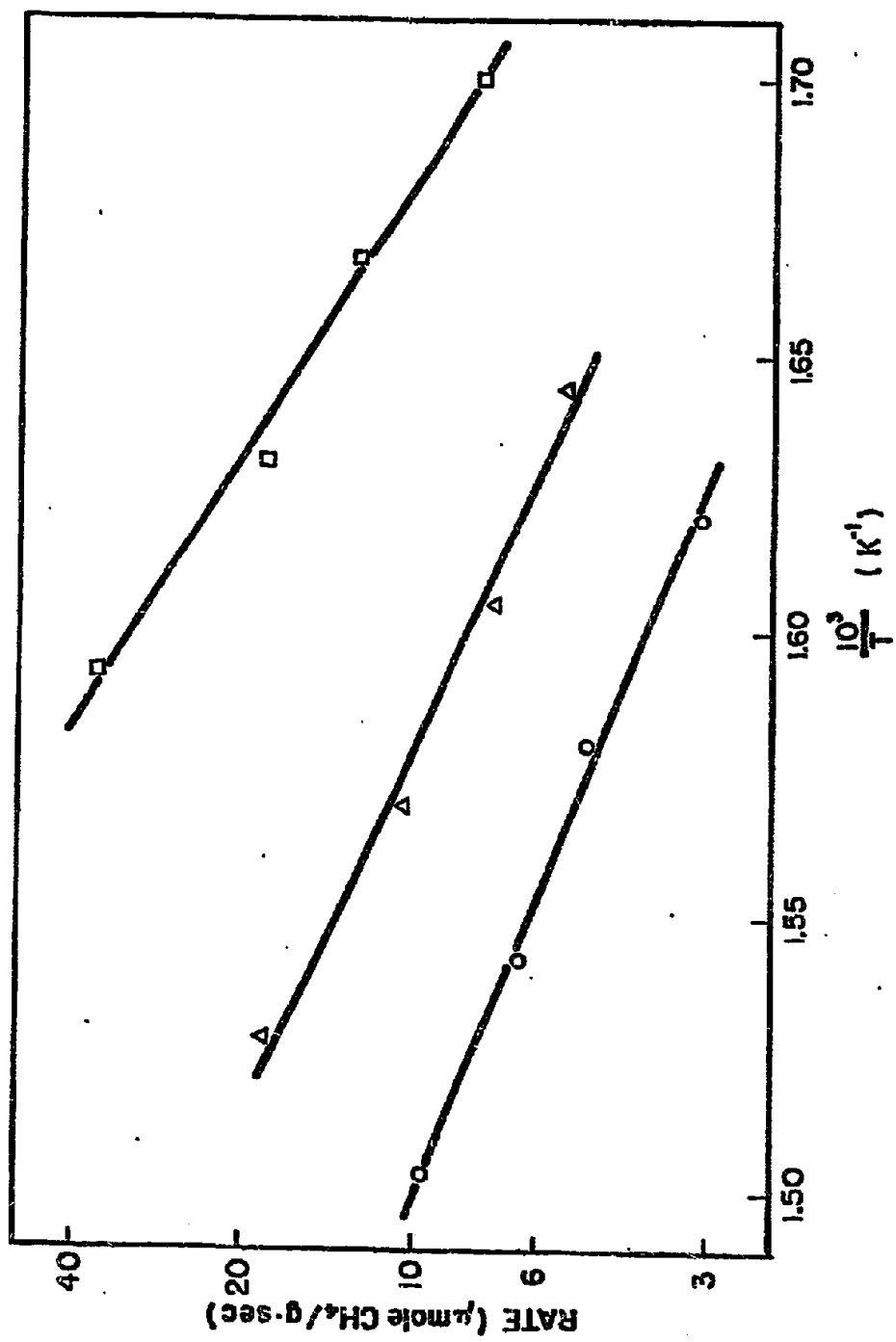


Figure 3

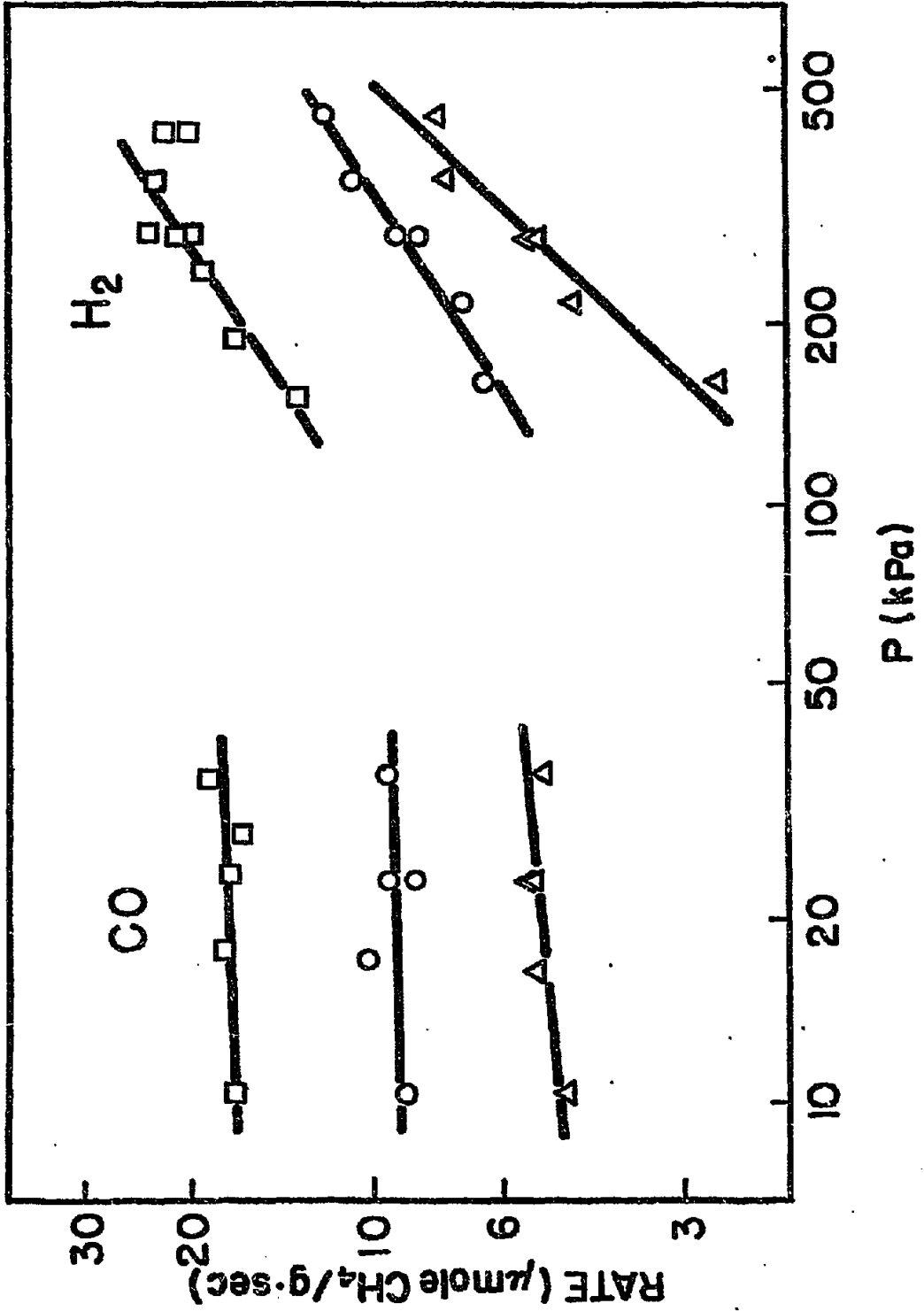


Figure 4

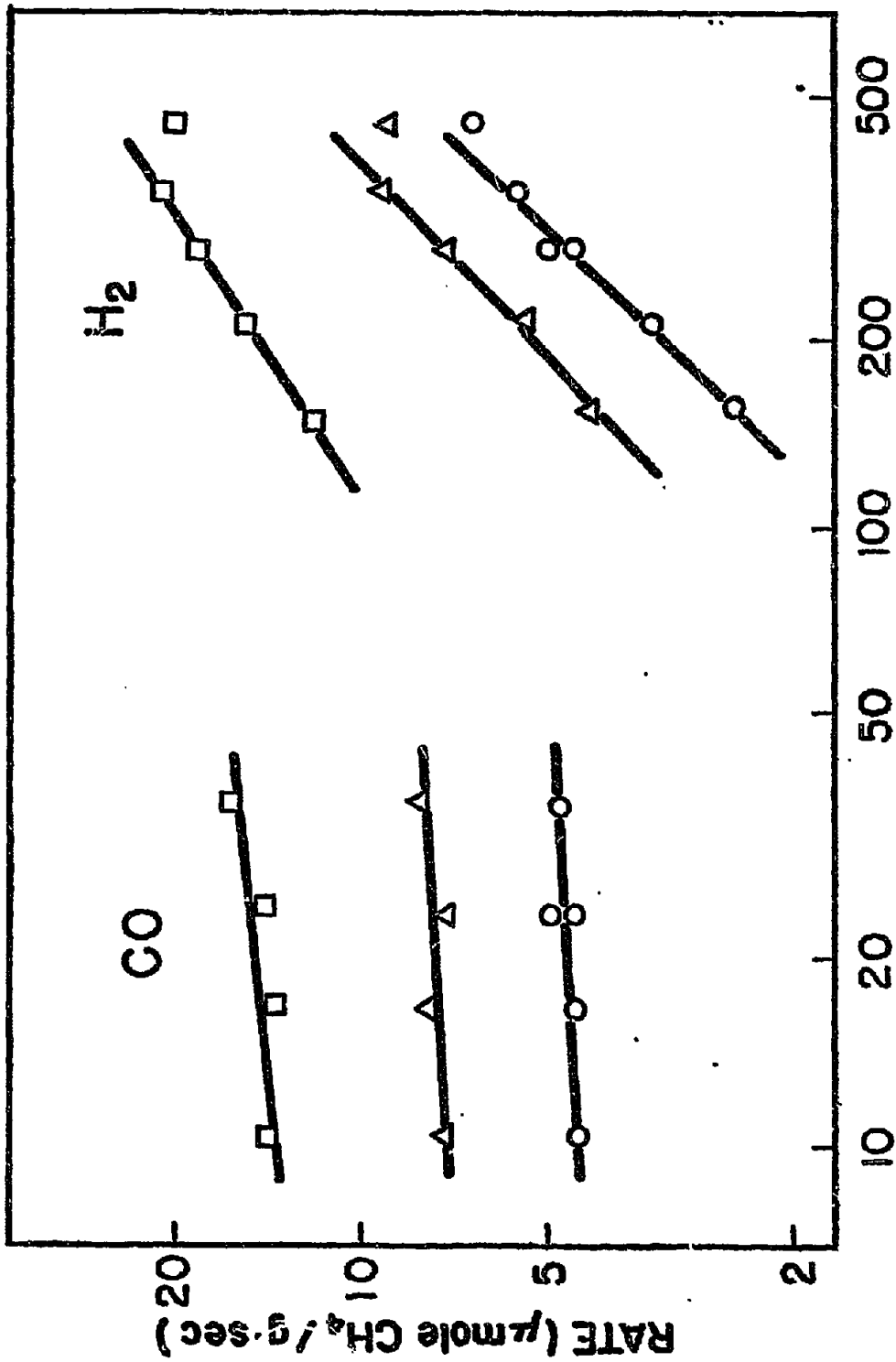


Figure 5

U=\*\*W

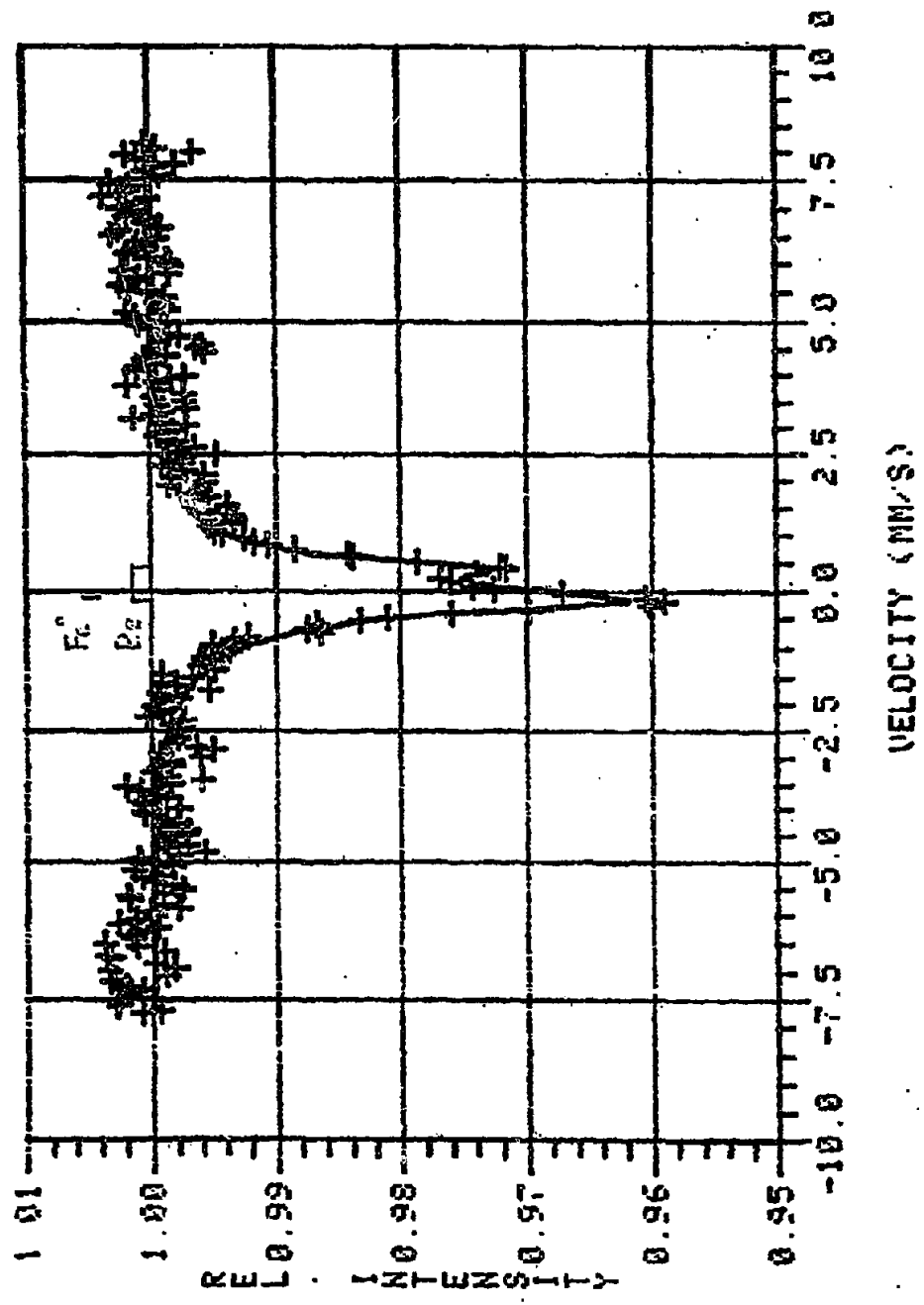


Figure. 6

U--W

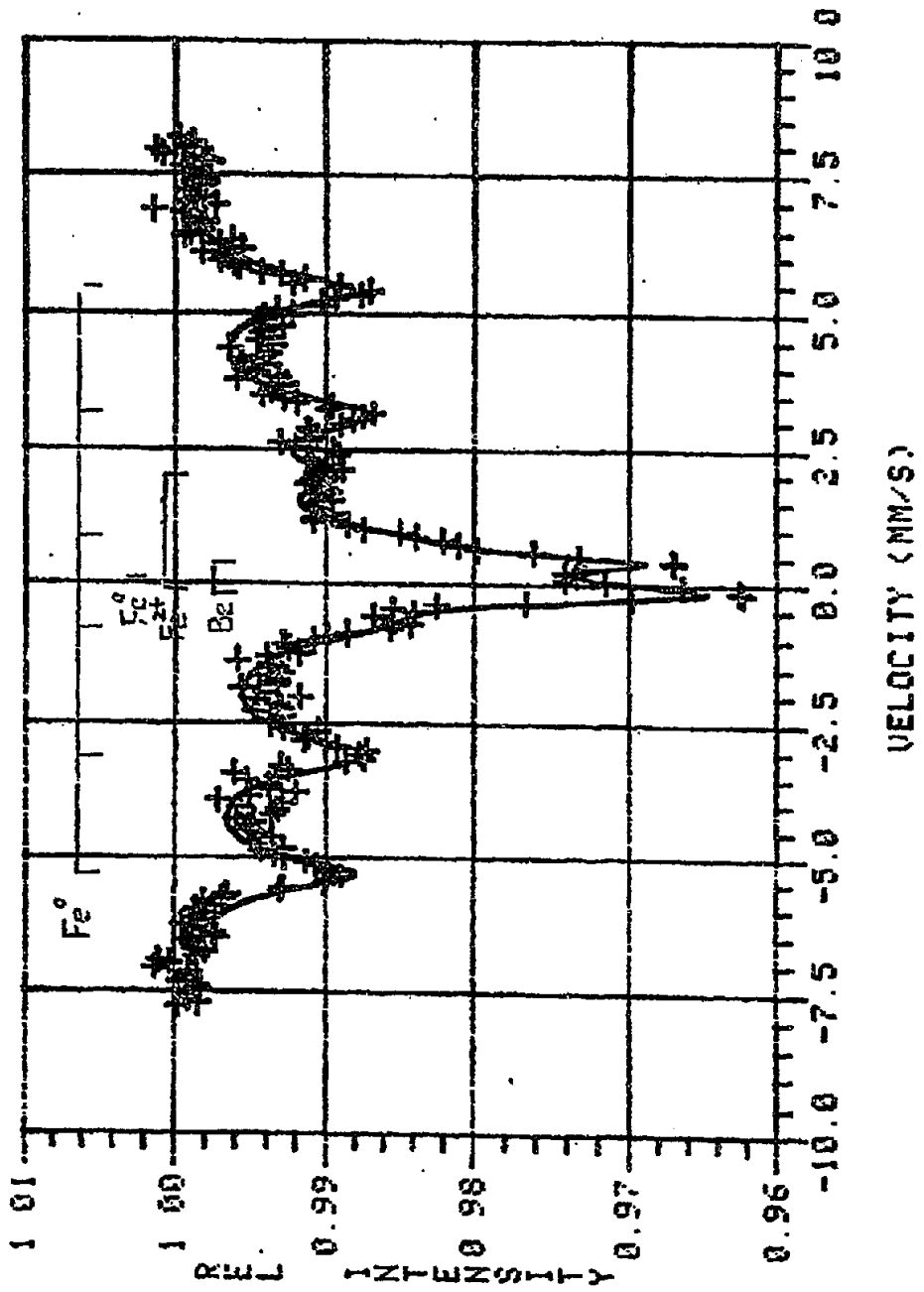


Figure 7

U-W

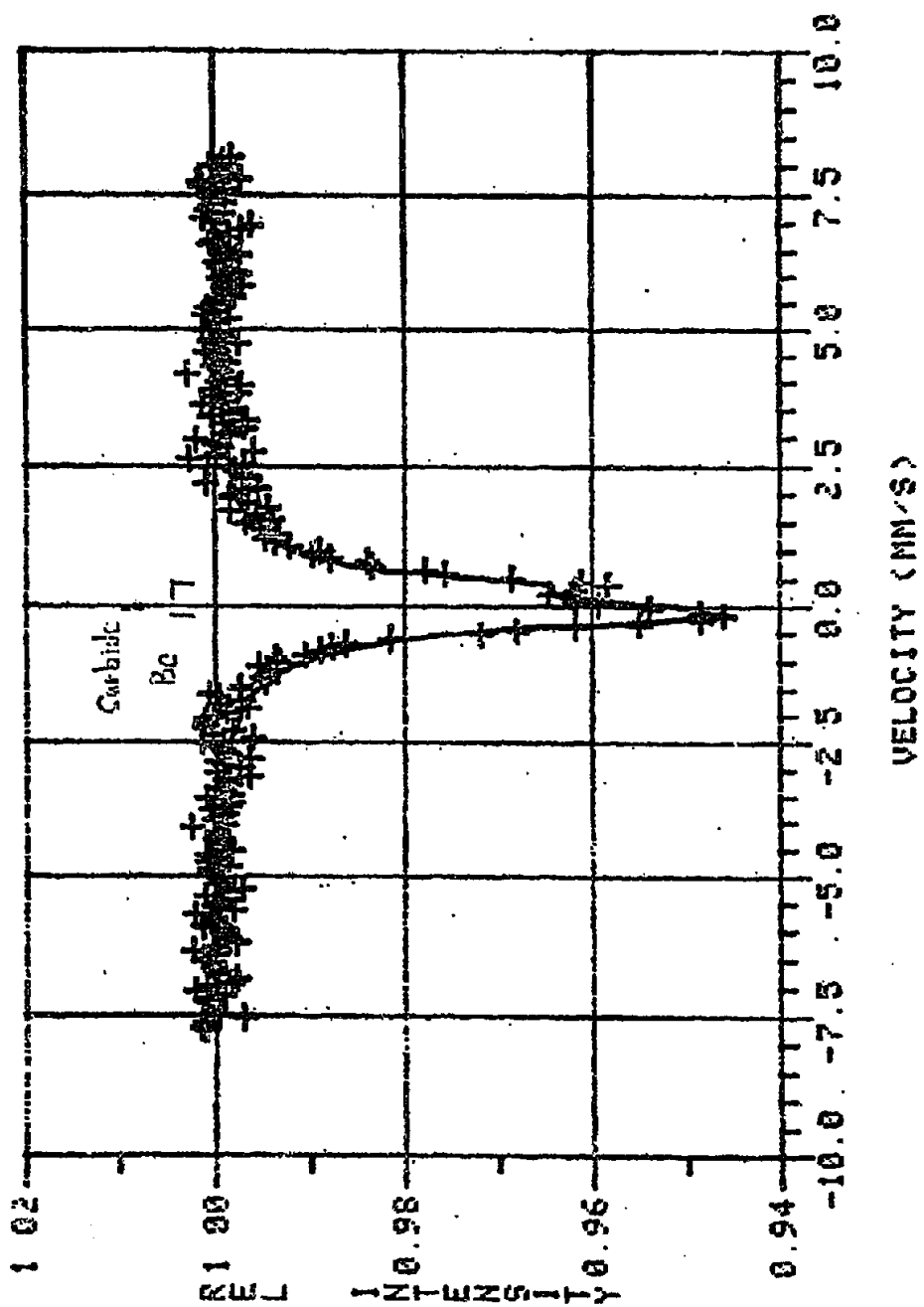


Figure 8

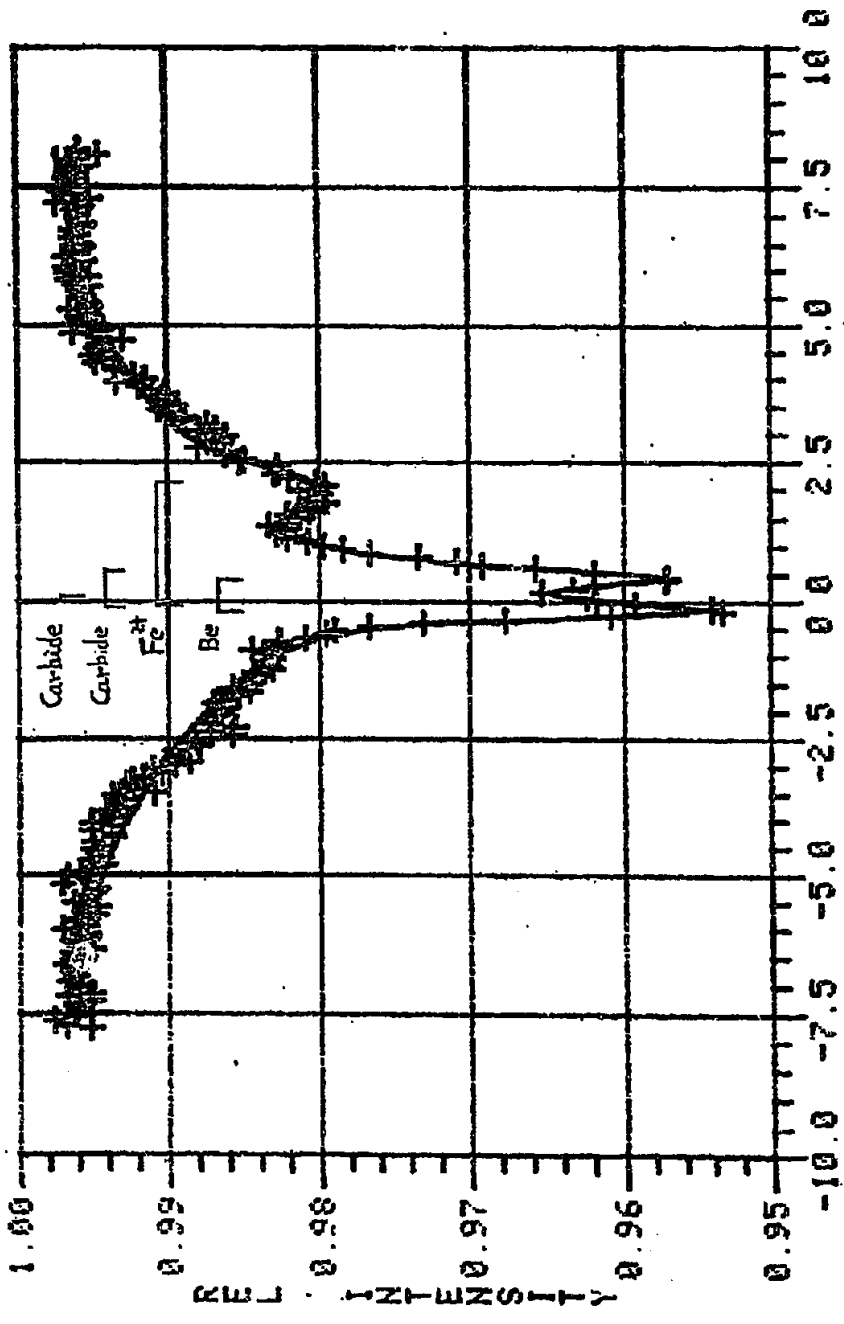


Figure 9

U<sup>235</sup>W

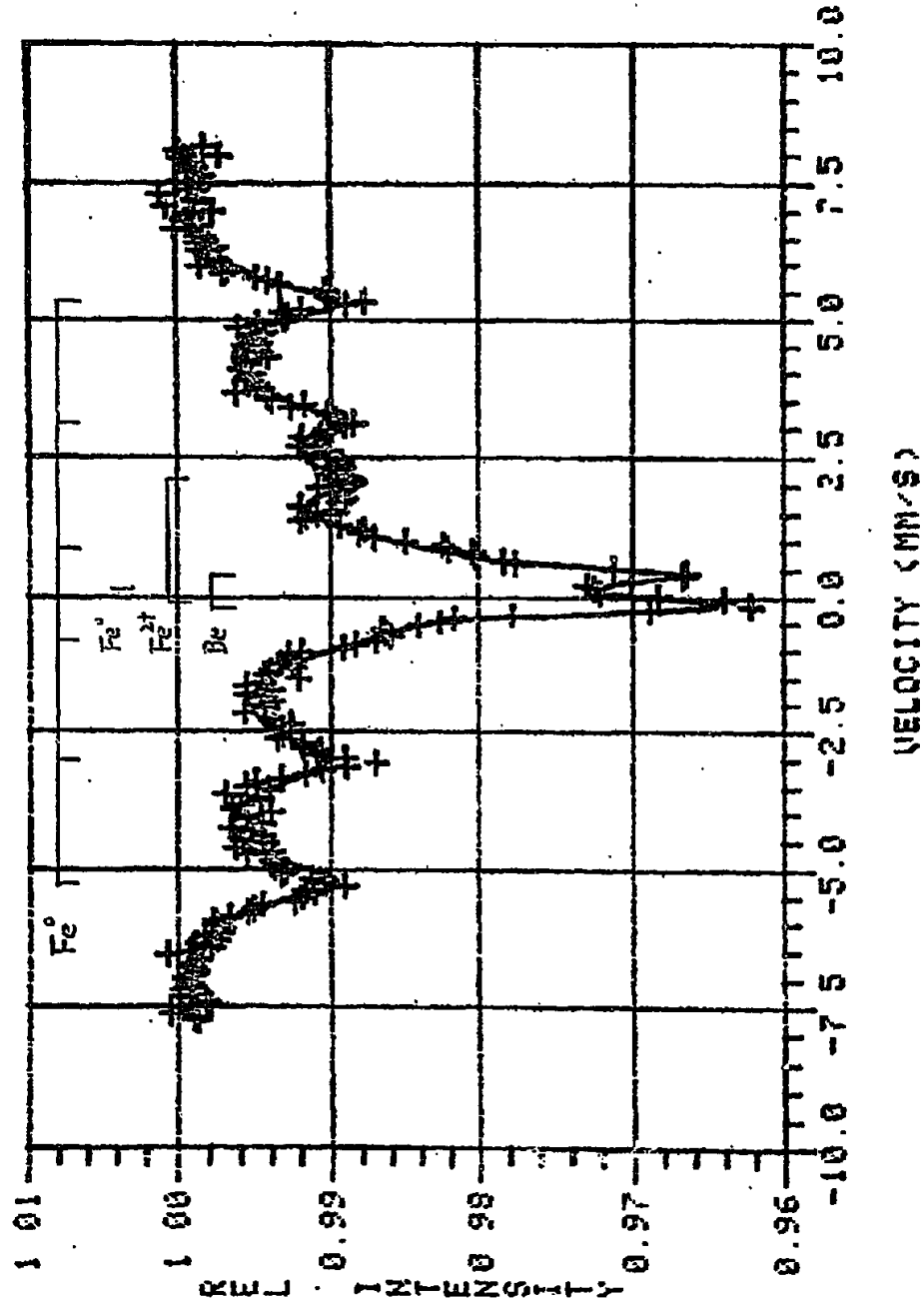


Figure 10



M-W  
U-N

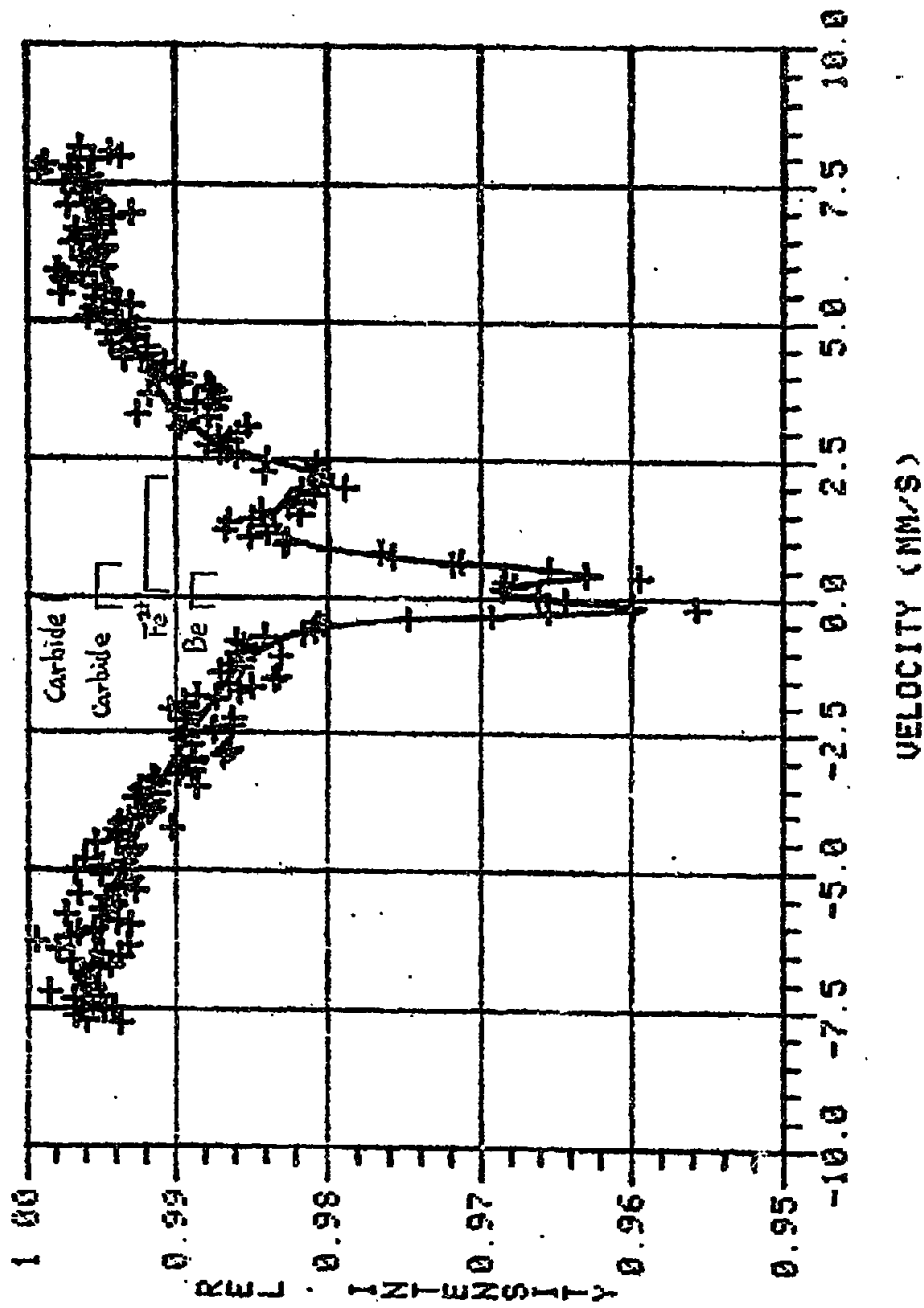
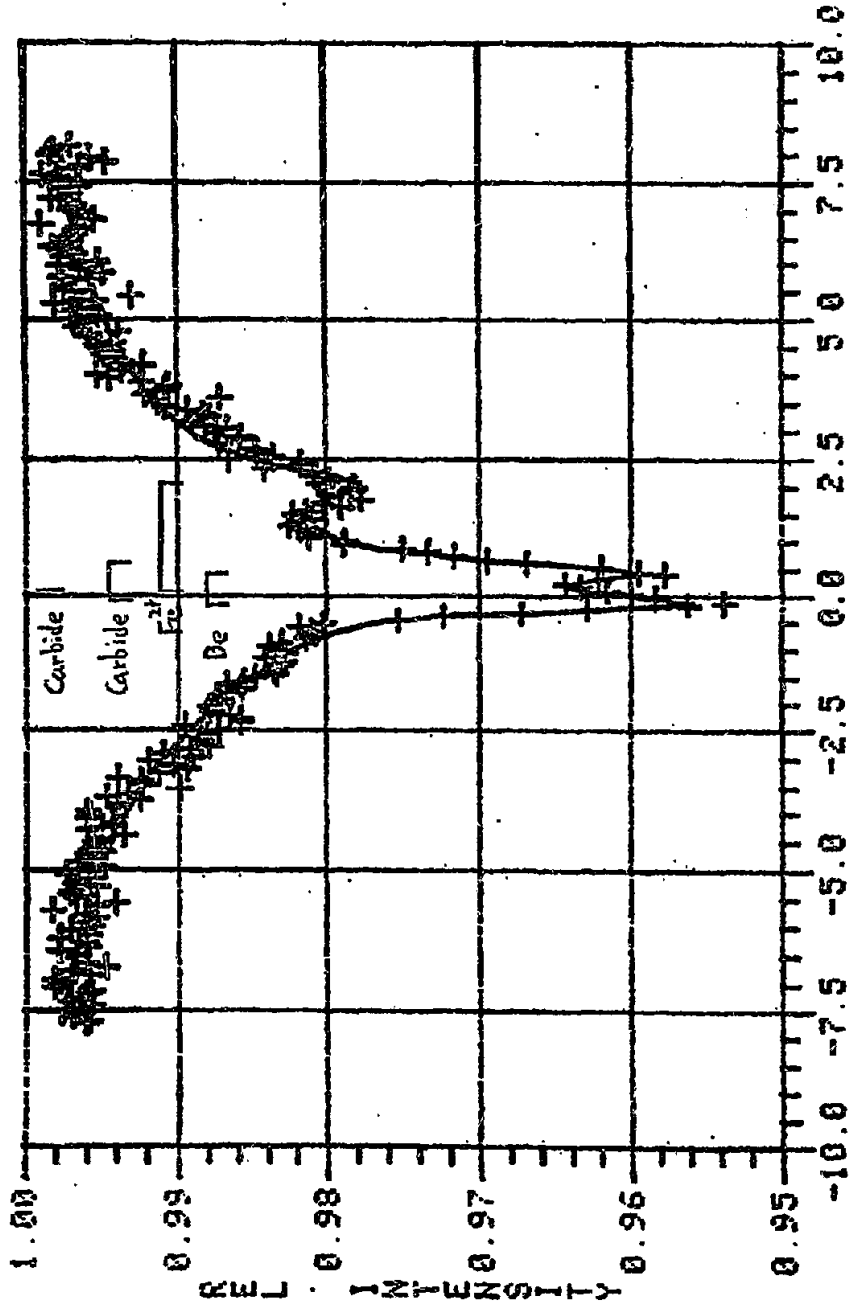


Figure 11

U<sub>2</sub>W



VELOCITY (MM/S)

Figure 12

U-W

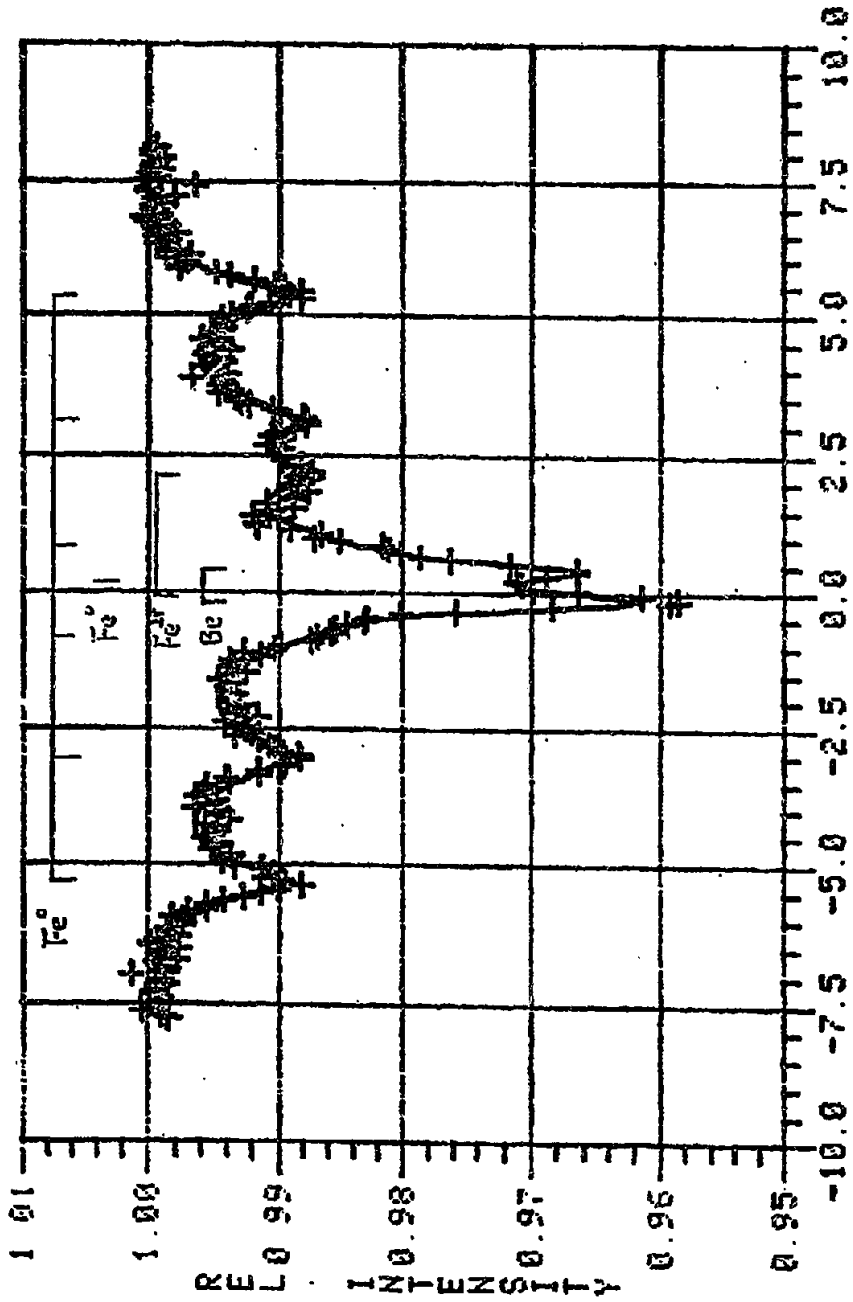


Figure 13

U-~~W~~W

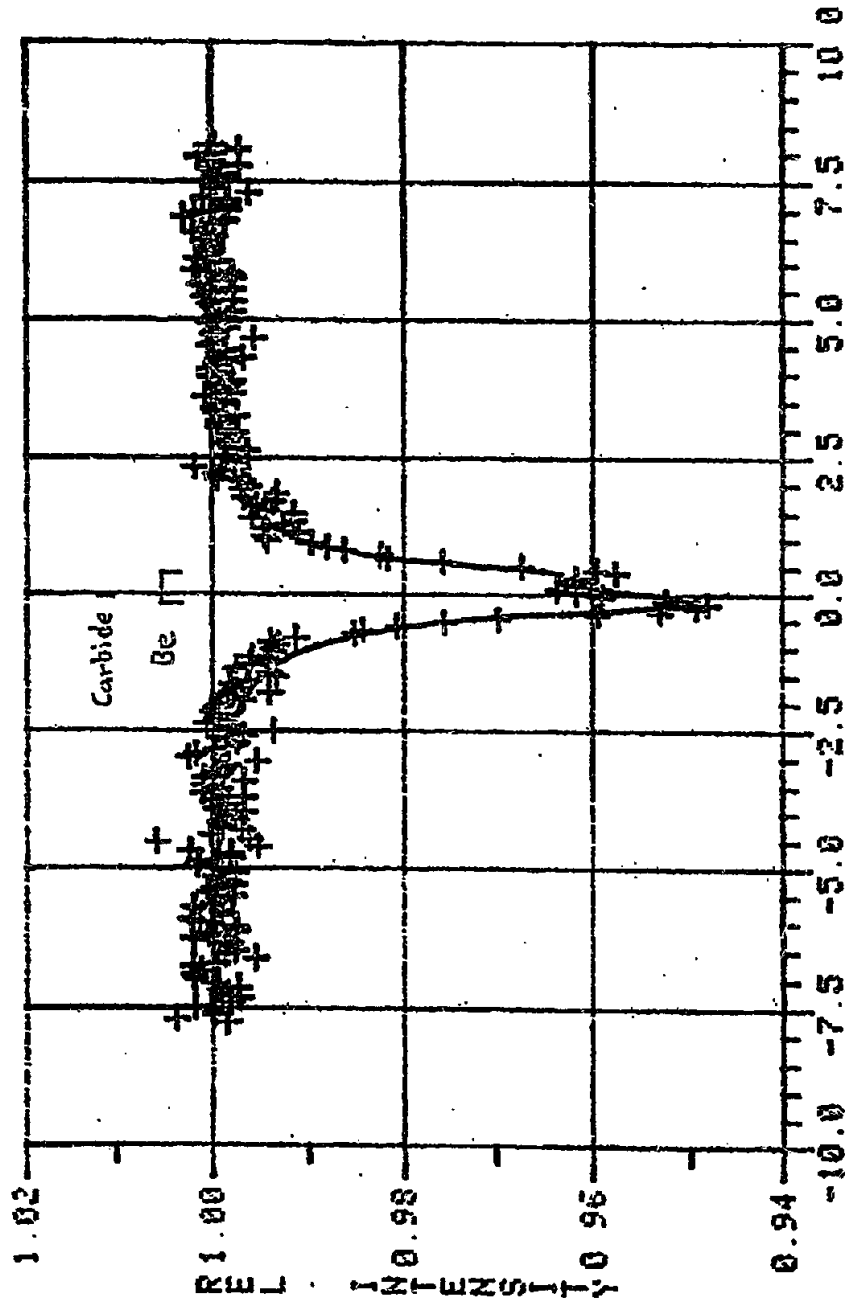


Figure 14

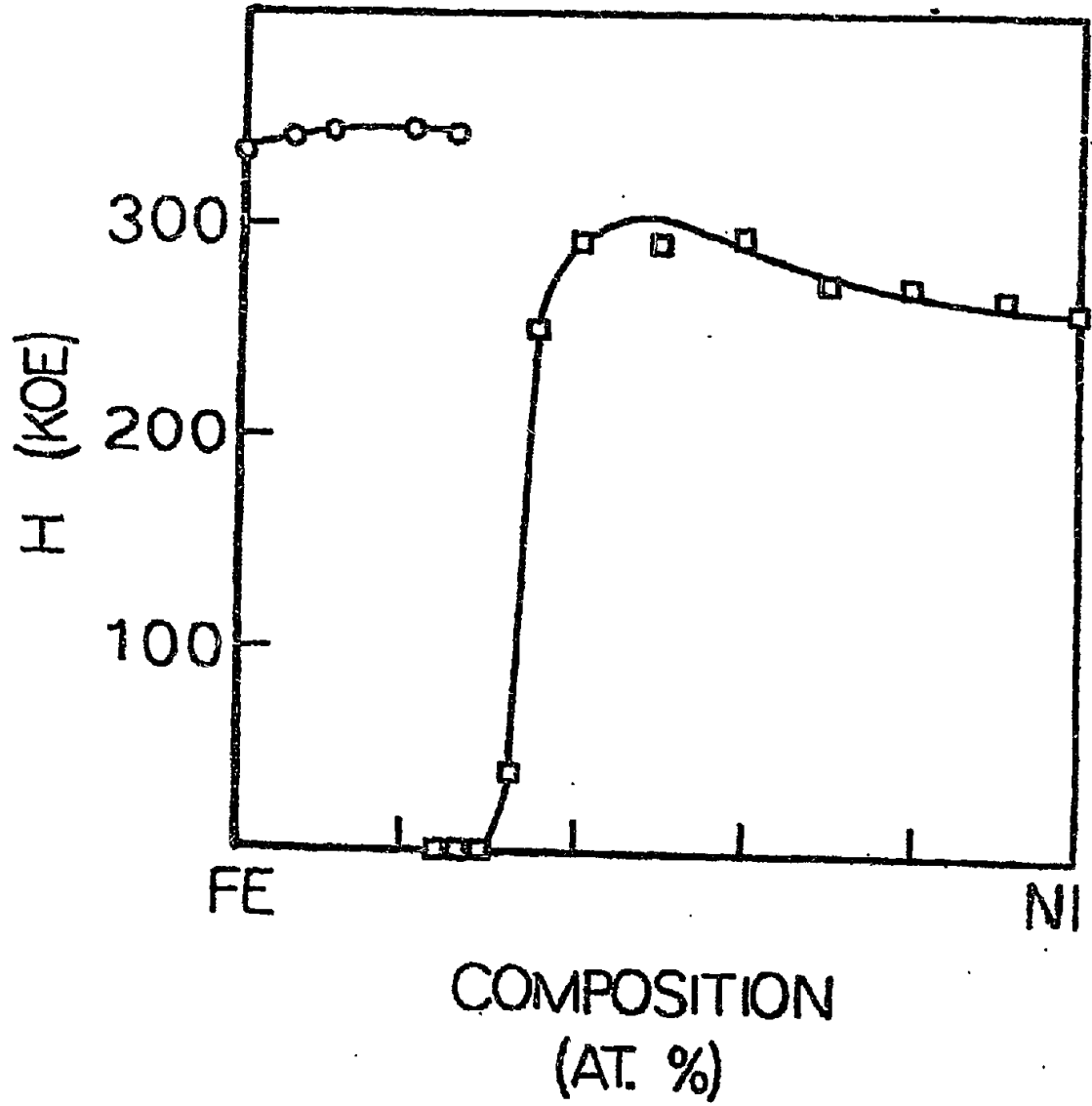


Figure 15

III. Appendix A\*

**Criteria for Stable Ni Particle Size under Methanation  
Reaction Conditions: Nickel Transport and Particle Size  
Growth via Nickel Carbonyl**

\* Revised from Semi-annual Progress Report, May 1980;  
and accepted for publication in the  
Journal of Catalysis.

## III.A. EXPERIMENTAL

III.A.1. High Pressure Reaction System

Kinetic data were measured in the all 316 stainless steel reaction system shown schematically in Fig. 1. The system can be operated at pressures up to 6.8 MPa. The reactor is made of a 1.27 cm O.D. x 1.02 cm I.D. tubing. The use of type 316 stainless steel prevents the formation of  $\text{Fe}(\text{CO})_5$ , and minimizes the formation of  $\text{Ni}(\text{CO})_4$  from the reaction between CO and the tube wall at high CO pressures and high temperatures (1). Composition changes of both reactant mixtures and effluent gases can be monitored continuously using a Gow-Mac high pressure thermal conductivity cell. The kinetic data were measured after the system had reached steady state, as determined by the steady voltage output from the thermal conductivity cell. The portion of the system downstream from the reactor was wrapped with heating tape to prevent water from condensing. Analyses of both effluent gases and reactant mixtures were carried out using a Carle Basic 8700 gas chromatograph operated at 388 K with 1.8 m of 80/100 mesh Spherocarb column.

Hydrogen (National Cylinder Gases) was purified by passage through a Deoxo unit followed by an activated 13X molecular sieve trap at room temperature. Carbon monoxide (Matheson, C.P. grade) was purified by passage through a system composed of a copper turning trap (with 60 cm of preheating section) at 593 K, and activated 3A and 13X molecular sieve traps at room temperature. Such an arrangement was effective in completely removing  $\text{Fe}(\text{CO})_5$  from the CO stream.

### III.A.2. Particle Size Determinations

Hydrogen chemisorption measurements were carried out in an all-glass high vacuum system described elsewhere (2). Prior to chemisorption measurements at room temperature, whether on fresh or used catalysts, the sample was reduced in flowing hydrogen (atmospheric pressure, 50-100 cm<sup>3</sup>/min) at 723 K for 1 h, evacuated for 1 h at this temperature and then cooled under vacuum to room temperature. Desorption isotherms, rather than adsorption isotherms, were measured, because hydrogen chemisorption on Ni involves a fast chemisorption process followed by a slow, activated chemisorption process (3-5). A similar procedure has been used for ruthenium (6) and nickel-copper catalysts (7). The amount of strongly adsorbed hydrogen was estimated by extrapolating the initial portion of the desorption isotherm back to zero pressure. X-ray diffraction measurements were made on a Picker biphenar diffractometer. Magnetization measurements were carried out using a Cahn RG microbalance and an Alpha model 4800 electromagnet.

### III.A.3. Catalyst Preparation and Treatment

Supported nickel catalysts were prepared by incipient wetness impregnation, using 0.6 ml of Ni(NO<sub>3</sub>)<sub>2</sub> solution per gram of 80/100 mesh  $\gamma$ -Al<sub>2</sub>O<sub>3</sub> powder (Davison, SMR-7). After impregnation, the catalysts were dried overnight at 393 K. The "standard" reduction procedure consisted of treating the catalyst in flowing hydrogen ( $P_{H_2} = 308$  kPa) while the sample temperature was (i) slowly increased to 403 K (over a period of 40 min), (ii) held at 403 K for 0.5 h, (iii) held at 533 K for 0.5 h, and (iv) held at 723 K for 2.5 h. The reactor temperature



and pressure were then adjusted to the desired values before the  $H_2/CO$  reactant mixture was introduced.

Space velocities (at reactor inlet conditions) of 40,000-60,000  $cm^3 \cdot g^{-1} \cdot h^{-1}$  were used to keep CO conversions low so that data analyses could be carried out in terms of a differential reactor model. A procedure similar to that used by Vannice (8) was used to maintain a "clean" metal surface. Specifically, after each datum point, CO flow was stopped and  $H_2$  alone was passed over the catalyst surface to effect catalyst regeneration. Typically, the catalyst was exposed to  $H_2/CO$  for approximately 0.5 h during the collection of each datum point; this was followed by a 2 h regeneration treatment in  $H_2$ . The exit gas was monitored by gas chromatography during this regeneration. It was established that the  $CH_4$  concentration in the  $H_2$  stream dropped to zero within the 2 h regeneration period.

Runs designated by the prefix "A" were carried out using a 10:1 mixture of 100/120 mesh  $\gamma-Al_2O_3$  powder and 80/100 mesh Ni/ $\gamma-Al_2O_3$  catalyst. The mixture was physically separated using a 100 mesh sieve after the kinetic studies. This separated catalyst was then used for x-ray diffraction and  $H_2$  chemisorption studies. The use of a diluted catalyst allowed the catalyst bed height to be kept nearly constant and CO conversions to be kept low between kinetic runs carried out over greatly different temperature ranges. In the deactivation studies (series A4), the catalyst was not regenerated using hydrogen flushing after each datum point, as had been the procedure in series 2 and 3. This approach made the deactivation

studies feasible within a reasonable time span.

Chemical analyses of catalyst samples were carried out by Galbraith Laboratories, Inc.

## III.B. RESULTS

Experimental conditions are summarized in Table 1. The first digit in the run number designates the batch number of the catalyst preparation. The prefix "A" means that the catalyst studied has been diluted with  $\gamma\text{-Al}_2\text{O}_3$  powder. The temperature in parentheses indicates the highest temperature recorded after the reactant mixture was introduced. Temperatures connected by the " $\rightarrow$ " sign indicate the temperature range studied using step temperature increments of 15 to 25 K from the lower limit to the upper limit. The "time on-stream" refers to the total period of time during which the catalyst was exposed to  $\text{H}_2/\text{CO}$  mixtures under specified conditions. The results of catalyst characterization are summarized in Table 2. The suffix "F" denotes a "fresh" catalyst, which has experienced only standard hydrogen reduction. The values of calculated metal loading are obtained from the concentration and volume of the impregnation solution and the amount of  $\gamma\text{-Al}_2\text{O}_3$  powder used for catalyst preparation. Since the height of the catalyst bed was typically 5.1 to 6.4 cm, it was possible to distinguish the upper portion from the lower portion of the catalyst bed. After kinetic studies, the catalyst was removed from the high pressure reactor. The first half of the catalyst poured out of the reactor was then labeled the upper portion of the catalyst bed, and the second half the lower portion of the catalyst bed. Such a differentiation between the upper and the lower portions of the catalyst bed was made for runs 2-4 and 3-1.

The rapid loss of activity for methanation at relatively high CO-pressure is shown in Fig. 2. These data are

characteristic of operation in an "unsafe" regime. Figure 3 shows typical results in the search for "safe" operating conditions. "Safe" operating conditions are defined as those for which the catalyst maintains a stable activity over a period of time long enough for kinetics studies (i.e., several hours exposure to a  $H_2/CO$  mixture). Similarly, the "unsafe" operating conditions are those under which the catalyst cannot maintain a stable activity. Thus, a temperature of 688 K is classified as safe, while temperatures of 526 K and 588 K are classified as unsafe, when  $P_{H_2} = 305$  kPa and  $P_{CO} = 18.6$  kPa (Fig. 3). The results of the search for safe operating conditions are shown in Fig. 4. For each partial pressure of CO, there is a lower limit in temperature for safe operating conditions. Above this threshold temperature the catalyst does not undergo rapid deactivation in terms of the time frame of our studies. The partial pressure of  $H_2$  plays only a minor role, if any, in the deactivation processes. The deactivation rate remained essentially unchanged when the  $H_2$  pressure was doubled for a run at 602 K and  $P_{CO} = 33.8$  kPa.

After the safe operating regime was mapped, several runs (the A4 series) were designed and carried out to study differences in catalyst structure after use in the safe and unsafe regimes. The most important differences in catalyst structure are those in Ni particle sizes, as determined by x-ray diffraction. The time on-stream is of only minor importance. As indicated in Table 2, the Ni particle sizes for the catalysts after operation in the safe regime

(runs 2-2, 2A-7, 2A-8, and 2A-11) ---

determined by x-ray diffraction, regardless of the time on-stream. X-ray diffraction was also unable to measure the Ni particle sizes in fresh samples (3F and 4F). On the other hand, the Ni particle sizes in the catalysts after operation in the unsafe regime (runs A4-6, A4-8 and A4-12) are always much larger than those in fresh samples. In addition, the Ni particle size in a catalyst after 16 hours of operation in the unsafe regime (run A4-8) was not much larger than those obtained after 3 hours of treatment in the unsafe regime (runs A4-6 and A4-12). The Ni particle size determinations using H<sub>2</sub> chemisorption always gave larger values than those obtained by x-ray diffraction (Table 2). The calculation of particle size based on H<sub>2</sub> chemisorption has taken into account the fact that not all the Ni present on the alumina support can be reduced to a metallic state. Magnetic measurements indicated that 72% of the Ni loading was reduced to the metallic state during the standard reduction procedure.

The kinetics of the methanation reaction were studied under safe operating conditions in separate experiments using an alumina-diluted catalyst (similar to the A4-series). Additional studies of the temperature (see Figure 5) and partial pressure dependence of the rate (not included in Table 1) indicate that the best fit of the data is of the form

$$r_{\text{CH}_4} = A e^{\left(\frac{-29000}{RT}\right)} P_{\text{H}_2}^{0.63} P_{\text{CO}}^{0.0} \quad (1)$$

where  $R = 1.987 \text{ cal/gmole}\cdot\text{K}$ .

### III.C. DISCUSSION

#### III.C.1. Nickel Transportation and Particle Size Growth

The calculated values of metal loading agree very well with the results of chemical analyses for runs 2-1, 2-3 and 4F. The small differences between calculated and analytical values in series A-4 are attributable to the physical separation technique employed. In contrast, the results of the chemical analyses for runs 2-2 and 2-4 are not in agreement with the calculated metal loadings. The Ni metal on the catalyst has been almost completely stripped from the catalyst bed in run 2-2. In run 2-4, the upper portion of the catalyst bed contained far less Ni metal than the calculated value of the metal loading, while the lower portion of the catalyst bed contained far more Ni metal than the calculated value of the metal loading. The average value of the results of the chemical analyses, 5.20%, indicates that there was probably no significant stripping of Ni from the catalyst bed. These phenomena show that Ni can be transported with the gas stream from the upper portion to the lower portion of the catalyst bed, and that, in the extreme case, Ni can even be stripped from the bed.

The results from run 3-1 show a more subtle effect of Ni transportation. On one hand, the results of the chemical analyses for run 3-1 indicate that there is only minor Ni transportation. The average value of the metal loading based on chemical analyses, 6.06%, agrees well with the value of the a priori calculation, 5.96%. A small amount of Ni, however, appears to have been transported from the

is the observation that the Ni particle sizes determined by x-ray diffraction are very large (23-43 nm) compared to the typical size of Ni particles in fresh catalysts (3-4 nm) (Table 2).

Two mechanisms have been proposed for the growth of metal particle sizes in supported catalysts (9): the crystal migration model and the interparticle transport model. The crystal migration model (10,11), envisages the growth in particle size as resulting from migration of metal particles over the support surface, followed by collision and coalescence. This model is not believed to be applicable for the conditions of the present study. Specifically, this mechanism requires a high mobility of metal particles on the surface of the support; however, the Tamman temperature of Ni, 964 K, is much higher than the temperatures involved in these runs. Indeed, particle mobility is not generally observed at temperatures below the Tamman temperature (12). Furthermore, this model is not consistent with the results of this study which show that particle size growth becomes less extensive as the temperature is increased (see Tables 2 and 3). For example, the Ni particle size in the catalysts used in runs A4-7, A4-9 and A4-11 (which have experienced temperatures as high as 741 K) is too small to be determined by x-ray diffraction indicating that the temperatures used in this study were not high enough to cause surface migration of metal particles. This conclusion is also supported by reported observations. Richardson and Crump (13) showed that the dispersion of a Ni/SiO<sub>2</sub> catalyst was very stable at 673 K in helium. Williams et al. (14) showed that the nickel

surface area of a coprecipitated Ni-Al<sub>2</sub>O<sub>3</sub> catalyst remained constant during a 1000 hour treatment at 673 K in a steam and hydrogen mixture. It also remained constant during treatment at 1073 K in hydrogen. Temperatures in both studies were higher than the temperatures employed in runs 2-2, 2-4 and 3-1.

The second model for particle size growth, the interparticle transport model (15,16) involves escape of atomic or molecular metal species from crystallites, migration of these species along the surface (or vapor phase transport), and their recapture by crystallites via collision or readsorption. A mechanism similar to the interparticle transport model is postulated to explain the phenomena observed in the present studies. Upon exposure to an appropriate H<sub>2</sub>/CO reactant mixture, the Ni metal particle reacts with adsorbed CO or with CO molecules in the gas phase to form Ni(CO)<sub>4</sub> species. The formation of Ni(CO)<sub>4</sub> from Ni on SiO<sub>2</sub> maintained in a CO atmosphere has been reported by Vannice and Garten (17). The formation of Ni(CO)<sub>4</sub> under room temperature CO chemisorption conditions indicates the ease with which it is formed (18). Van Neerten *et al.* (19) have in fact raised the possibility of having Ni(CO)<sub>4</sub> as an intermediate for the transport of Ni from small to large Ni particles in a Ni on SiO<sub>2</sub> catalyst. Product Ni(CO)<sub>4</sub> molecules can leave the metal particle and diffuse through the gas phase and/or over the catalyst support. Depending on the operating conditions, these species then decompose to metallic Ni on either a nearby Ni particle or a Ni particle on a catalyst granule downstream from the original. Indeed, Ni(CO)<sub>4</sub> partially decomposes at temperatures as low

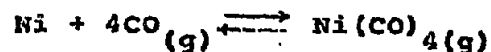


tion of Ni catalysts by decomposing  $\text{Ni}(\text{CO})_4$  on  $\text{Al}_2\text{O}_3$  fibers at 473 K. The industrial production of high purity Ni pellets is carried out by decomposing  $\text{Ni}(\text{CO})_4$  at 443-523 K (22). Temperatures employed in most of our runs are higher than these decomposition temperatures. Finally, under certain conditions, the  $\text{Ni}(\text{CO})_4$  molecules may even be flushed out of the reactor, causing the stripping of Ni metal from the catalyst bed as will be discussed later.

As pointed out earlier, one of the prominent differences between catalysts after operation in the safe regime and catalysts after operation in the unsafe regime is the Ni particle size determined by x-ray diffraction. After 16 hours of treatment at 653 K in the safe regime (run A4-9) a catalyst still has a Ni particle size comparable to that of a fresh sample. However, after 3 hours of treatment at lower temperatures in the unsafe regime (run A4-6) a catalyst shows a five-fold increase in Ni particle size relative to fresh samples. As can be seen in Tables 1 and 2, the correlating factors are (i) the CO partial pressure, which was higher in the unsafe treatments than in the safe treatments, and (ii) the temperature, which was lower in the unsafe treatments than in the safe treatments. Thermodynamically the higher CO pressure and the lower temperature used in the unsafe treatment favor the formation of  $\text{Ni}(\text{CO})_4$ . These data are consistent with the argument that the deactivation proceeds via the interparticle transport model rather than via the crystallite migration model.

### III.C.2. Kinetic and Thermodynamic Aspects of Ni(CO)<sub>4</sub> Formation

Thermodynamic data for the reaction



are available in the literature (23-27). The data summarized by Goldberger and Othmer (26) were used for calculating equilibrium partial pressures of Ni(CO)<sub>4</sub>. The calculated values are tabulated in Table 3.

Goldberger and Othmer (26) found that the rate of Ni(CO)<sub>4</sub> formation reaches a maximum at 348 K at all CO pressures studied, while Kipnis and Mikhailova (28,29) have determined the kinetic rate expression for this reaction. Accordingly, for all runs in the present study, the rate of Ni(CO)<sub>4</sub> formation would be approximately 10<sup>-6</sup> mole/cm<sup>2</sup>.h in the absence of gaseous Ni(CO)<sub>4</sub>. This corresponds to about 10<sup>2</sup> monolayers of Ni removed from each Ni particle per hour. (These kinetic data are only semiquantitative due to the fact that a much larger Ni particle size, 38 μ, was used in the studies of Kipnis and Mikhailova (28,29).) Yet, small Ni particles (consisting of several tens of monolayers) are in fact stable for long times in runs 3-2, A4-11, A4-9 and A4-7. Thus, the kinetics of Ni(CO)<sub>4</sub> decomposition must also be considered to interpret the phenomena of the present study. In short, it has been found (30-33) that the rate increases with increasing temperature up to approximately 400 K, while above this temperature the rate-determining step in the thermal decomposition is the gas phase diffusion of Ni(CO)<sub>4</sub> to the surface of metallic nickel (30,32). In other words, the intrinsic rate of Ni(CO)<sub>4</sub> decomposition on metallic Ni at temperatures higher than ca. 400 K is fast compared to the rate

of gas phase diffusion of  $\text{Ni}(\text{CO})_4$  to the Ni surface. In the present case, the fast rates of  $\text{Ni}(\text{CO})_4$  formation and decomposition suggest that thermodynamic equilibrium with respect to formation of  $\text{Ni}(\text{CO})_4$  from nickel and carbon monoxide is achieved at the surface of the Ni particles during methanation.

The equilibrium partial pressures of  $\text{Ni}(\text{CO})_4$  vary from 67 Pa for the run in which Ni was stripped from the catalyst bed to  $1.3 \times 10^{-8}$  Pa for a run in the safe regime. Under those conditions for which the thermodynamics of  $\text{Ni}(\text{CO})_4$  formation are unfavorable (small  $\text{Ni}(\text{CO})_4$  partial pressure), the flux of  $\text{Ni}(\text{CO})_4$  away from each Ni particle is expected to be small. The Ni particle size distribution is then stable, because the various particles do not exchange nickel via  $\text{Ni}(\text{CO})_4$  transport. When the reaction conditions are changed such that the  $\text{Ni}(\text{CO})_4$  partial pressure at the Ni surface is increased, the flux of  $\text{Ni}(\text{CO})_4$  away from the Ni particles is expected to increase. However, as long as the decomposition of  $\text{Ni}(\text{CO})_4$  is fast compared to the rate of diffusion, the  $\text{Ni}(\text{CO})_4$  will subsequently decompose near the site at which it was formed. This provides a mechanism for exchange of Ni between neighboring Ni particles. There would not be any growth in particle size if  $\text{Ni}(\text{CO})_4$  decomposed at the same rate on Ni particles having different sizes. However, the rate at which a particle gains metal atoms by the processes described in the interparticle transport model is proportional to the effective diameter of the particle (15). Kipnis and Mikhailova (25) have reported that nickel carbonyl is easier to form from smaller Ni particles. Hence one expects larger particles to grow at the expense of smaller ones, and this is the mechanism by which the Ni particle size

This expectation is confirmed by observations of Evans and Simpson (34) on an industrial process producing Ni pellets via decomposition of  $\text{Ni}(\text{CO})_4$ . Finally, as the temperature is decreased, the intrinsic rate of  $\text{Ni}(\text{CO})_4$  decomposition decreases faster than the rate of  $\text{Ni}(\text{CO})_4$  diffusion. This allows the  $\text{Ni}(\text{CO})_4$  to diffuse and decompose further from the site at which it was originally formed. At sufficiently low temperatures, the  $\text{Ni}(\text{CO})_4$  would be able to diffuse out of the catalyst granule in which it was formed, and then be decomposed in another granule further downstream in the catalyst bed. In the limiting case of slow intrinsic rates of  $\text{Ni}(\text{CO})_4$  decomposition, the  $\text{Ni}(\text{CO})_4$  would be swept from the catalyst bed by the gas flowing through the reactor.

Inspection of Table 3 shows that the experimental observations are in accord with the above arguments. The various experimental runs are listed in the order of decreasing equilibrium  $\text{Ni}(\text{CO})_4$  partial pressures for the temperatures and CO partial pressures used in the methanation studies. The presence of an asterisk as an entry in the table indicates that one or more of the following phenomena were observed in the run in question: (i) loss of Ni from the catalyst bed, (ii) transport of Ni down the catalyst bed, (iii) growth of Ni particle size, and (iv) stable nickel particle size and catalytic activity.

It can be seen that those runs with the highest  $\text{Ni}(\text{CO})_4$  partial pressures combined with the slowest intrinsic  $\text{Ni}(\text{CO})_4$  decomposition rates showed the most dramatic effects of Ni transportation. (The intrinsic rate of  $\text{Ni}(\text{CO})_4$  decomposition

which increases with increasing temperature, is used for comparison among various runs, since the effects of  $\text{Ni}(\text{CO})_4$  diffusion are considered separately.) For example, the conditions of run 2-2 corresponded to the highest equilibrium  $\text{Ni}(\text{CO})_4$  partial pressure with the slowest  $\text{Ni}(\text{CO})_4$  decomposition rate, and significant loss of Ni from the catalyst bed was observed in this run. Run 2-4 had a smaller  $\text{Ni}(\text{CO})_4$  equilibrium partial pressure with a higher  $\text{Ni}(\text{CO})_4$  decomposition rate; less removal of Ni from the bed was observed. On the other hand, significant transport of Ni down the catalyst bed was observed during this run. The equilibrium  $\text{Ni}(\text{CO})_4$  partial pressure of run 3-1 was still lower while the  $\text{Ni}(\text{CO})_4$  decomposition rate was higher; less extensive Ni transport down the catalyst bed was observed, compared to run 2-4. Furthermore, no loss of Ni from the catalyst bed was observed for run 3-1. The conditions of runs A4-8, A4-6 and A4-12 gave equilibrium  $\text{Ni}(\text{CO})_4$  partial pressures lower than run 3-1. Accordingly, no transport of Ni out of the catalyst bed or down the catalyst bed was observed. However, the Ni particles were observed to increase in size under these reaction conditions. That is, the equilibrium  $\text{Ni}(\text{CO})_4$  partial pressure was still high enough to allow Ni particles within a given catalyst granule to exchange matter via  $\text{Ni}(\text{CO})_4$  transport. Finally, the lowest equilibrium  $\text{Ni}(\text{CO})_4$  partial pressures were those of runs 3-2, A4-11, A4-9 and A4-7. Indeed, the size of Ni particles did not increase and the catalysts maintained stable activity during each of these runs. The temperatures and CO partial pressures of these runs correspond to safe operating conditions.

Figure 4 shows calculated equilibrium partial pressure curves for  $\text{Ni}(\text{CO})_4$  as a function of temperature and CO partial pressure. The equilibrium curve for  $P_{\text{Ni}(\text{CO})_4} = 1.0 \times 10^{-6}$  Pa outlines the border between the safe operating regime and the unsafe regime. This is to be expected, because, as mentioned earlier, thermodynamics plays an important role in determining the conditions for safe operation. Thus, the equilibrium partial pressure of  $\text{Ni}(\text{CO})_4$  can be used as an empirical criterion for determining the "safety" of a given set of operating conditions.

Similar deactivation behavior has been observed for a commercial 30% Ni/ $\alpha\text{-Al}_2\text{O}_3$  catalyst (35) and a 5% Ni/ $\text{Al}_2\text{O}_3$  monolithic catalyst (36). The corresponding equilibrium  $\text{Ni}(\text{CO})_4$  partial pressures are  $7.18 \times 10^{-2}$  Pa and  $2.7 \times 10^{-6} - 1.3 \times 10^{-5}$  Pa, respectively. These values are larger than the suggested safe value of  $1.0 \times 10^{-6}$  Pa. Van Meerten et al. (19) have recently shown by magnetization measurements that the Ni particle size of a 4.88% Ni/ $\text{SiO}_2$  catalyst grows gradually during methanation. The equilibrium  $\text{Ni}(\text{CO})_4$  partial pressure corresponding to their operating conditions is  $4.0 \times 10^{-6}$  Pa. These facts suggest that the present criterion for judging the "safety" of operating conditions can be applied to other systems with higher metal loadings and/or different geometry. The previously stated conclusion concerning the insensitivity of this deactivation process to the hydrogen partial pressure is also supported by these studies. Vannice and Garten (35) used a partial pressure of  $\text{H}_2$  which is twice that employed in this study. Bartholomew (36) found no difference in deactivation behavior

### III.C.3. Blockage of Surface Sites

For  $\text{Al}_2\text{O}_3$ -supported catalysts the larger Ni particle sizes determined by hydrogen chemisorption relative to those determined by x-ray diffraction have been previously attributed to metal-support interactions, e.g. formation of a surface spinel (37). Hence, magnetization measurements were used to study the reducibility of a typical Ni/ $\text{Al}_2\text{O}_3$  catalyst. After the standard reduction procedure a catalyst showed 72% reducibility (run 4F). This value was used to correct the metal loadings used for calculating the particle size based on  $\text{H}_2$  chemisorption. For a freshly reduced sample (4F) the particle size determined by  $\text{H}_2$  chemisorption is 3.2 nm, a value which agrees very well with those determined by magnetization measurements. The Langevin low-field estimate at 300 K gives 3.4 nm, while the Langevin high-field estimate at 77 K gives 2.8 nm. However, after exposure to  $\text{H}_2/\text{CO}$  reaction mixtures, the reducibility-corrected Ni particle sizes determined by hydrogen chemisorption are consistently larger than those determined by x-ray diffraction. The difference is too large to be attributed to experimental uncertainty and it cannot be explained by the presence of a particle size distribution. The catalyst surface must be blocked, probably by carbon deposition.

In estimating the percentage coverages of the surface (see Table 2), it is assumed that the actual Ni particle size after operation in the safe regime is the same as that for run 4F, and that the Ni particles are spherical. The first assumption is suggested by the fact that these catalysts are indistinguishable by x-ray diffraction measurements. The x-ray diffraction data, however, were suggestive of nonspherical particles in some cases.

While the assumption of a spherical particle shape may invalidate the quantitative aspects of the surface coverage calculations, the qualitative trends in the values for catalysts exposed to different operating conditions can still be observed. (It is noted that the calculated surface coverages are sensitive to the particle shape assumed.) In short, the extent of surface blockage (by carbon) is approximately the same, after catalyst operation in either safe or unsafe regimes. This adds further support to the belief that the primary difference between the safe and unsafe operating conditions is the extent of Ni particle growth, and not differences in the extent of surface coverage by carbon.

#### III.C.4. Methanation Kinetics

The Arrhenius plots shown in Figure 5 indicate that the catalyst activity decreased by only 50% after 21 days on-stream. The activation energy increased by 25 kJ/mole during this mild deactivation process. The activation energy for methane formation is presently reported to be 121 kJ/mole, instead of 96 kJ/mole, because most of the kinetic data were collected after long times on-stream. This value is within the range of reported values for  $\text{Al}_2\text{O}_3$  supported Ni catalysts (37). The dependence of the rate on reactant partial pressures is somewhat different from those reported for kinetic studies at lower temperatures (37). However, for methanation, as the results of Bartholomew (36) indicate, the partial pressure dependence is a function of the



temperature studied. For purposes of comparison the turnover numbers for methane formation are extrapolated and reported at the conditions used by Vannice (37). For catalysts employed in the safe region (runs A4-9 and A4-11), the values agree well with reported values. However, for catalysts employed in the unsafe region (runs A4-6 and A4-8) the values are an order of magnitude lower than reported values, although they agree with each other. In run A4-12, the catalyst had first experienced the same treatments as employed in run A4-6 (see Table 1). The catalyst was then brought into the safe region. The turnover number for the datum point collected in the safe region was indistinguishable from those for catalysts that never had been exposed to operation in the unsafe regime. This fact may indicate that the mechanism of methanation in the unsafe region is different from that in the safe region. Consequently, the use of the rate expression determined from operation in the safe region for data extrapolation of runs in the unsafe regime can give erroneous results.

## III.D. CONCLUSIONS

The conditions of the present study can be divided into two different operating regimes. In the "safe" regime, the nickel particles are stable against increases in size and the catalytic activity for methanation is constant with time. In the "unsafe" regime, the catalyst deactivates with time due to the increase in Ni particle size. Approximately 50% of the Ni surface is covered by inactive carbon, but this is the same during operation of the catalyst in both safe and unsafe regimes. Particle size growth in Ni/Al<sub>2</sub>O<sub>3</sub> methanation catalysts during operation in the unsafe region results from the formation of Ni(CO)<sub>4</sub>, diffusion of this species through the gas phase and/or over the catalyst surface, and subsequent decomposition of Ni(CO)<sub>4</sub>. Thermodynamic considerations can be used to predict whether a given set of reaction conditions correspond to the safe or unsafe regimes of operation. Specifically, conditions for which the equilibrium partial pressure of Ni(CO)<sub>4</sub> is less than ca. 10<sup>-6</sup> Pa will give stable methanation activity for catalysts consisting of nickel on alumina. Conversely, reaction conditions giving much higher equilibrium partial pressures of Ni(CO)<sub>4</sub> will lead to transport of nickel through the catalyst bed and ultimately to the removal of nickel from the catalytic reactor. In addition, the mechanism of methanation in the unsafe regime may be different from that in the safe regime.

## III.E. REFERENCES

1. Inouye, H., and DeVan, J. H., *J. Mater. Energy Syst.* 1, 52 (1979)
2. Lund, C. R. F., Schorfheide, J. J., and Dumesic, J. A., *J. Catal.* 57, 105 (1979)
3. Schuit, G. C. A., and DeBoer, N. H., *Rec. Trav. Chim., Pays-Bas*, 70, 1067 (1951)
4. Rostrup-Nielsen, J. R., "Steam Reforming Catalyst", Teknisk Forlag A/S, Copenhagen (1975)
5. Bartholomew, C. H., and Farrauto, R. J., *J. Catal.* 45, 41 (1976)
6. Dalla Betta, R. A., *J. Catal.* 34, 57 (1974)
7. Dalmon, J. A., *J. Catal.* 60, 325 (1979)
8. Vannice, M. A., *J. Catal.* 37, 449 (1975)
9. Wynblatt, P., and Gjostein, N. A., *Prog. Solid State Chem.* 9, 21 (1975)
10. Ruckenstein, E., and Pulvermacher, B., *AIChE J.* 19, 356 (1973)
11. Ruckenstein, E., and Pulvermacher, B., *J. Catal.* 29, 224 (1973)
12. Baker, R. T. K., *Catal. Rev.-Sci. Eng.* 19, 161 (1979)
13. Richardson, J. T., and Crump, J. G., *J. Catal.* 57, 417 (1979)
14. Williams, A., Butler, G. A., and Hammonds, J., *J. Catal.* 24, 352 (1972)
15. Flynn, P. C., and Wanke, S. E., *J. Catal.* 34, 390 (1974)
16. Flynn, P. C., and Wanke, S. E., *J. Catal.* 34, 100 (1974)
17. Vannice, M. A., and Garten, R. L., *J. Catal.* 56, 236 (1979)

18. Bartholomew, C. H., "Quarterly Technical Progress Report" for Dept. of Energy, Contract No. EF-77-S-01-2729 (July 1979).
19. Van Meerten, R. Z. C., Habets, H. M. J., Beaumont, A. H. G. M., and Coenen, J. W. E., The 7th International Congress on Catalysis, Prepr. D7, Tokyo, Japan (1980)
20. Syrkin, V. G., Vasilenok, E. M., and Tolmasskii, I. S., Porosh. Met. 3, 6 (1970)
21. Derouane, E. G., Nagy, J. B., and Védrina, J. C., J. Catal. 46, 434 (1977)
22. Forman, H. R., U.S. Pat. 3,826,225 (July 30, 1974)
23. Syrkin, V. G., Russ. J. Phys. Chem. 48, 1718 (1974)
24. Ross, L. W., Haynie, F. H., and Hochman, R. P., J. Chem. Eng. Data 9, 339 (1964)
25. Kipnis, A. Ya., and Mikhailova, N. F., Zh. Prikl. Khim. 45, 1450 (1972)
26. Goldberger, W. M., and Ottman, D. F., Ind. Eng. Chem., Process Des. Dev. 2, 202 (1963)
27. Spice, J. E., Staveley, L. A. K., and Harrow, G. A., J. Chem. Soc. 100 (1955)
28. Kipnis, A. Ya., Mikhailova, N. F., and Ravdel, E. A., Kinet. Katal. 8, 803 (1967)
29. Kipnis, A. Ya., and Mikhailova, N. F., Kinet. Katal. 12, 1397 (1971)
30. Carlton, H. E., and Oxley, J. H., RICHE J. 13, 86 (1967)
31. Kalitovich, I. M., Kipnis, A. Ya., Mikhailova, N. F., and Taganov, D. N., Zh. Prikl. Khim. 47, 43 (1974)
32. Tsylov, B. A., Porosh. Met. 5, 21 (1971)
33. Goosen, A. J. and Van der Berg, J. A., J. S. African Chem. Inst. 25, 370 (1972)
34. Evans, D., and Simpson, A. B., U.S. Pat. 3,844,251 (Oct. 29, 1974).

35. Vannice, M. A., and Garten, R. L., Ind. Eng. Chem., Prod. Res. Dev. 18, 186 (1979).
36. Bartholomew, C. H., "Quarterly Technical Progress Report" for Dept. of Energy, Contract No. EF-77-S-01-2729 (Jan. 1980).
37. Vannice, M. A., J. Catal. 44, 152 (1976)

Table 1: Experimental Conditions

Run No.	Temp. (K)	Pressure (kPa)		H <sub>2</sub> /CO ratio	Time on-stream (min)	Oper- ating Regime	
		H <sub>2</sub>	CO				
2-2	397 → 477	365	123	2.98	132	Unsafe	
	723 rereduction				60		
	474 → 580	378	121	3.12	202		
2-4	428 → 543	381	124	3.07	140	Unsafe	
	723 rereduction				150		
	523 → 598	381	124	3.07	64		
	423	381	124	3.07	22		
2-3	446 → 561	355	117	3.03	236	Unsafe	
	723 rereduction				150		
	457 → 555	352	118	2.99	83		
2-1	527 (728)	461	150	3.07	26	Unsafe	
	485 → 529	436	145	3.01	252		
3-1	473	334	79	4.22	100	Unsafe	
	723 rereduction				150		
	473	334	79	4.22	29		
	499	334	79	4.22	49		
A4-8	513	307	85	3.59	930	Unsafe	
	562	307	85	3.59	22		
	590	307	85	3.59	17		
A4-6	523	307	85	3.59	124	Unsafe	
	547	307	85	3.59	26		
	573	307	85	3.59	17		
A4-12	524	296	81	3.68	128	Unsafe	
	549	292	80	3.66	27		
	572	292	80	3.66	23		
	655	294	17.9	16.4	33		Safe
	639 H <sub>2</sub> flushing				72		
	647	294	17.2	17.1	24		
3-2	521 (576)	345	18.6	18.5	44	Safe	
	522 (575)	345	19.3	17.9	1487		
A4-11	644	300	17.2	17.4	54	Safe	
	741	277	40.7	6.81	50		
	577	300	17.2	17.4	61		
A4-9	633	298	19.3	15.4	930	Safe	
	638	298	19.3	15.4	45		
A4-7	651	302	17.9	16.8	49	Safe	
	741	285	42.0	6.77	54		

Table 2: Catalyst Characterization

Run No.	Metal Loading (wt %) <sup>1)</sup>		Particle Size (nm)		Surface Coverage (%)	$N_{CH_4}$ (sec <sup>-1</sup> ) <sup>3)</sup>
	Calculated	Analytical	XRD (111)	Chemisorption <sup>2)</sup> (200)		
2-2	5.73	0.95	**5)	-	-	-
2-4 upper bed	5.73	3.89	50.3	61.6	-	-
2-4 lower bed	5.73	6.51	39.5	35.4	-	-
2-3	5.73	5.63	40.1	53.3	-	-
2-1	5.73	5.75	33.0	34.9	-	-
3-1 Upper bed	5.96	5.78	36.9	23.7	-	-
3-1 lower bed	5.96	6.34	43.1	23.7	-	-
4-8	5.98	5.44	20.7	12.3	58.1	$1.5 \times 10^{-3}$
4-6	5.98	5.45	16.4	*	19.8	$4.1 \times 10^{-3}$
4-12	5.98	-	15.4	*	38.1	$25.0 \times 10^{-3}$
4-2	5.96	-	*4)	-	-	-
4-11	5.98	-	*	-	7.6	$31.4 \times 10^{-3}$
4-9	5.98	5.64	*	-	6.5	$25.0-42.6 \times 10^{-3}$
4-7	5.98	5.82	*	-	6.7	53
4	5.96	-	*	-	4.0	-
4	5.98	6.00	*	-	3.2	-

Table 2 continued

- (1) Based on dried-reduced samples.
- (2) Assuming spherical particles and 72% reduction (as determined by magnetization measurements). Ni atom area =  $6.78 \text{ \AA}^2$  (the average of (100), (110) and (111) planes). If possible, the values of metal loadings determined by chemical analyses were used for the particle size calculations. For samples 3F, A4-11 and A4-12, the calculated metal loadings were used to calculate Ni particle sizes.
- (3) Turnover numbers are extrapolated to  $T = 548 \text{ K}$ ,  $P = 101.3 \text{ kpa}$  and  $H_2/CO = 3$  using Eq. (1).
- (4) An asterisk denotes that no particle-size determination can be made because the peak is too broad. In most cases, the extremely broadened Ni diffraction peak cannot even be distinguished from background.
- (5) No Ni diffraction peak can be observed because there is not enough Ni in the sample.



Table 3: Thermodynamic Calculations of Ni(CO)<sub>4</sub>

Run No.	Temp. (K) 1)	P <sub>CO</sub> (kPa)	P <sub>Ni(CO)<sub>4</sub></sub> (Pa) 2)	Loss of Ni from Bed	Transport of Ni Down the Bed	Ni Particle Size Growth 3)	Stable Catalytic Activity
2-2	397	123	67	*	-	-	-
2-4	423	124	47	*	*	*	-
2-3	446	117	4.5	-	-4)	*	-
2-1	485	145	0.46	-	-4)	*	-
3-1	473	79.2	0.10	-	*	*	-
A4-8	513	85.5	8.0x10 <sup>-3</sup>	-	-	*	-
A4-6	523	85.5	4.2x10 <sup>-3</sup>	-	-	*	-
A4-12	524	80.6	3.1x10 <sup>-3</sup>	-	-	*	-
3-2	576	18.6	4.6x10 <sup>-7</sup>	-	-	-	*
A4-11	577	17.2	3.2x10 <sup>-7</sup>	-	-	-	*
A4-9	653	19.3	1.6x10 <sup>-8</sup>	-	-	-	*
A4-7	651	17.9	1.3x10 <sup>-8</sup>	-	-	-	*

- (1) The lowest temperature in each run.
- (2) Equilibrium partial pressure of nickel carbonyl based on calculated equilibrium constant.
- (3) x-ray diffraction peak observable.
- (4) Separation of the upper from the lower portions of the catalytic bed was not attempted.

## FIGURE CAPTIONS

Fig. 1 Schematic Diagram of the all Stainless-steel System for High Pressure Kinetics Studies (most on-off valves omitted).







-  : on-off valve
-  : regulating valve
-  : check valve
-  : safety head
-  : three way valve
-  : pressure gage
- 1 : Deoxo unit
- 2 : copper turning trap
- 3 : 3A molecular sieve trap
- 4 : 13X molecular sieve trap
- 5 : filter with 2  $\mu$  filter element
- 6 : Tylan FM-360 flowmeter with readout box RO-14
- 7 : Chatham precision needle valve
- 8 : Grove 90W back pressure regulator
- 9 : Grove 15S small volume regulator
- 10 : Gow-Mac 10-454-25 WX thermal conductivity cell with 40-001 power supplier
- 11 : Valco V-6-HPaX C20 sampling valve
- 12 : Linberg 54356-V three-zone furnace with 59744-A control console
- 13 : 316 S.S. tubular reactor
- 14 : Valco CV-8-HPaX C20 sampling valve
- 15 : auxiliary exit, which can be connected to wet test meter for flowmeter calibration

Fig. 2 Rapid Loss of Catalytic Activity for Methanation (run 3-1) at 470 K (o) and 500 K ( $\Delta$ ).

X's are used for points where  $\text{CH}_4$  peaks were so small that they were not integrated by the electronic integrator. Vertical lines on the abscissa denote catalyst regenerations (ca. 2 h) in flowing hydrogen. The catalyst was typically exposed to  $\text{H}_2/\text{CO}$  reactant mixture for 0.5 h between hydrogen regenerations.

Fig. 3. Safe and Unsafe Operation Conditions for  $\text{Ni}/\text{Al}_2\text{O}_3$  Catalyst.

$$P_{\text{H}_2} = 305 \text{ kPa}, P_{\text{CO}} = 18.6 \text{ kPa}$$

(i)  $T = 526 \text{ K}$  (o)

(ii)  $T = 588 \text{ K}$  (o)

(iii)  $T = 688 \text{ K}$  ( $\Delta$ )

Fig. 4. A Map of the Region of Safe Operating Conditions for  $\text{Ni}/\text{Al}_2\text{O}_3$  Catalysts.

o: Safe Operating Conditions

$\square$ : Unsafe Operating Conditions

The equilibrium curves for various equilibrium partial pressures of  $\text{Ni}(\text{CO})_4$  are calculated using thermodynamic data available in the literature.

Fig. 5. Arrhenius Plots for  $\text{Ni}/\text{Al}_2\text{O}_3$ .

$$P_{\text{CO}} = 35.8 \text{ kPa}$$

$$P_{\text{H}_2} = 257 \text{ kPa}$$

o: data collected on the first day

$$(E_A = 96 \text{ kJ/mole})$$

o: data collected after catalyst had

$$(E_A = 121 \text{ kJ/mole})$$

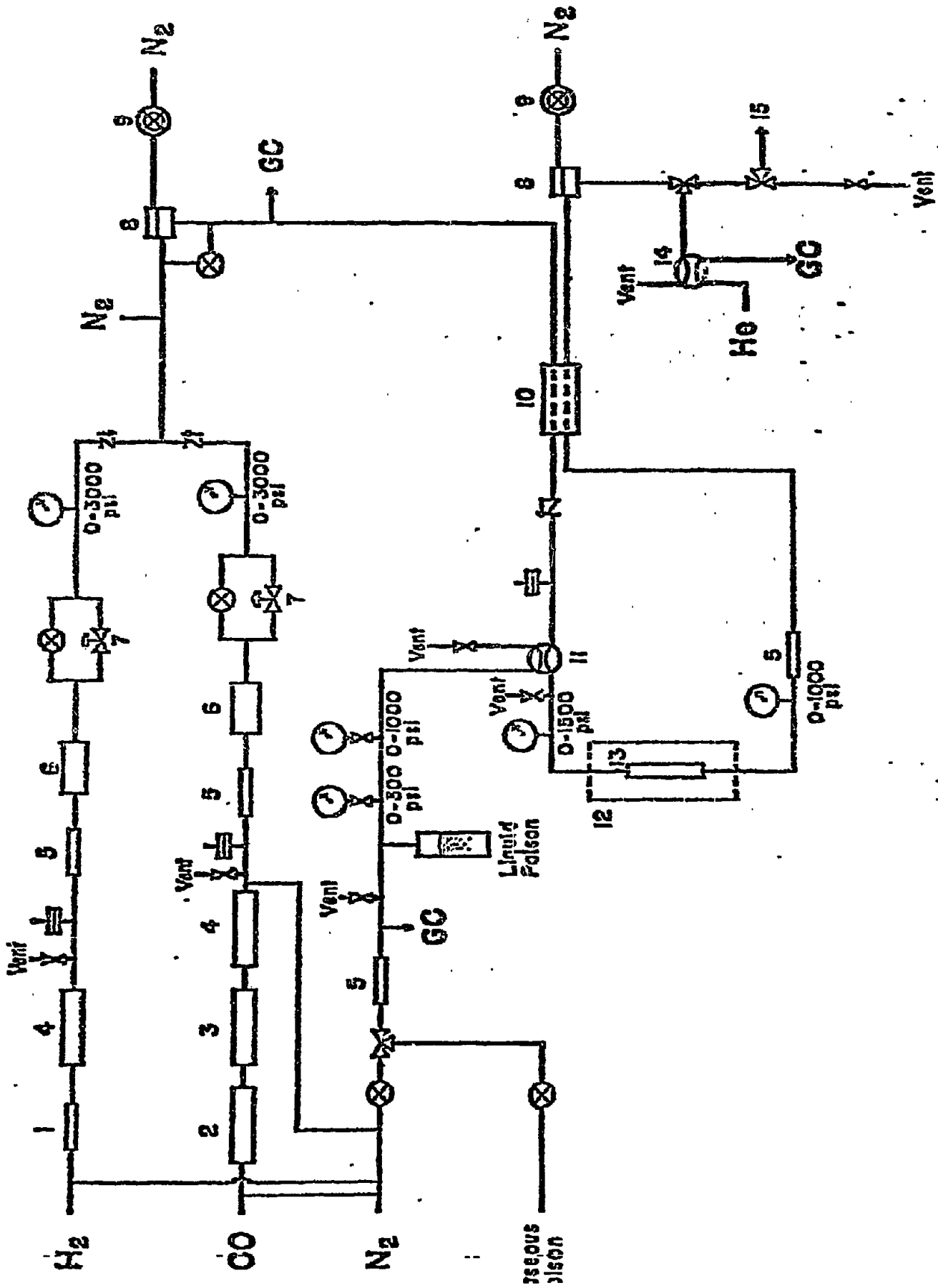
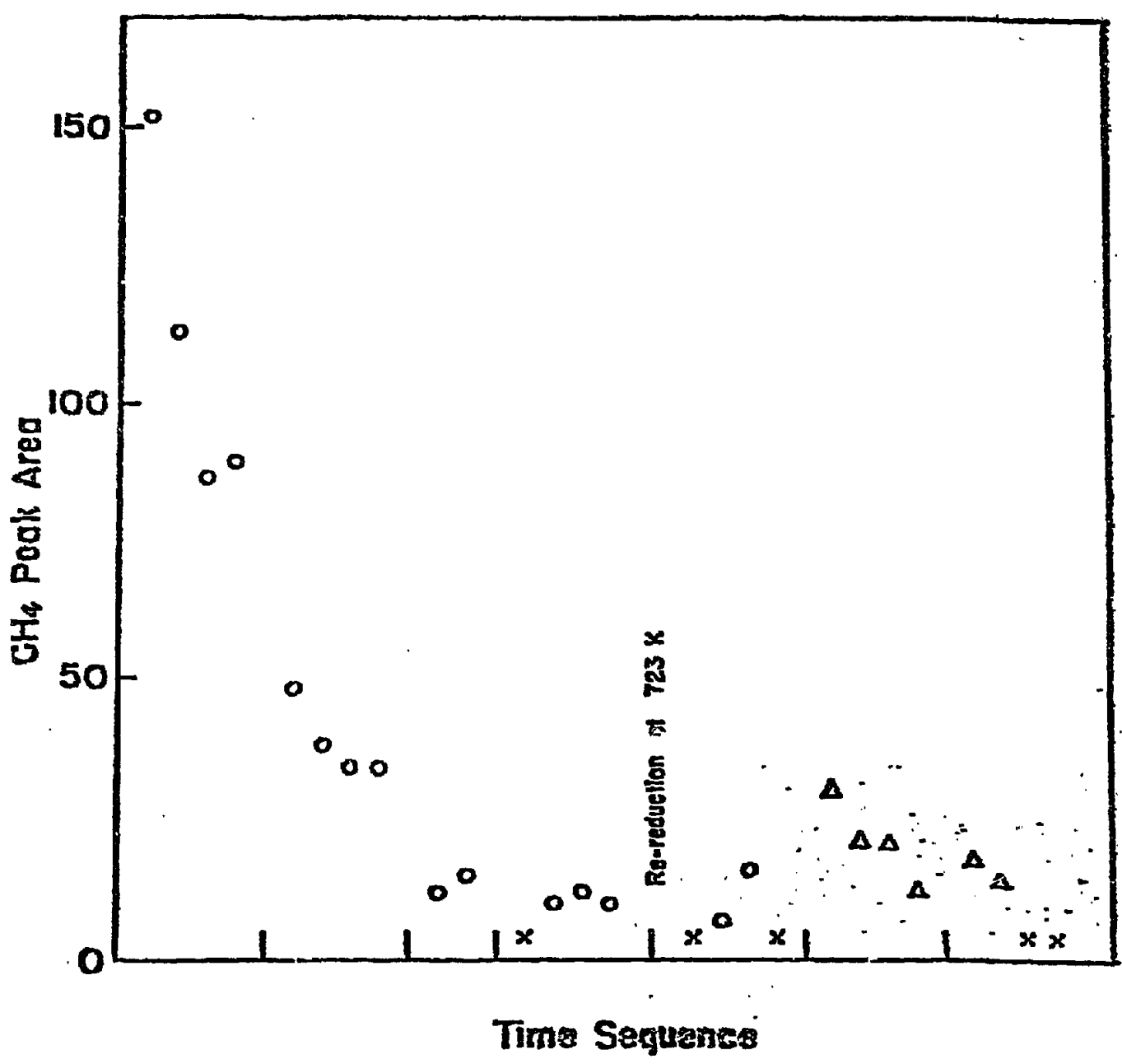


Fig. 1

Fig. 2  
84



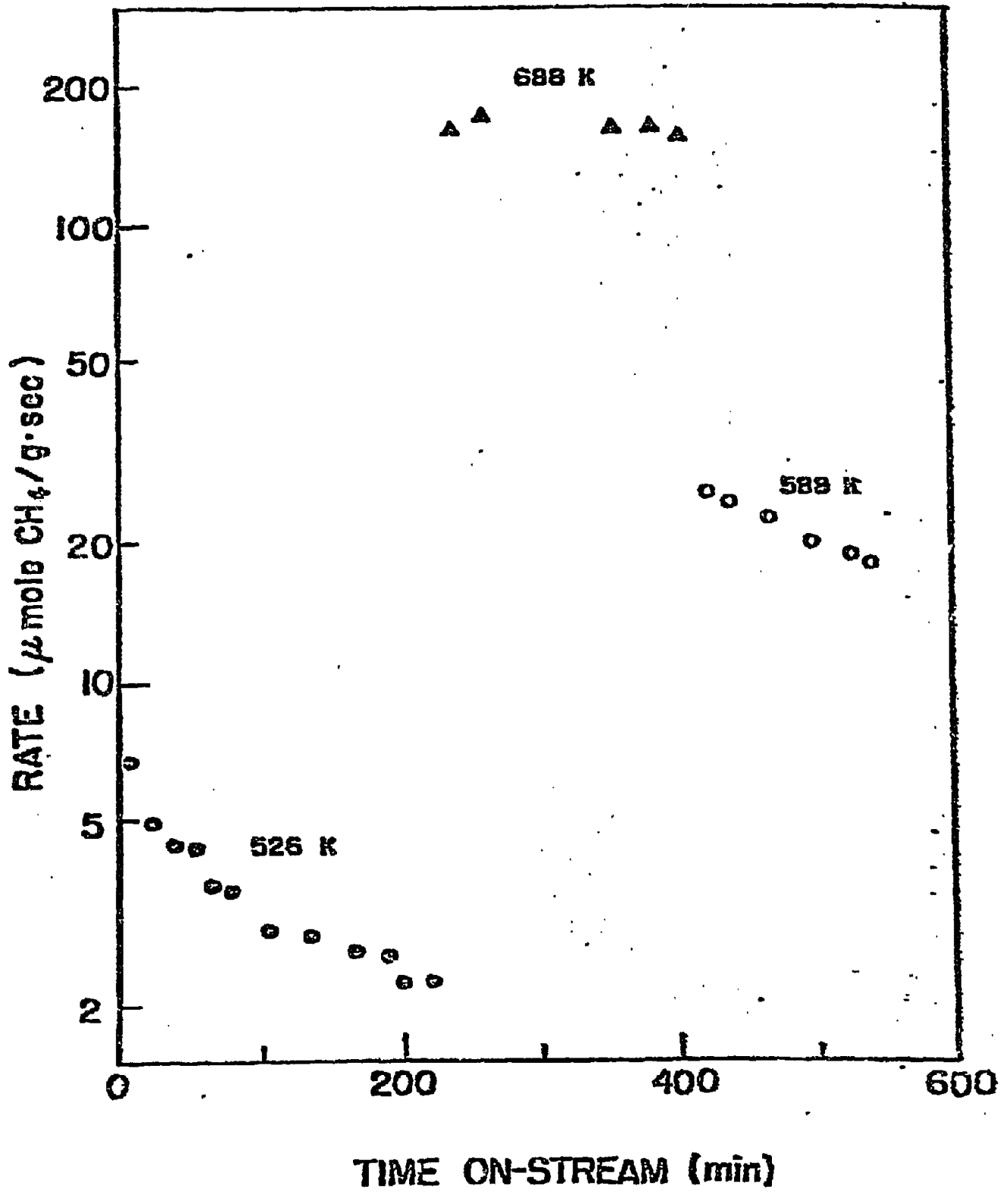
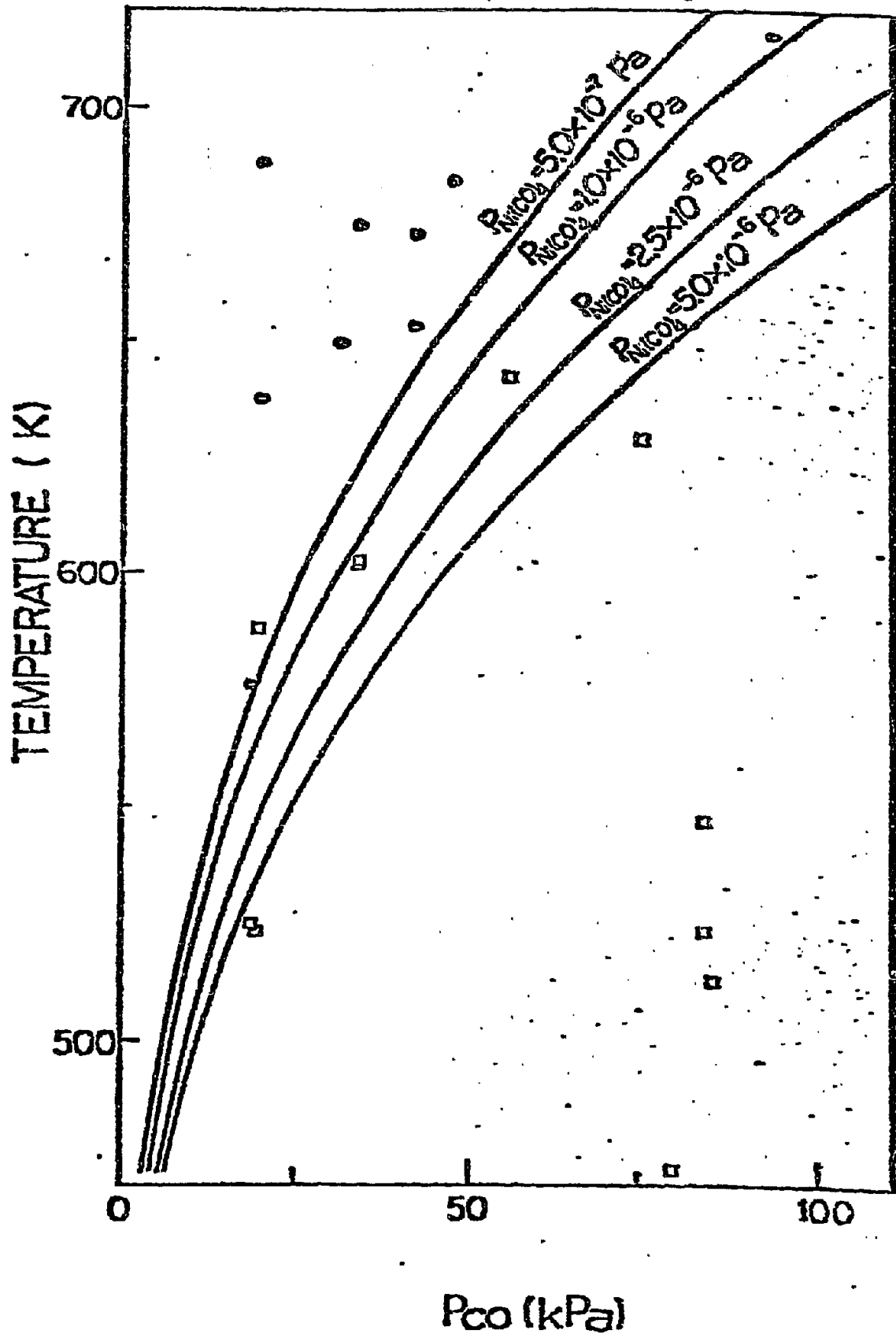


Fig. 4



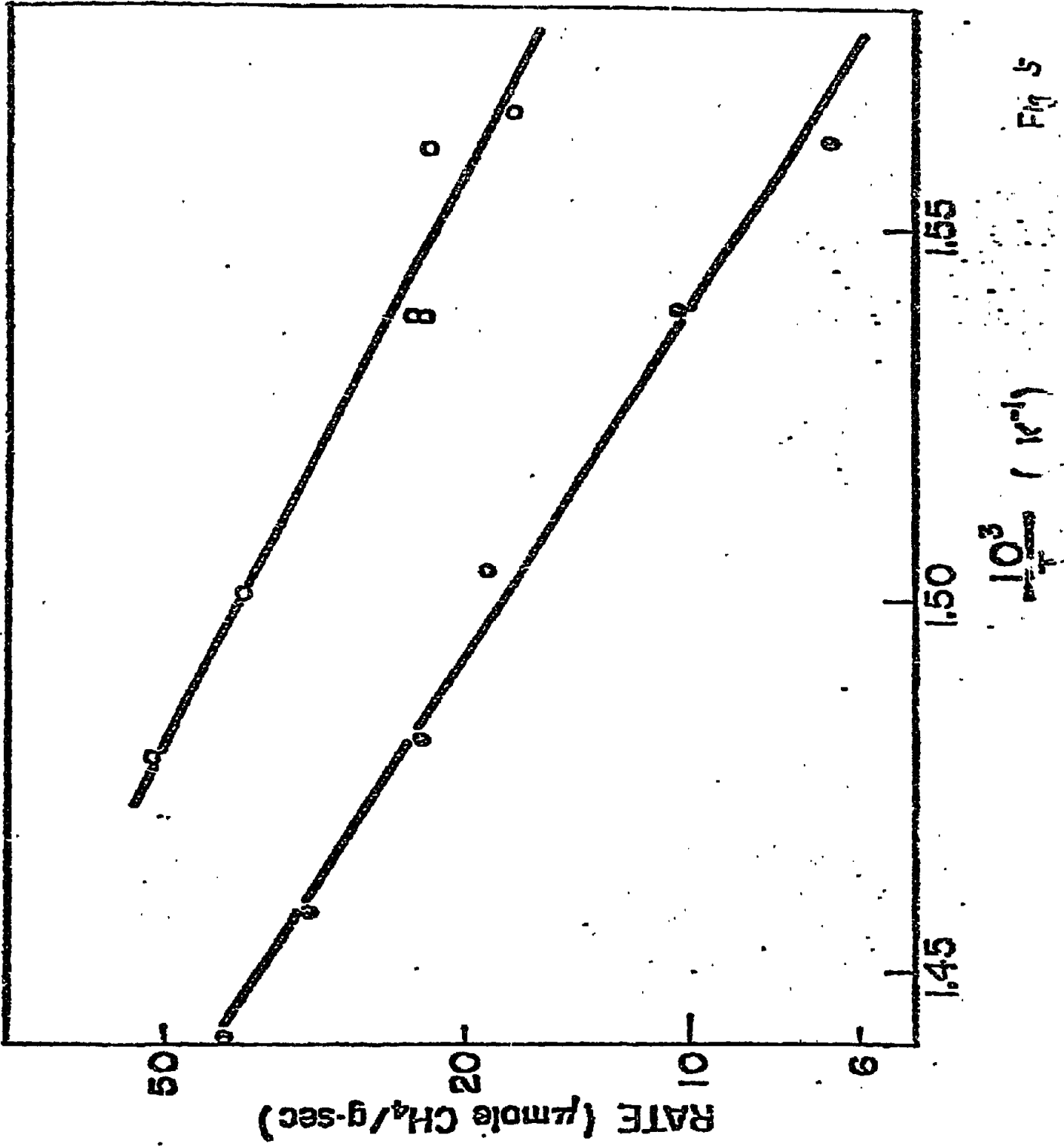


Fig 5



p

IV. Appendix B.\*

Iron Pentacarbonyl Decomposition over Grafoil:  
I. Production of Small Metallic Iron Particles<sup>‡</sup>

\* Revised from Annual Progress Report, October 1979; and  
published in the Journal of Physical Chemistry  
84, 1814 (1980).

<sup>‡</sup>References 1-27 provide an introduction to the  
properties of small, metallic particles and  
the decomposition of metal carbonyls.

#### IV.A. EXPERIMENTAL

88

##### IV.A.1. Iron Pentacarbonyl Handling

Iron pentacarbonyl, used as received from Apache Chemical Co., is a toxic, air and light sensitive material. Therefore for these experiments, a system was developed for handling the  $\text{Fe}(\text{CO})_5$  in a low light, air-free atmosphere (see Fig. 1). As preparation for introducing the  $\text{Fe}(\text{CO})_5$  to the Grafoil sample, the transfer bulb and the glass manifold were first evacuated to a pressure of ca. 1 Pa. Next, the evacuated section was opened to the bulb containing the liquid carbonyl, resulting in the rapid transport of carbonyl to the manifold and transfer bulb. At ambient temperatures the final vapor pressure is typically 3.3 kPa. The liquid-containing bulb and the transfer bulb were then isolated from the manifold and a pre-baked molecular sieve (13 X) trap was used to pump carbonyl vapor out of the system. This procedure prevents contamination of the mechanical-pump oil, and prevents subsequent deposition of iron on the walls of the manifold (which occurs readily upon contact of  $\text{Fe}(\text{CO})_5$  with oxygen). Finally the transfer bulb was mounted directly on the Mössbauer spectroscopy cell, and through appropriate valving the vapor in the bulb was allowed to enter the cell and adsorb on the treated Grafoil sample. The size of the transfer bulb (150 cm<sup>3</sup>) was chosen such that it contained the appropriate amount of  $\text{Fe}(\text{CO})_5$  vapor at room temperature to provide monolayer coverage of a 5 g Grafoil sample. This amount of iron is sufficient to give a Mössbauer spectrum in a reasonable time period (ca. 10 hours), but it is not great enough to cause detrimental "thickness line broadening" effects.<sup>28</sup>

#### IV.A.2. Mössbauer Spectroscopy

The Mössbauer spectroscopy cell (see Fig. 2) was modelled after an infrared cell described by Della Betta and Shelef.<sup>29</sup> The necessary windows for  $\gamma$ -ray transmission were made from 131 Teflon-coated Kapton (DuPont). Specifically, the Kapton (0.01 mm thick) was used for its excellent thermal stability (up to ca. 700 K), and the Teflon coating (0.004 mm thick on each side of the Kapton) was used to reduce the permeability of the polymer composite and to provide a leak-tight seal with the copper gaskets of standard conflat flanges. These windows were stable at all temperatures used in the present study (77-623 K), and they proved to be stable through dozens of vacuum cycles to pressures as low as  $6 \times 10^{-6}$  Pa.

Constant acceleration spectra were obtained with an Austin Science Associates, Inc. S-600 Mössbauer spectrometer equipped with an electromagnetic Doppler velocity motor. The source was 50 mCi of  $^{57}\text{Co}$  diffused into a palladium matrix, and it was obtained from New England Nuclear, Inc. The pulses from the proportional counter detector (Reuter Stokes) were amplified, shaped and gated using Austin Science Associates electronics. These shaped pulses were then sent to a Tracor Northern NS-900 multichannel analyzer. The MCA was interfaced directly to a PDP-11 mini-computer, greatly facilitating data storage and analysis. Doppler velocity was calibrated with a 1 mil Fe foil, and isomer shifts are reported relative to this standard absorber. Positive velocity corresponds to the source moving towards the absorber.

The spectra, collected using a triangular wave-form, were

the data to an assigned number of Lorentzian lines superimposed on a horizontal base line. The fitting procedure is "least squares" with a random stepping of free parameters. All sextuplets fitted in this study were constrained to be symmetric about the zero velocity channel (corrected for isomer shift).

#### IV.A.3. Graphite Sample

The sample was made from 38 circular discs (2.54 cm diameter) of GTA-grade "Grafoil" (Union Carbide). This material was made by pressing high purity, naturally occurring Madagascar graphite flakes into thin sheets.<sup>31</sup> Grafoil has two properties which proved useful for the present experiments and for several Mössbauer spectroscopy studies of molecular adsorption as well.<sup>32-35</sup> First, there is a high degree of alignment between the basal planes of the graphite microcrystals and the macroscopic Grafoil sheets. Neutron diffraction studies<sup>36</sup> have shown that the orientation distribution of the microcrystal basal planes is peaked parallel to the Grafoil sheet with a full width at half maximum of 30°. Secondly, the material has been measured<sup>37</sup> to have an average surface area of 22 m<sup>2</sup>/g, almost all of which is the highly uniform basal plane surface. The high surface area is required to make Mössbauer spectroscopy, in the transmission mode, a surface sensitive technique.

#### IV.B. RESULTS

A 7.9 g graphite sample was "activated" by treatment in oxygen at 970 K, resulting in a 8.5% reduction in sample weight. Following this oxidation, the sample was evacuated to ca. 10<sup>-3</sup> Pa for 10 h at 723 K and then cooled to room temperature under vacuum. The cell was subsequently sealed off from the pumps

and  $\text{Fe}(\text{CO})_5$  introduced from the transfer bulb.

91

Table 2 summarizes the pretreatments and Mössbauer spectroscopy run conditions for a series of experiments dealing with  $\text{Fe}(\text{CO})_5$  adsorption and decomposition on Grafoil. Spectrum 1 (Figure 3A) was taken by cooling the sample to 77 K in the presence of  $\text{Fe}(\text{CO})_5$ . The resulting quadrupole doublet is very similar to that of solid  $\text{Fe}(\text{CO})_5$ , as will be discussed later. The sample was then quickly heated (over a 5 minute period) to 378 K, maintained at this temperature for 55 minutes, and subsequently cooled to 77 K. The resulting six-peak spectral pattern (Figure 3B) indicates that the  $\text{Fe}(\text{CO})_5$  has been decomposed to metallic iron by the 378 K heat treatment. After collection of Spectrum 2, the sample was warmed to 295 K, and Spectrum 3 (Figure 3C) was then taken at this temperature. Finally, this series of experiments was concluded by heating the sample to 450 K for 10 h and collecting Spectrum 4 (Figure 3D) after cooling to 295 K. The iron, after this treatment, can again be qualitatively identified as being in the metallic state. It must be noted, however, that while the six-peak patterns of Spectra 2 and 3 indicate the presence of metallic iron, the isomer shifts, line widths and magnetic hyperfine fields are not those of massive metallic iron samples. This can be seen quantitatively in Table 2, where the results of computer analyses of Spectra 1-4 and a 1-mil Fe foil are summarized. Indeed, this difference is very significant, and will be addressed at length in the discussion section. The gas phase over the Grafoil surface, under conditions corresponding to Spectra 3 and 4, was sampled mass spectroscopically, and the results of these analyses are given in Table 3.

Transmission electron micrographs were made (Figure 4) of  $\text{Fe}(\text{CO})_5$  decomposed on single crystal Ticonderoga graphite,<sup>38</sup> cleaved in order to achieve the thinness required for transmission electron microscopy (TEM). The cleaved graphite flakes were cleaned at 1170 K for three hours in a vacuum of better than  $10^{-2}$  Pa. Following cooling to room temperature, the flakes were exposed to  $\text{Fe}(\text{CO})_5$  and decomposition was carried out for one hour at 378 K. The system was then pumped out and oxygen introduced very slowly in order to minimize oxidative heating of the iron particles.

It is assumed that the particles seen in Figure 4 are oxidized iron particles, and therefore do not necessarily represent the morphology of particles formed upon the initial decomposition of  $\text{Fe}(\text{CO})_5$ . However, it is also assumed that the particle location does not change during the oxidation process.

In the following section, the spectra are discussed and evaluated in more detail. In short, it will be shown that upon heating to 378 K,  $\text{Fe}(\text{CO})_5$  decomposes to form small metallic particles that interact with and "wet" the graphite surface. These particles in turn sinter and may become partially carbided following heating above 440 K.

#### IV.C. DISCUSSION

##### IV.C.1. $\text{Fe}(\text{CO})_5$ Adsorbed on Graphite-Spectrum 1

Figure 3A is the spectrum of  $\text{Fe}(\text{CO})_5$  adsorbed on graphite at 77 K. These two peaks were not observable at room temperature, suggesting that the  $\text{Fe}(\text{CO})_5$  is only physisorbed on the surface. In fact, the Mössbauer parameters obtained (quadrupole splitting = 2.51 mm/sec and isomer shift relative to iron =  $-0.06$  mm/sec) are similar to those given in the literature for solid  $\text{Fe}(\text{CO})_5$  (quadrupole splitting

= 2.57 mm/sec and isomer shift relative to iron = -.09 mm/sec).<sup>39</sup>

In the present study, however, the observed quadrupole splitting is slightly smaller than that reported in the literature.

Similar reductions in the quadrupole splitting of  $\text{Fe}(\text{CO})_8^{2-}$  and  $\text{Fe}(\text{CO})_4\text{H}$  have been interpreted to arise from the displacement of the equatorial CO groups out of the equatorial plane.

This results in a more nearly tetrahedral arrangement of four of the CO groups and hence a quadrupole splitting somewhere between the expected trigonal bipyramid value and the much smaller tetrahedral value.<sup>40</sup>

This suggests that there is a weak interaction between the  $\text{Fe}(\text{CO})_5$  and graphite, which leaves the  $\text{Fe}(\text{CO})_5$  structure altered only by a slight displacement of the equatorial CO groups. Also, the fact that the two peaks of the quadrupole doublet are of equal area suggests that there is no significant orientation of the  $\text{Fe}(\text{CO})_5$  molecules relative to each other on the graphite surface.<sup>41</sup> This is consistent with the statement that the  $\text{Fe}(\text{CO})_5$  is physisorbed on graphite.

#### IV.C.2. Interaction of Metallic Iron with Graphite - Spectra 2, 3 and 4

##### IV.C.2.a. Active Sites on Graphite

The spectra of Figures 3B,C,D are qualitatively those of metallic iron. Furthermore, it is reasonable to assume that this metallic iron is formed preferentially at edges or at other dislocations on the graphite surface. Experimental evidence for this statement is found in the transmission electron micrographs of Figure 4. In addition, however, there is evidence from other studies to support this claim.

For example, studies with carbon blacks, which like Grafoil are principally composed of the basal planes of carbon crystallites,<sup>42,43</sup> have shown that

p

94.

crystallite edges<sup>44</sup> and other imperfections.<sup>45</sup> Oxygen attacks these sites and must be removed before the carbon is "activated". For this reason, the Grafoil sample (see Table 1) was pretreated in a manner intended to maximize the total number of chemically active sites. First the graphite was subjected to a mild burning in order to increase the total crystallite edge area. Then the surface was outgassed at 725 K. Total oxygen desorption requires vacuum heating to 1273 K,<sup>46,47</sup> but it has been shown that a significant fraction of the surface oxygen can be removed as CO or CO<sub>2</sub> at temperatures as low as 500 K. Furthermore, heating at high temperatures, ca. 1000 K, has been shown to significantly reduce the reactivity of graphite,<sup>45,48,49</sup> possibly due to an annealing of basal plane dislocations initially introduced during mechanical processing. Hence, cleaning at 725 K represents a compromise (between removing all surface oxides and annealing out surface defects) likely to yield a chemically active graphite surface.

Studies of the kinetics of oxygen chemisorption on graphite<sup>50</sup> show that following cleaning, the re-adsorption of oxygen is a function of the temperature, pressure and nature of the surface sites. These studies suggest that although the most strongly adsorbing sites are covered (at 10 Pa of oxygen and 300 K) in seconds, the majority of sites, which are less active stay uncovered for variable lengths of time extending to several hours. Since the Fe(CO)<sub>5</sub> was admitted to the cell only a few minutes after in situ graphite cleaning, it is concluded that the Grafoil surface retains a large fraction of its active sites prior to carbonyl admission. Furthermore, independent experiments with the cell used in this study suggest that oxygen leaks over



the duration of the experiment were minimal. That is,  $\text{Fe}(\text{CO})_5$  did not oxidize to a detectable extent after more than five days in the cell, whereas deliberate introduction of oxygen into the cell immediately led to the room temperature oxidation of all the  $\text{Fe}(\text{CO})_5$  in the cell.

#### IV.C.2.b. Orientation of Iron Particles on Graphite

The relative areas of the six hyperfine-split peaks in Figures 3A,B,C indicate that the metallic iron particles are oriented on the Grafoil surface. Specifically, the relative peak areas in a hyperfine-split spectrum are a function of the average angle between the radiation of the source and the magnetic field at the iron in the sample. In a randomly oriented sample, the relative intensities of the spectral peaks is 3:2:1:1:2:3. For complete alignment of the magnetic fields perpendicular to the  $\gamma$ -ray direction the ratio is 3:4:1:1:4:3, while for alignment of the magnetic fields parallel to the  $\gamma$ -ray direction the ratio is 3:0:1:1:0:3. The relative peak areas of the observed spectra (see Table 2) are, thus, qualitatively indicative that the metallic iron magnetization is oriented approximately parallel to the Grafoil sheets. This would be consistent with the close proximity of neighboring iron particles along steps and edges of the graphite surface (as discussed above), with the corresponding "interaction anisotropy" responsible for aligning the iron magnetization parallel to the Grafoil sheets. Alternatively, this could be explained by a "spreading" of the iron particles over the graphite surface, with the corresponding magnetic shape anisotropy responsible for aligning the iron magnetization parallel to the Grafoil sheets. Evidence that the iron particles

do, in fact, "wet" the graphite surface will be presented later in this discussion.

#### IV.C.2.c. Particle Sintering and Possible Carbide Formation

The isomer shift provides additional evidence that the iron is interacting with carbon. The positive isomer shift (with respect to bulk metallic iron) of the iron after the heat treatment at 378 K indicates that the electronic properties of the iron are significantly different from those of bulk metallic iron. The origin of this effect is probably the interaction between iron and carbon, leading to an increase in the ratio of electrons in the p- and d-orbitals to electrons in the s-orbitals of iron. Heating to 450 K then decreases the extent of electron transfer between carbon and iron since the isomer shift approaches the value characteristic of bulk metallic iron following this treatment. In addition, the magnetic hyperfine field increases to that value for bulk metallic iron (Spectrum 4, Figure 3D), and the total spectra area increases by ca. 15%. These spectral changes are all suggestive that the iron particles sinter during extended heating at 450 K.

Although Spectrum 4 is composed primarily of the six peaks of metallic iron, it is possible that there is a minor contribution being made by one or more secondary iron-containing phases. It proved very difficult to fit this, or these, secondary phases because of peak overlap and poor counting statistics. However, several attempted computer fits, each using widely differing starting parameters, yielded broad secondary (ca. 15% of the total spectral area) sextuplets with an average hyperfine field of about 245 kOe. This suggests the possible presence of some form, or forms, of iron carbide.

Table 4 shows the results of the mass spectroscopic experiments designed to probe the extent to which carbon deposition (and hence carbide formation) could occur under the conditions experienced by the sample in the Mössbauer spectroscopy cell. The presence of  $\text{CO}_2$  in the gas phase following the 450 K heat treatment, and not following the 378 K heat treatment, suggests that the disproportionation of CO (and the possible formation of iron carbides) could occur only during the high temperature treatment. The formation of carbides from the dissociation of CO on iron particles is already well documented in the literature.<sup>51,52</sup>

#### IV.C.3. Quantitative Spectral Analysis - Spectra 2 and 3

##### IV.C.3.a. Relaxation Effects

Recent theoretical work suggests<sup>53,54</sup> that modes of collective magnetic excitation will result in a reduced hyperfine splitting for magnetic micro-crystals held below their blocking temperatures,  $T_B$  (where  $T_B$  is the temperature above which superparamagnetic relaxation becomes important). This phenomenon has been observed by several investigators<sup>53-55</sup> and has been used to determine approximate particle sizes using the formula:

$$\frac{\text{measured splitting}}{\text{bulk splitting}} = 1 - kT/2KV \quad (1)$$

where the measured and bulk hyperfine splittings are observed at temperature  $T$ ,  $k$  is Boltzmann's constant,  $V$  is the particle volume and  $K$  is the magnetic anisotropy energy constant. The magnetic anisotropy energy constant is a measure of the energy required to move the collective magnetic moment of a single domain spin system between various "easy directions".<sup>56</sup>

crystalline, shape anisotropy, surface anisotropy) make it difficult to precisely predict the value of  $K$  for a given system. However, a typical range of  $K$  for metallic iron is from approximately  $10^4$  erg/cm<sup>3</sup> (magnetocrystalline anisotropy) to  $10^7$  erg/cm<sup>3</sup> (shape or surface anisotropy).<sup>56</sup> With these values the average metallic iron particle volume can be computed using the above formula for the observed reduction in average magnetic hyperfine field. The results of this calculation are summarized in Table 4.

It should be noted, however, that the larger widths of the outer lines in Figures 3B and C is an indication that there is a distribution of hyperfine fields,<sup>57</sup> which in the model of collective magnetic excitations would be attributed to a distribution of particle sizes. (A distribution of quadrupole splittings would result in a uniform broadening of all six lines.) Hence, the values listed in Table 4 refer only to the mean particle diameter. The close agreement between particle sizes calculated from the spectra collected at two temperatures demonstrates that magnetic relaxation phenomena can explain the reduced hyperfine field data consistently.

A more rigorous test whether the observed reduced magnetic fields and broad spectral peaks can be interpreted in terms of magnetic relaxation is made through computer simulations of Mössbauer spectra. Following Mørup, Topsøe and Lipka,<sup>54</sup> spectra were generated taking into account (i) the combined effects of collective magnetic excitations, which result in a reduction in the observed hyperfine field and (ii) superparamagnetic relaxation, which results in the collapse of the six-

peak pattern. For each particle size of the particle size distribution, the associated anisotropy energy barrier was calculated (for a given anisotropy energy constant) and used to determine both the reduction in hyperfine splitting (see Equation (1)) and the superparamagnetic relaxation time  $\tau$ .<sup>58,59</sup> These values were then used to generate a Mössbauer spectrum for each particle size using the analytical expressions for line shape given by Wickman.<sup>60</sup> Then, by summing the Mössbauer spectra for the different particle sizes of an assumed particle size distribution, a global Mössbauer spectrum was computed and compared with those spectra obtained experimentally.

Several examples of simulated (room temperature) spectra are presented in Figure 5. In each case the spectrum is accompanied by a plot of the particle size distribution. The anisotropy energy constant was varied over the complete range of physically reasonable values (from ca.  $10^5 - 10^7$  erg/cm<sup>3</sup>); and all meaningful particle size distributions for a given value of  $K$  were also tried, as discussed below. The Mössbauer parameters of iron were chosen such that as the particle size increased the peak positions and relative peak intensities approached those of bulk metallic iron (at 300 K) with its magnetization perpendicular to the  $\gamma$ -ray direction. It was deduced from these simulations that for any given anisotropy barrier, only a very small range of particle radii existed with particles (i) sufficiently large that a superparamagnetic central peak not be present and (ii) sufficiently small that the reduced magnetic hyperfine fields be observed.

In no case could spectra be generated which had all of the qualitative features of the spectra obtained experimentally. For example, in the experimental spectrum at room temperature (Figure 3.C) the absorbance of the innermost peaks (lines 3 and 4) and outermost peaks (lines 1 and 6) are very nearly the same due to the large relative broadening of the outer peaks. Thus, although magnetic relaxation effects can indeed quantitatively explain the reduced magnetic hyperfine fields and their temperature dependence, these effects cannot quantitatively explain the significant relative broadening of the outer lines. The origin of this relative broadening must be the presence of a hyperfine field distribution in addition to that produced by magnetic relaxation and the particle size distribution.

#### IV.C.3.b. Hyperfine Field Distribution Effects

The surface layers of iron crystals and films have been shown to have magnetic hyperfine fields significantly different from those of the bulk as reviewed recently by Toppé et al.<sup>61</sup> In some cases, these differences may be simply due to the loss of three-dimensional translational symmetry at the surface. While several theoretical (and experimental)<sup>62</sup> studies suggest that this effect should lead to a reduced hyperfine field at the surface,<sup>63,64</sup> other studies note that the surface may show an enhanced hyperfine field.<sup>65</sup> Some calculations also point to the presence of a hyperfine field distribution near the surface, the breadth of which increases as the Curie temperature is approached.<sup>66</sup> In addition to these effects of translational symmetry, large deviations from bulk magnetic properties have been attributed to the nature of the chemical bonding at the

surface. For example, the adsorption of gases has been shown to affect the surface magnetic properties.<sup>67,68</sup> The case of CO adsorbed on iron is of particular interest in the present discussion, and it has been reported that the chemisorption of this molecule increases the surface hyperfine field of iron by ca. 5-10 kOe. The chemical effects at an iron/solid interface have been shown to be even larger. Specifically, the average hyperfine field for an iron/solid interface has been found to be a strong function of the solid material with which the iron surface is in contact (see Table 5). It can be seen from this table that the average hyperfine field may be either larger or smaller than that in the bulk, depending on the nature of the chemical interaction between the two solids. Furthermore, many investigators report the existence of a distribution of hyperfine fields near the surface. In addition, it should be noted that the presence of demagnetizing fields for single domain particles may also be expected to alter the average hyperfine field, giving rise to an increase of up to 20 kOe for metallic iron.<sup>75</sup>

For the case of the iron/carbon system, there is considerable evidence in the literature that the presence of carbon in the atomic vicinity of iron can both increase and decrease the magnetic hyperfine field.<sup>76-78</sup> In particular, an iron atom having carbon atoms as nearest

neighbors will possess a reduced magnetic hyperfine field due to local electron interactions between the d-orbitals of iron and the s- and p-orbitals of carbon.<sup>79</sup> It has generally been found that non-magnetic atoms in a magnetic lattice will reduce the field locally.<sup>80,81</sup> In addition, an iron atom having carbon atoms as second, third and further next-nearest neighbors will possess an increased magnetic hyperfine field due to lattice strain effects.<sup>76</sup> The effect of these next-nearest neighbors decreases geometrically with increasing distance between iron and carbon, approaching zero asymptotically.

It has been shown that the effects of carbon are not limited to carbon dissolved in a lattice. Carbon-metal interfaces also have changed magnetic behavior. Gradmann et al.<sup>82</sup> suggested that a reduction in the magnetic moment of carbon covered 60 Ni/40 Fe oligatomic films could be caused by the filling of metal "d-holes" in the interface layer by the covering carbon atoms.

The results of Table 5 suggest that the effects of carbon on the magnetic hyperfine field of iron, in fact, are restricted to the Fe/graphite interface in contrast to the presence of carbon "dissolved" in the iron. That is, the mass spectroscopic analysis of the gas phase over the iron following  $\text{Fe}(\text{CO})_5$  decomposition at 378 K gives no evidence for the presence of  $\text{CO}_2$ . This observation indicates that dissolved carbon could not have been produced at this temperature via the Boudouard reaction (the disproportionation



of CO to give C and CO<sub>2</sub>). Furthermore, graphite is thermodynamically stable (at these temperatures) with respect to the formation of iron carbides or significant amounts of carbon dissolved in iron.

While it is not possible to predict the magnetic hyperfine field distribution resulting from the iron/graphite and iron/gas interfaces, it is clear from the above discussion that a magnetic hyperfine field distribution should, in fact, exist. Thus, computer simulations were carried out by adding an independent magnetic hyperfine field distribution to the effects of magnetic relaxation discussed in the previous discussion section. The results of one such simulation are shown in Figure 6. This combination reproduced the reduced magnetic hyperfine fields (magnetic relaxation), the broad background dip centered at zero velocity (magnetic relaxation) and the relative broadening of the outer peaks (hyperfine field distribution). It is thus suggested that the presence of a magnetic hyperfine field distribution (due to the iron/graphite and iron/gas interfaces) and magnetic relaxation effects are responsible for the general features of Spectra 2 and 3. It is not suggested, however, that the values for the adjustable parameters of this simulation necessarily have quantitative validity.

#### IV.C.4. Proposed Iron Morphology

The computer simulations performed in this investigation show that any model of the particle morphology (prior to the 450 K heat treatment) must explain the existence of both magnetic relaxation and a distribution of hyperfine fields.

The relaxation phenomena are unambiguously attributed to a finite particle volume. However, the distribution of hyperfine fields may arise from the presence of the Fe/graphite and/or Fe/gas interfaces. The experiments conducted in this study were not sufficient to distinguish these two interfacial effects. Fortunately, both of these interfacial effects lead to the same morphological model. That is, to fully explain the distribution of hyperfine fields, the particles must have a high surface to volume ratio. Hence, the metal particles are modelled to be "raft-like" structures of the order 1 nm thick and several tens of nm in lateral dimension. The choice of the order of 1 nm for the raft thickness explains the observed importance of interfacial effects (hyperfine field distribution). The large lateral dimension is chosen for consistency with the particle volumes estimated from the magnetic relaxation effects (reduced hyperfine field, see Table 4).

Finally, it is postulated that the particles are preferentially located at dislocations, steps and other imperfections on the Grafoil surface. There are two types of evidence which support this suggestion: (i) a general understanding of the behavior and location of "active sites" on a graphite surface, and (ii) transmission electron micrographs of iron particles decorating steps and edges of single-crystal graphite surfaces. During heating to 450 K, both the Mössbauer spectra and mass spectroscopic gas phase analyses suggest that CO may disproportionate on the metallic iron surface, creating partially carbided particles and CO<sub>2</sub>. The metallic iron particles also sinter, resulting in a spectral component with parameters close to those of bulk metallic iron.

## IV.D. REFERENCES

- (1) E. B. Prestrige, G. H. Via, and J. H. Siefert, *J. Catal.*, 50, 115 (1977).
- (2) M. A. Vannice and R. L. Garten, *J. Catal.*, 56, 236 (1979).
- (3) J. R. Katzer, G. C. A. Schuit, and J. H. C. Van Hooff, *J. Catal.*, 59, 278 (1978).
- (4) R. Van Hardeveld and F. Hartog, *Surf. Sci.*, 15, 189 (1969).
- (5) J. A. Dumesic, H. Topsøe, S. Khammouma, and M. Boudart, *J. Catal.*, 37, 503 (1975).
- (6) R. P. Messmer and K. R. Johnson, NBS Special Publ. 455, 1976, p. 67.
- (7) R. C. Baetzold, *Adv. Catal.*, 25, 1 (1976).
- (8) N. D. Parkyns, "Proceedings of the Third International Congress on Catalysis", W. H. M. Sachtler, G. C. A. Schuit, and P. Zwietering, Eds., North-Holland, Amsterdam, 1965, p. 914.
- (9) R. F. Howe, D. E. Davidson, and D. A. Whan, *J. Chem. Soc., Faraday Trans. 1*, 68, 2266 (1972).
- (10) R. F. Howe and J. R. Leath, *J. Chem. Soc., Faraday Trans. 1*, 69, 1967 (1973).
- (11) E. G. Derouane, J. B. Nagy, and J. C. Vedrine, *J. Catal.*, 46, 434 (1977).
- (12) J. Smith, R. F. Howe, and D. A. Whan, *J. Catal.*, 34, 191 (1974).
- (13) J. R. Anderson and D. E. Mainwaring, *J. Catal.*, 35, 162 (1974).
- (14) J. R. Anderson and R. F. Howe, *Nature*, 268, 129 (1977).
- (15) J. R. Anderson, P. S. Elmes, R. F. Howe, and D. E. Mainwaring, *J. Catal.*, 50, 508 (1977).
- (16) P. Gallezot, G. Coudurier, M. Primet, and B. Imelik, "Molecular Sieves II", ACS Symposium Series, No. 40, J. Katzer, Ed., p. 144.
- (17) J. Robertson and G. Webb, *Proc. R. Soc. London, Ser. A*, 341, 383 (1974).
- (18) G. C. Smith, T. P. Chojnacki, S. R. Dasgupta, K. Iwatate, and K. L. Watters, *Inorg. Chem.*, 14, 1419 (1975).
- (19) J. B. Nagy, M. Van Eenoo, and E. G. Derouane, *J. Catal.*, 58, 230 (1979).

- (20) B. H. Bartholmew and M. Boudart, *J. Catal.*, 25, 173 (1972).
- (21) J. Bette, K. Kinoshita, K. Roulsis, and P. Stonehart, *J. Catal.*, 29, 160 (1973).
- (22) D. Pope, W. L. Smith, M. J. Eastlake, and R. L. Moss, *J. Catal.*, 22, 72 (1971).
- (23) C. E. Hunt, *J. Catal.*, 23, 93 (1971).
- (24) K. Aika, H. Hori, and A. Ozaki, *J. Catal.*, 27, 424 (1972).
- (25) P. Ehrburger, O. P. Mahajan, and P. L. Walker, Jr., *J. Catal.*, 43, 61 (1976).
- (26) P. Ehrburger and P. L. Walker, *J. Catal.*, 55, 63 (1978).
- (27) E. Ruckenstein and P. S. Lee, *Surf. Sci.*, 52, 298 (1975).
- (28) J. A. Dumesic and H. Topsøe, *Adv. Catal.*, 26, 121 (1977).
- (29) R. A. Dalla Betta and M. Shelef, *J. Catal.*, 48, 111 (1977).
- (30) K. Sørensen, Laboratory of Applied Physics II, Technical University of Denmark, Lyngby, Denmark, Internal Report No. 1 (1972).
- (31) M. Bretz, J. G. Dash, D. C. Hickernell, E. O. Mclean and O. E. Vilches, *Phys. Rev. A*, 8, 1589 (1973).
- (32) S. Bukshpan, *Phys. Lett. A*, 62, 109 (1977).
- (33) H. Shecter, J. G. Dash, M. Mor, R. Ingalls, and S. Bukshpan, *Phys. Rev. B*, 14, 1876 (1976).
- (34) S. Bukshpan, T. Sonnino, and J. G. Dash, *Surf. Sci.*, 52, 466 (1975).
- (35) J. K. Kjems, L. Passell, H. Taub, and J. G. Dash, *Phys. Rev. Lett.*, 32, 724 (1974).
- (36) J. K. Kjems, L. Passell, H. Taub, J. G. Dash, and A. D. Novao, *Phys. Rev. B*, 13, 1446 (1976).
- (37) R. L. Elgin and D. L. Goodstein, *Phys. Rev. A*, 9, 265 (1974).
- (38) R. T. F. Baker, J. A. France, L. Rouse, and R. J. Waite, *J. Catal.*, 41, 22 (1976).
- (39) K. Farmery, M. Kilner, R. Greatrex, and N. N. Greenwood, *J. Chem. Soc. A*, 2339 (1969).
- (40) R. H. Herber, W. R. Kingston, and G. K. Wertheim, *Inorg. Chem.*, 2, 153 (1963).
- (41) R. Greatrex and N. N. Greenwood, *Disc. Faraday Soc.*, No. 47, 126 (1969).

- (42) H. Akamatu and H. Kuroda, "Proceedings of the Fourth Conference on Carbon", Pergamon Press, New York, N.Y., 1960, p. 355.
- (43) E. A. Kmetko, "Proceedings of the First and Second Conferences on Carbon", University of Buffalo, Buffalo, N.Y., 1956, p. 21.
- (44) G. R. Hennig, "Proceedings of the Fifth Conference on Carbon", Vol. 1, Pergamon Press, New York, N.Y., 1962, p. 143.
- (45) H. H. Harker, J. B. Horsley, and D. Robson, Carbon, 9, 1 (1977).
- (46) N. R. Laine, F. J. Vastola, and P. L. Walker, Jr., J. Phys. Chem., 67, 2030 (1963).
- (47) S. S. Barton and B. H. Harrison, Carbon, 10, 245 (1972).
- (48) S. Mrozowski and J. F. Andrew, "Proceedings of the Fourth Conference on Carbon", Pergamon, New York, N.Y., 1960, p. 207.
- (49) S. Barton, B. H. Harrison, and J. Dollimore, J. Phys. Chem., 82, 290 (1978).
- (50) R. C. Bansal, F. J. Vastola, and P. L. Walker, Jr., J. Colloid Interface Sci., 32, 187 (1970).
- (51) J. A. Amelse, J. B. Butt, and L. H. Schwartz, J. Phys. Chem., 82, 558 (1978).
- (52) G. B. Raupp and W. N. Delgass, J. Catal., 58, 348 (1979).
- (53) S. Mørup and H. Topsøe, Appl. Phys., 11, 63 (1976).
- (54) S. Mørup, H. Topsøe, and J. Lipka, J. Phys. (Paris), Colloq., 37, C6-287 (1976).
- (55) G. B. Raupp and W. N. Delgass, J. Catal., 58, 337 (1979).
- (56) S. Mørup, J. A. Dumesic, and H. Topsøe, "Applications of Mössbauer Spectroscopy", Vol. 2, R. L. Cohen, Ed., Academic Press, in press.
- (57) T. Shinjo, T. Matsuzawa, T. Takada, S. Nasu, and Y. Murakami, J. Phys. Soc. Jpn., 35, 1032 (1973).
- (58) W. F. Brown, Phys. Rev., 130, 1677 (1963).
- (59) A. Aharoni, Phys. Rev. A, 135, 447 (1964).
- (60) R. H. Wickman, "Mössbauer Effect Methodology", Vol. 2, I. J. Gruverman, Ed., Plenum, New York, N.Y., 1966, p. 39.
- (61) H. Topsøe, J. A. Dumesic, and S. Mørup, "Applications of Mössbauer Spectroscopy", Vol. 2, R. L. Cohen, Ed., Academic Press, in press.

- (62) T. Shinjo, *IEEE Trans. Magn.*, 12, 86 (1976).
- (63) K. Levin, A. Liebsch, and K. H. Bennenann, *Phys. Rev. B*, 7, 3066 (1973).
- (64) P. Fulde, A. Luther, and R. E. Watson, *Phys. Rev. B*, 8, 440 (1973).
- (65) A. J. Freeman, "Proceedings of the International Conference on the Mössbauer Effect", Yugoslavia, 1979, in press.
- (66) K. Binder and P. C. Hohenburg, *Phys. Rev. B*, 9, 2194 (1974).
- (67) P. W. Selwood, "Chemisorption and Magnetization", Academic Press, New York, N.Y., 1975.
- (68) S. Mørup, B. S. Clausen, and H. Topsøe, *J. Phys. (Paris), Colloq.*, 40, C2-78 (1979).
- (69) J. Lauer, W. Keune, and T. Shinjo, *Physica*, 86-88B, 1409 (1977).
- (70) T. Shinjo, S. Hibe, and T. Takada, "Proceedings of the Seventh International Vacuum Congress and Third International Conference on Solid Surfaces", Vienna, 1977, p. 2655.
- (71) T. Shinjo, S. Hibe, and T. Takada, *J. Phys. (Paris), Colloq.*, 40, C2-86 (1979).
- (72) L. E. Violet and E. L. Lee, "Mössbauer Effect Methodology", Vol. 2, I. J. Gruverman, Ed., Plenum, New York, N.Y., 1966, p. 171.
- (73) W. Keune, J. Lauer, U. Gonser, and D. L. Williamson, *J. Phys. (Paris), Colloq.*, 40, C2-69 (1979).
- (74) S. Duncan, A. H. Owens, R. J. Semper, and J. C. Walker, *Hyperfine Int.*, 4, 886 (1978).
- (75) S. Mørup, B. S. Clausen, and H. Topsøe, "Proceedings of the International Conference on the Mössbauer Effect", Yugoslavia, 1979, in press.
- (76) T. Moriya, H. Ino, and F. E. Fujita, *J. Phys. Soc., Jpn.*, 24, 60 (1968).
- (77) H. Ino, T. Moriya, F. E. Fujita, Y. Maeda, Y. Ono, and Y. Inokuti, *J. Phys. Soc., Jpn.*, 25, 88 (1968).
- (78) H. Ino, T. Moriya, F. E. Fujita, and Y. Maeda, *J. Phys. Soc., Jpn.*, 22, 346 (1967).
- (79) H. Bernas, I. A. Campbell, and R. Fruchart, *J. Phys. Chem. Solids*, 28, 17 (1967).
- (80) G. K. Wertheim, V. Jaccarino, J. H. Wernick, and D. N. E. Buchanan, *Phys. Rev. Lett.*, 12, 24 (1964).

- (81) C. E. Johnson, M. S. Ridout, and T. E. Cranshaw, Proc. Phys. Soc., 81, 1079 (1963).
- (82) U. Gradmann and K. Salewski, Physica, 86-88B, 1399 (1977).

List of Tables

- Table 1: Sample Preparation
- Table 2: Computer Fit Parameters for Mössbauer Spectra of Iron Particles Formed from the Decomposition of Iron Pentacarbonyl on Grafoil
- Table 3: Mass Spectral Analyses of Gas Phase over Grafoil after  $\text{Fe}(\text{CO})_5$  Decomposition
- Table 4: Relaxation Model Computations
- Table 5: Results from Mössbauer Studies of the Magnetic Properties of Thin Iron Films



TABLE I - SAMPLE PREPARATION

Sample	% Burn-off	Approx. mass (g)	CLEANING		
			Temp.	Time	Pressure
Mössbauer	8.5	7.9	723 K	10 hrs.	$10^{-2}$ Pa
TEM	0	-	1273 K	2 hrs.	$10^{-3}$ Pa

TABLE 2 - COMPUTER FIT PARAMETERS FOR MOSSBAUER SPECTRA OF IRON PARTICLES FORMED FROM THE DECOMPOSITION OF IRON PENTACARBONYL ON GRAFOIL

SPECTRUM	TREATMENT TEMP. (K)	SPECTRUM TEMP. (K)	SPECTRAL PEAK AREA RATIO (1+G)/(2+G)	HYPERFINE FIELD (kOe)	ISOMER SHIFT (mm/sec) (Relative to Fe)	LINE WIDTHS (mm/sec)
SPECTRUM 2 (FIGURE 3B)	378	77	1.02/1	329	0.14	1.5/1.2/0.7
SPECTRUM 3 (FIGURE 3C)	378	295	1.04/1	299	0.06	1.7/1.2/0.7
SPECTRUM 4* (FIGURE 3D)	450	295	1.04/1 (1.5/1)	331 (245)	0.003 (0.2)	0.35/0.35/0.5
1 mil Fe foil	-	295	2.9/2	330	0	0.28/0.25/0.23

\* Spectrum 4 is composed of two components. The major component is metallic iron. The secondary component(s) (in parenthesis) representing less than 15% of the total spectral area, proved difficult to computer fit. Hence the figures in parenthesis are very approximate values.

TABLE 3 - MASS SPECTRAL ANALYSES OF GAS PHASE OVER  
GRAFOIL AFTER  $\text{Fe}(\text{CO})_5$  DECOMPOSITION

Sample	Weight	CLEANING		DECOMPOSITION		CO/CO <sub>2</sub> Ratio
		Temp. (K)	Time	Temp. (K)	Time	
1	1.67	723	10 hrs.	383	2 hrs.	>1000/1
2	1.47	723	10 hrs.	450	10 hrs.	~70/1

TABLE 4 - RELAXATION MODEL COMPUTATIONS

Energy Anisotropy Constant, K	T (K)	Mean Particle Diameter (nm) (A)	Lateral Dimension (nm) (B)
$10^7$ ergs/cm <sup>3</sup>	295	4.3	12.9
	77	4.3	12.5
$10^5$ ergs/cm <sup>3</sup>	295	20	89.5
	77	19	82.8

(A) Calculations based on the assumption that the particles are hemispheres.

(B) Calculations based on the assumption that the particles are square "rafts" 1 nm thick.

TABLE 5 - RESULTS FROM MOSSBAUER STUDIES OF THE MAGNETIC PROPERTIES OF THIN IRON FILMS

<u>Film Morphology</u>	<u>Average hyperfine field</u>	<u>Approx. range of hyperfine fields</u>	<u>Temp. K</u>	<u>Ref.</u>
Vacuum - 1/10 monolayer $^{57}\text{Co}$ - $10^2$ layers Co	330	240-380	4.2	56
Vacuum - 1/10 monolayer $^{57}\text{Co}$ - $10^2$ layers natural Fe	290	210-370	4.2	62
100 nm Cu - 0.5 nm $^{57}\text{Fe}$ - 10 nm natural Fe	290	210-370	77	69
20 nm $\text{MgF}_2$ - 2.4 nm Fe - 20 nm $\text{MgF}_2$	(320)	(300-330)	300	70
20 nm $\text{MgF}_2$ - 2.4 nm Fe - 20 nm $\text{MgF}_2$	(370)	(320-390)	4.2	70
20 nm $\text{MgF}_2$ - 1.6 nm Fe - 20 nm $\text{MgF}_2$	(300)	(250-340)	300	70
20 nm $\text{MgF}_2$ - 1.6 nm Fe - 20 nm $\text{MgF}_2$	(375)	(320-390)	4.2	70
40 nm $\text{MgO}$ - 1.6 nm Fe - 40 nm $\text{MgO}$	(330)	(*)	300	71
40 nm $\text{MgO}$ - 0.8 nm Fe - 40 nm $\text{MgO}$	(380)	(350-400)	4.2	71
5 nm $\text{SiO}_2$ - 0.5 nm Fe - 5 nm $\text{SiO}_2$	(325)	(300-350)	77	72
5 nm $\text{SiO}_2$ - 1.5 nm Fe - 5 nm $\text{SiO}_2$	(330)	(310-350)	300	72
30 nm Cu - 0.5 nm Fe - 30 nm Cu	290	(260-330)	4.2	73
30 nm Ag - 0.5 nm Fe - 30 nm Ag	358	(*)	4.2	73
30 nm Ag - 2.0 nm Fe - 200 nm Ag	325	323-327	300	74
30 nm Ag - 2.0 nm Fe - 200 nm Ag	348	-	4.2	74

Numbers in parenthesis are approximations made on the basis of visual inspection of published spectra.

\* (very little broadening)

### List of Figures

- Figure 1: Carbonyl Handling System. A) To vacuum pump, B) Thermocouple pressure gauge, C) Liquid nitrogen trap, D) Molecular sieve trap, E) Bulb containing liquid  $\text{Fe}(\text{CO})_5$ , F) Carbonyl transfer bulb, G) Mercury manometer
- Figure 2: Mössbauer Sample Cell. A) Thermocouple feed-through, B) Ground glass joint for attaching carbonyl transfer bulb, C) Liquid nitrogen reservoir, D) Sample, E) Beaded heater, F) Conflat flange, G) Vacuum line, H) 131 Kapton windows squeezed between copper gaskets, I) Heater wires
- Figure 3: Mössbauer Spectroscopy Record of  $\text{Fe}(\text{CO})_5$  Decomposition on Grafoil. A)  $\text{Fe}(\text{CO})_5$  frozen on Grafoil at 77 K, B) Spectrum at 77 K following decomposition at 378 K, C) Spectrum at 295 K following decomposition at 378 K, D) Spectrum at 295 K following heat treatment at 450 K
- Figure 4: Transmission Electron Micrograph following decomposition of  $\text{Fe}(\text{CO})_5$  at 378 K on Cleaned, Single Crystal Graphite Specimens.
- Figure 5: Computer Simulations of Collective and Superparamagnetic Relaxation Effects on Mössbauer Spectra. In all three simulations pictured,  $K = 5 \times 10^5$  ergs/cm<sup>3</sup> and  $T = 300$  K. The only parameter varied in the three examples shown was the particle radius distribution (printed to the right of each spectrum). It was assumed for computation of the particle volumes (and hence relaxation time  $\tau$ ) that the particles were hemispherical.
- Figure 6: Computer Simulation of Combined Hyperfine Field Distribution and Relaxation Effects. A) Mössbauer spectrum at 300 K following decomposition of  $\text{Fe}(\text{CO})_5$  at 378 K (same as Figure 3C), B) Simulated Mössbauer spectrum, C) Assumed particle radius distribution (for hemispherical particles), D) Assumed hyperfine field distribution. In the simulation, It was assumed that  $K = 5 \times 10^5$  ergs/cm<sup>3</sup>,  $T = 300$  K, and the peak area ratio was equal to 3:3:1:1:3:3.

Figure 1

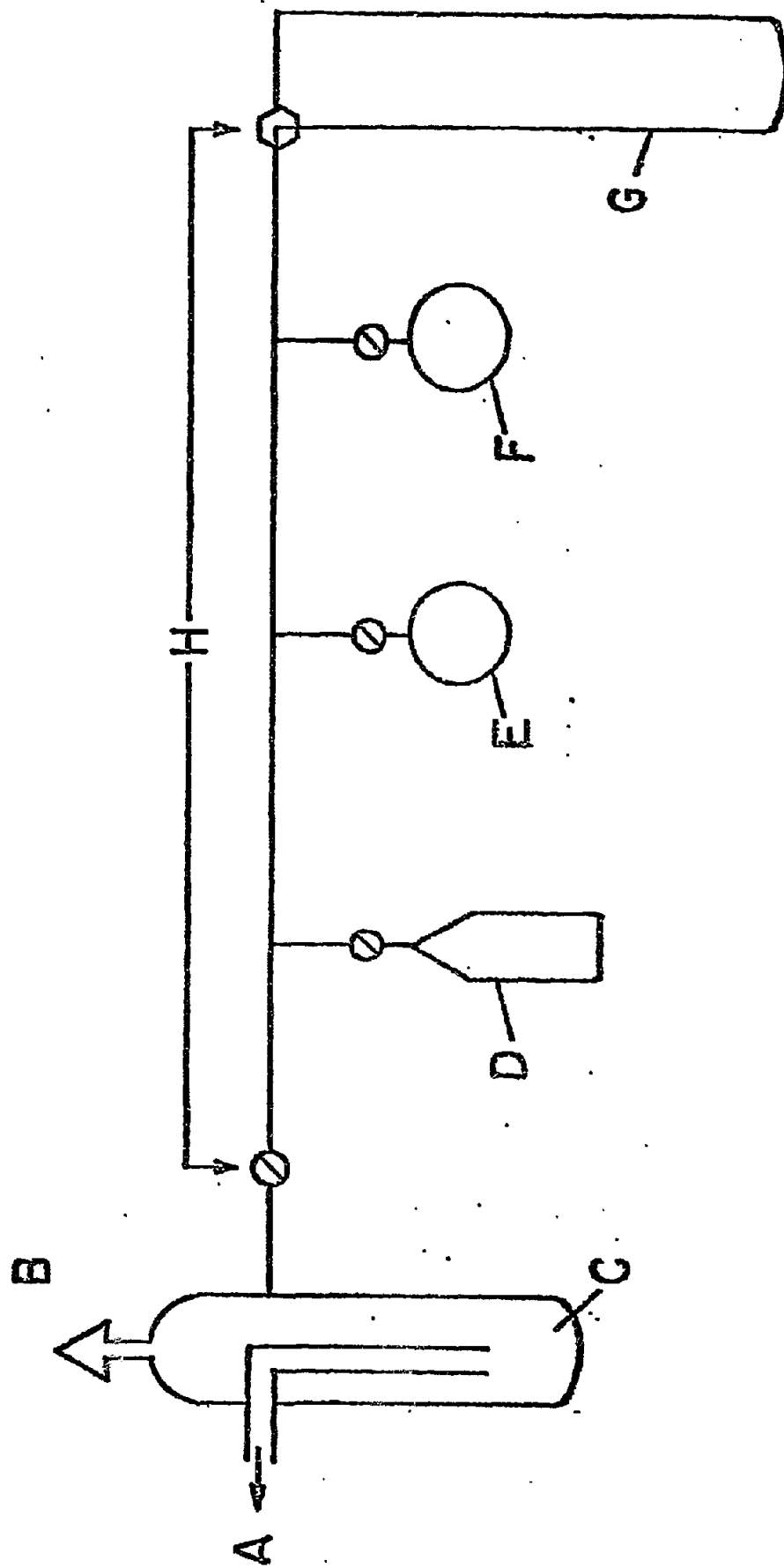


Figure 2

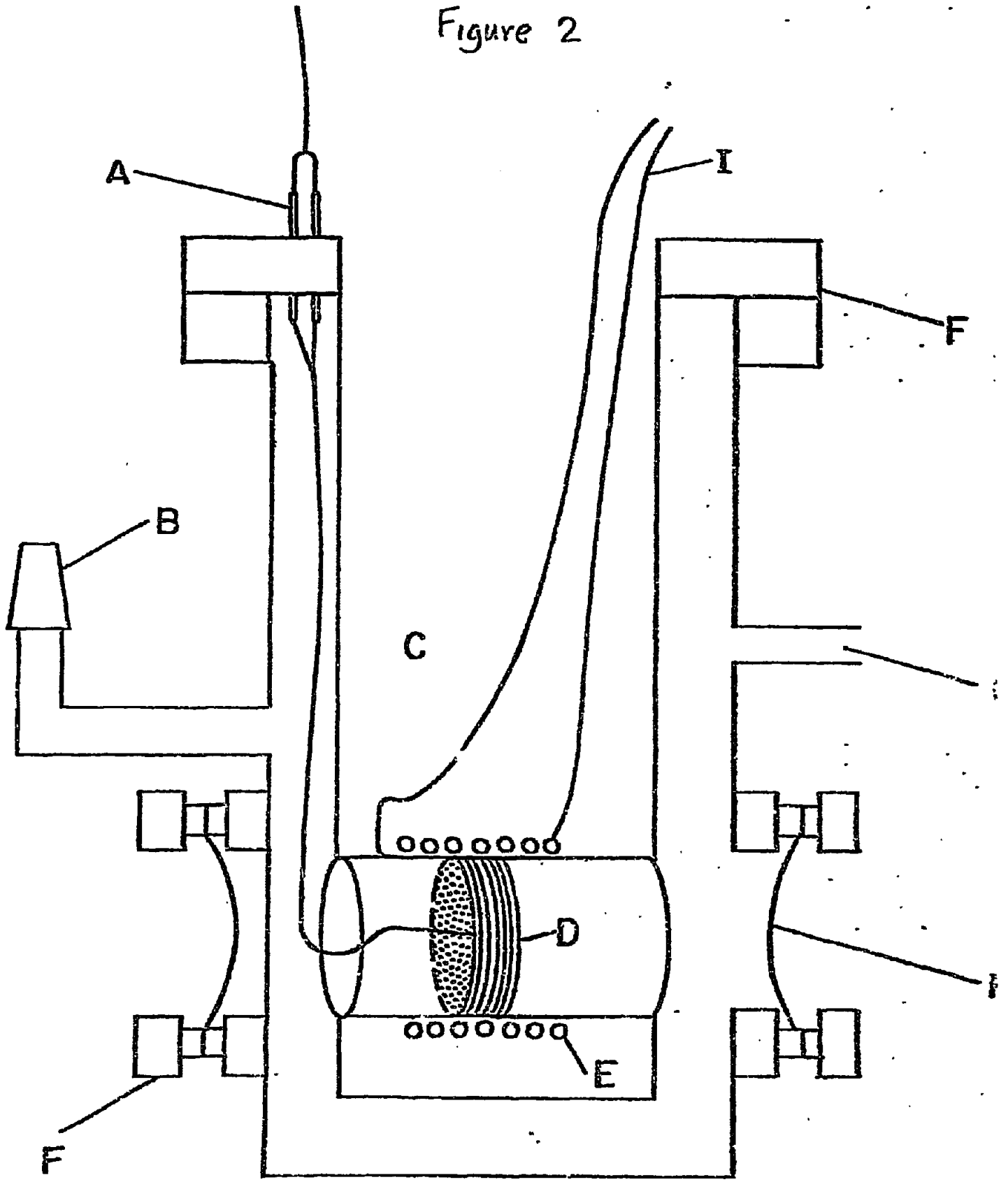




Figure 3

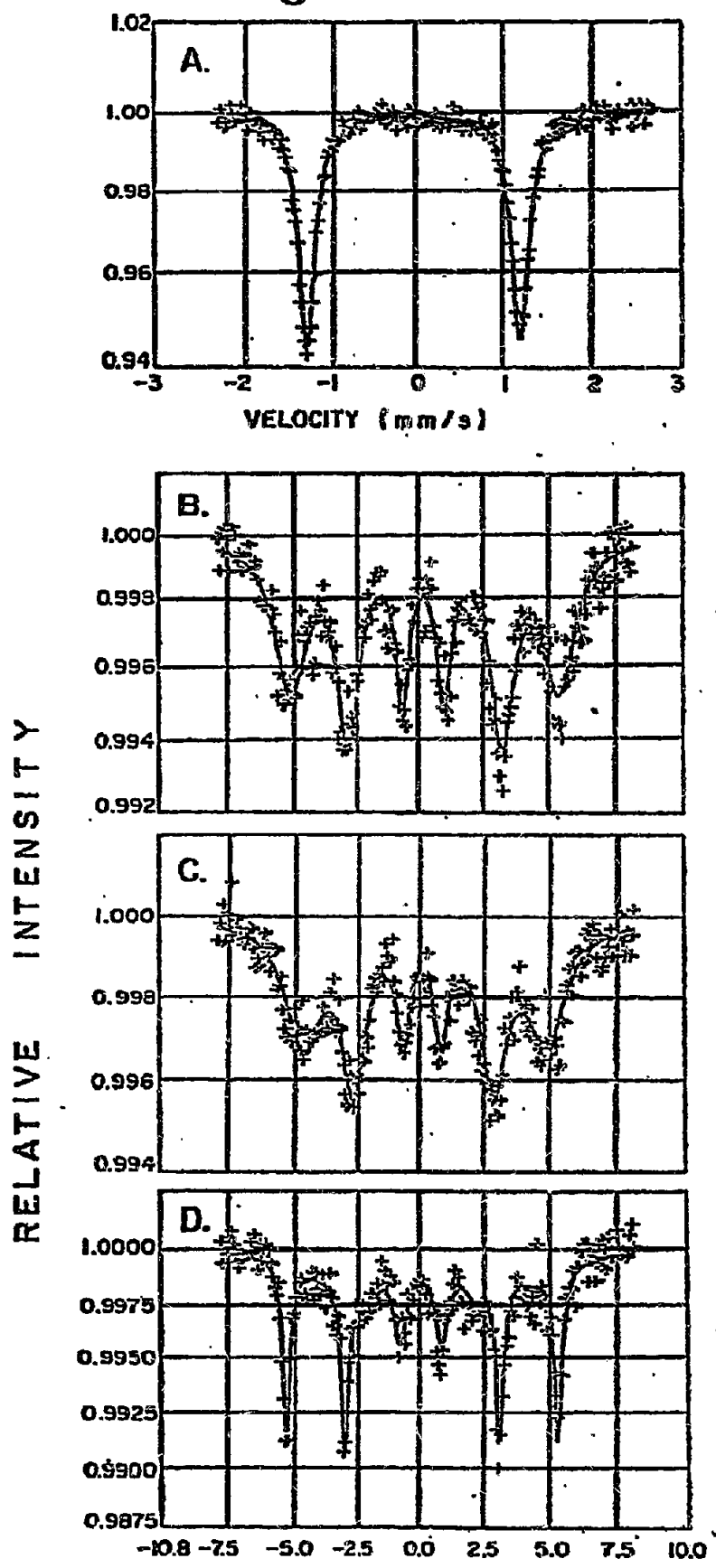
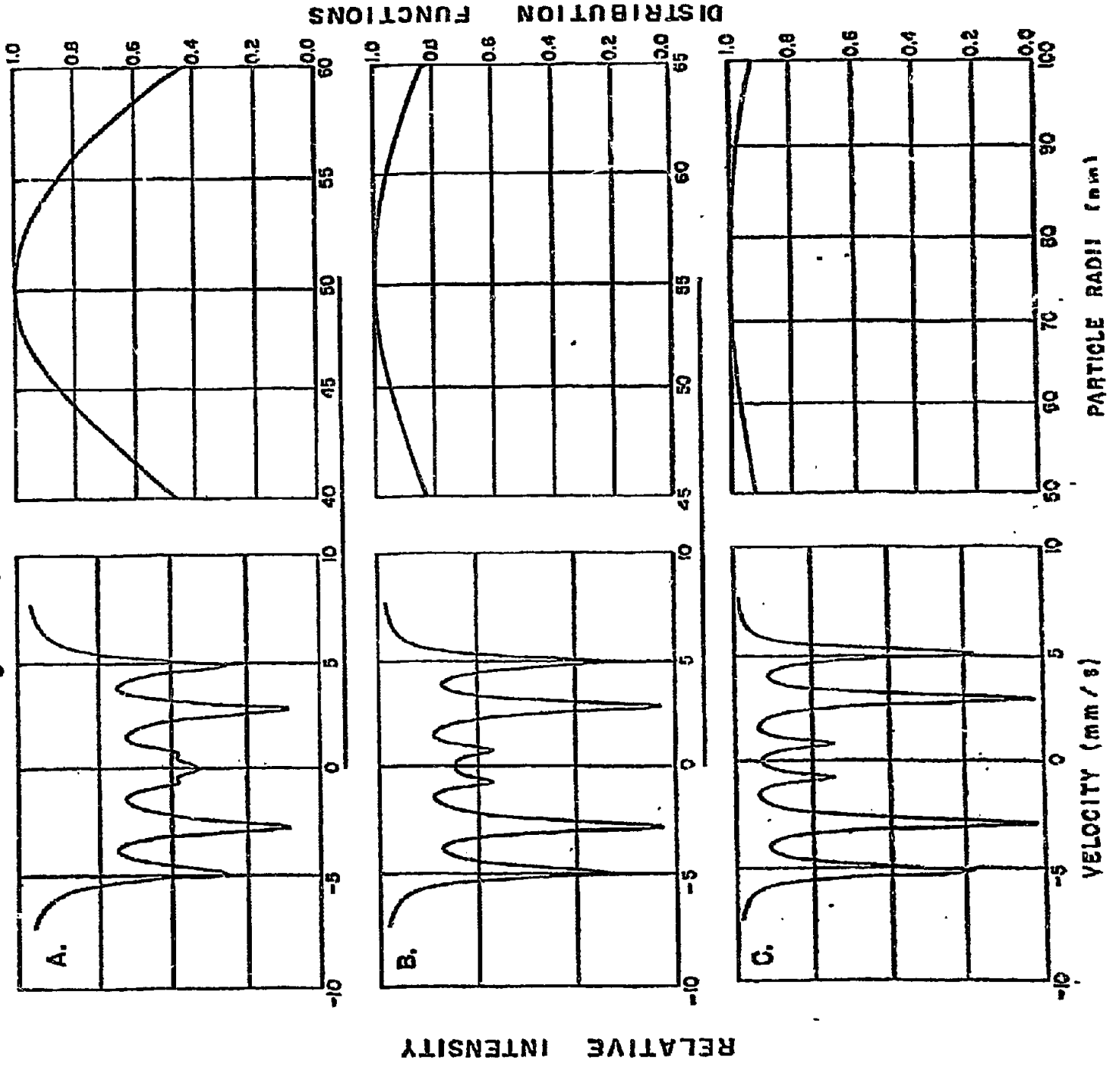


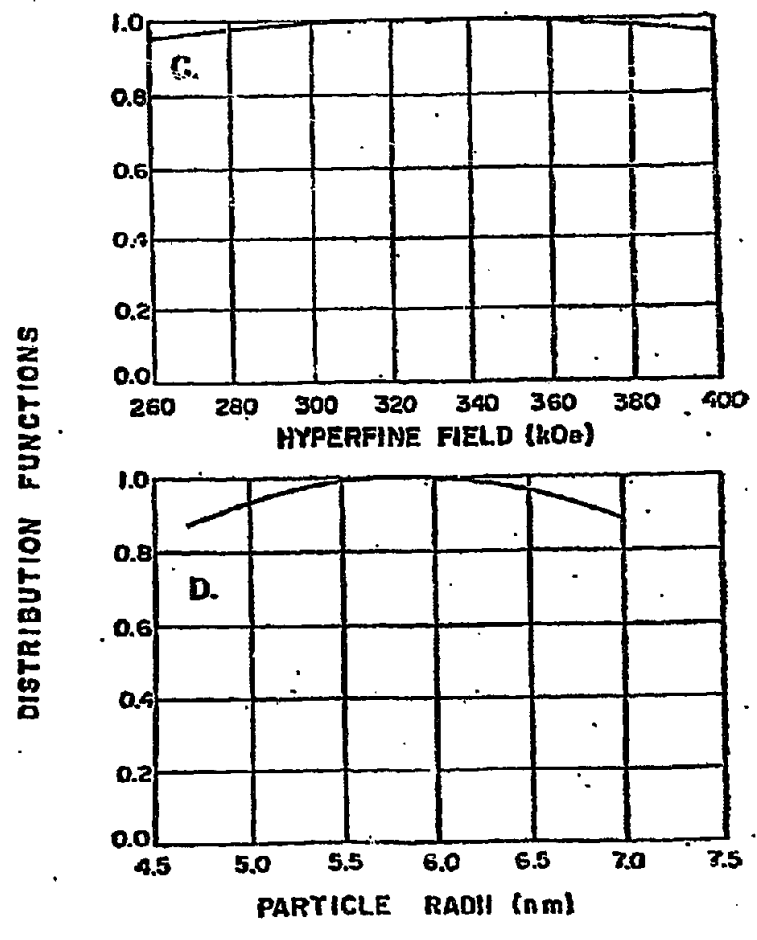
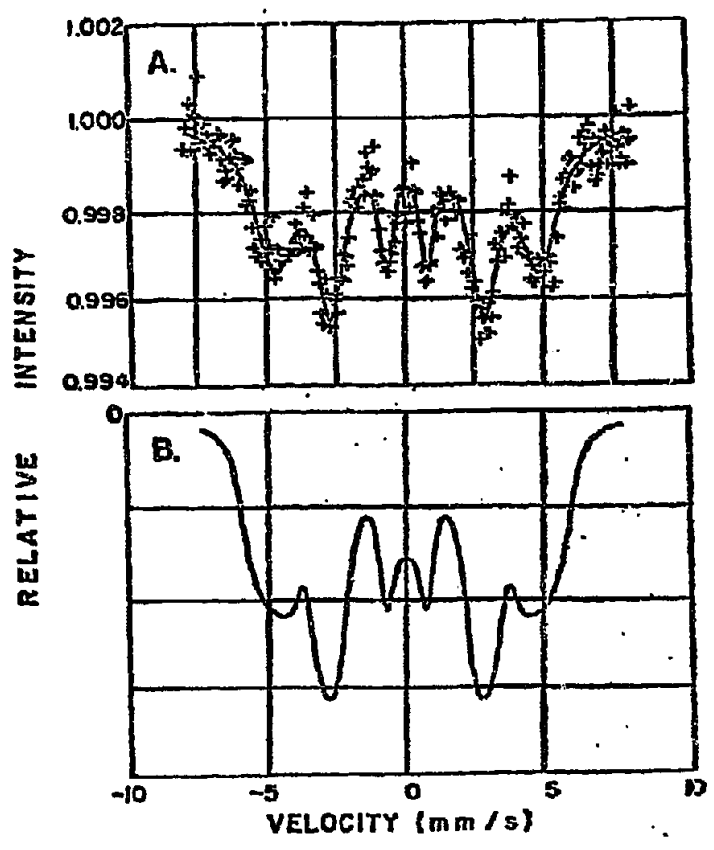


Figure 4

Reproduced from  
best available copy

Figure 5





V. Appendix C.\*

IRON PENTACARBONYL DECOMPOSITION OVER GRAFOIL-

II. Effect of Sample Outgassing on Decomposition Kinetics

\* Revised from Semi-annual Progress Report, May 1980;  
and accepted for publication in Applications  
of Surface Science.

## V.A. EXPERIMENTAL

V.A.1 Graphite Sample - The samples for both Mössbauer spectroscopy and volumetric gas phase studies were made from GTA grade "Grafoil" (Union Carbide). This material is composed of high purity, naturally occurring Madagascar graphite flakes, pressed into sheets approximately 15 mil thick (1). Grafoil has two properties which proved useful for the present study. First there is a high degree of alignment between the basal planes of the graphite microcrystals and the macroscopic Grafoil sheets (2). Secondly, the material has been measured (3) to have an average surface area of  $22 \text{ m}^2/\text{gm}$ , almost all of which is the highly uniform basal plane surface. The high surface area is required to make Mössbauer spectroscopy, in the transmission mode, a surface sensitive technique (4-7). The high surface area also serves to make Grafoil a convenient material for use in the volumetric gas phase measurements.

V.A.2 Mössbauer Spectroscopy - The Mössbauer spectroscopy cell and equipment have been described elsewhere (8). A sample made from one inch diameter Grafoil discs was outgassed in vacuum ( $10^{-4}$  Pa) in the Mössbauer spectroscopy cell at a desired temperature in the range from 77 to 623 K. Following outgassing, an amount of  $\text{Fe}(\text{CO})_5$  was permitted into the cell such that ca. 2% of the Grafoil surface would be covered by iron if monolayer iron particles were formed during decomposition. A spectrum of  $\text{Fe}(\text{CO})_5$  frozen on the Grafoil surface at 77 K was then taken. Next, decomposition at 383 K commenced. At various stages in the decomposition process the sample was cooled to ambient and/or 77 K, and a Mössbauer spectrum recorded.

The spectra, collected using a triangular wave form, were

folded and fitted using the program MFIT (9). A detailed description of the use of this program is provided elsewhere (8). All isomer shifts are reported relative to a metallic iron absorber at 300 K.

V.A.3 Volumetric Gas Phase Measurements - The all-glass apparatus used for volumetric gas phase analyses is shown schematically in Figure 1. Each Grafoil sample was first outgassed at a desired temperature in the sample cell. A liquid nitrogen trapped diffusion pump (backed by a mechanical pump) provided the vacuum for this sample pretreatment, the residual pressure being approximately  $10^{-4}$  Pa. Following completion of sample outgassing,  $\text{Fe}(\text{CO})_5$  from the transfer bulb (see Figure 1) was permitted into the main manifold. Again, the amount of  $\text{Fe}(\text{CO})_5$  permitted into the cell was stringently limited, as discussed above for the Mössbauer spectroscopy studies. The pressure of the  $\text{Fe}(\text{CO})_5$  vapor in the manifold was then measured with the precision pressure gauge (Texas Instruments). Next, the sample cell was opened to the manifold, allowing  $\text{Fe}(\text{CO})_5$  vapor to enter the sample cell and adsorb on the Grafoil surface. The drop in manifold pressure (measured with the pressure gauge) was used to determine the total amount of  $\text{Fe}(\text{CO})_5$  which had (i) adsorbed on the Grafoil surface or (ii) entered the gas phase of the previously evacuated sample cell. For the present study, the Grafoil sample size (ca. 2.0 g) and the initial pressure of the  $\text{Fe}(\text{CO})_5$  in the manifold (ca.  $10^3$  Pa) were chosen such that the majority of the  $\text{Fe}(\text{CO})_5$  (ca. 90%) was, in fact, adsorbed on the Grafoil. Following exposure of the sample to  $\text{Fe}(\text{CO})_5$  the sample cell was closed and the remaining  $\text{Fe}(\text{CO})_5$  in the

manifold (ca.  $10^2$  Pa) was pumped out using a liquid nitrogen cooled molecular sieve trap. The Grafoil sample was then rapidly heated (over a period of 5 minutes) to 383 K and subsequently held at this temperature for 1 hr. After this thermal treatment, the sample cell was rapidly cooled to room temperature, opened to the previously evacuated manifold and the pressure of the gas phase measured. The cell was then again isolated from the main manifold, heated to 383 K and held at that temperature for one hour. During this and subsequent thermal decomposition steps, the gas in the manifold was not evacuated. This procedure was repeated consecutively until the gas phase pressure in the manifold reached a constant value. It should be noted that the increase in gas phase pressure can be attributed solely to the decomposition of  $\text{Fe}(\text{CO})_5$ , since heating Grafoil alone for extended periods of time at 383 K causes no measurable increase in gas phase pressure. Furthermore, mass spectroscopic analysis of the gas phase following complete  $\text{Fe}(\text{CO})_5$  decomposition showed primarily CO, with trace amounts (less than 1%) of other gases such as  $\text{H}_2\text{O}$  and  $\text{CO}_2$ . In addition, the low initial pressure of  $\text{Fe}(\text{CO})_5$  prior to the thermal decomposition steps (less than  $10^2$  Pa) ensures that the partial pressure of CO is significantly greater than that of  $\text{Fe}(\text{CO})_5$  for total extents of decomposition greater than ca. 10%. Partial pressure measurements made during the course of the experiments also indicate that after the initial hour(s) of decomposition very little, if any,  $\text{Fe}(\text{CO})_5$  is present in the gas phase. These measurements were made by immersing into liquid nitrogen the glass appendage shown in Fig. 1. Finally,



control studies established that CO does not adsorb (to significant extent) on the surface of Grafoil at room temperature or 383 K. Thus all CO molecules released during  $\text{Fe}(\text{CO})_5$  decomposition must either (i) enter the gas phase or (ii) adsorb on the surface of decarbonylated iron species.

#### V.B. RESULTS

V.B.1. Mössbauer Spectroscopy - Experiments were designed to qualitatively determine (i) the effect of outgassing the Grafoil on the  $\text{Fe}(\text{CO})_5$  decomposition process and (ii) the identity of the iron surface species present at various stages of the decomposition process. Table I summarizes the outgassing conditions followed for each of the two samples studied.

Figure 2 shows the Mössbauer spectra (at 77 K) of the two samples after thermal decomposition of  $\text{Fe}(\text{CO})_5$  for 1 hr at 383 K. The sample outgassed at a low temperature (sample 1) shows a two-peak Mössbauer spectrum indicative of  $\text{Fe}(\text{CO})_5$ , as seen in Figure 2A (quadrupole split = 2.51 mm, isomer shift = -0.069 (10)). In contrast, the sample outgassed at a high temperature (sample 2) shows a six-peak spectrum indicative of metallic iron, as seen in Figure 2B. It can readily be concluded that the rate of  $\text{Fe}(\text{CO})_5$  decomposition is faster on the Grafoil sample subjected to the more rigorous outgassing. In Figure 3, Mössbauer spectra (at 77 K) are shown as a function of  $\text{Fe}(\text{CO})_5$  decomposition time for the

sample outgassed at low temperature. In particular, Figures 3A, 3B, 3C, and 3D correspond to 1, 4.5, 14 and 25 hr thermal decomposition times, respectively. It is important to note that only two distinct iron-containing phases can be identified during the course of the decomposition process. These are the quadrupole doublet of  $\text{Fe}(\text{CO})_5$  and the magnetically hyperfine split sextuplet of metallic iron. Accordingly, no evidence can be found for the presence of other iron carbonyls (e.g.  $\text{Fe}_2(\text{CO})_9$ ) or sub-carbonyl species. Finally, while the six-peak patterns in Figures 2B, 3B, 3C and 3D are qualitatively those of metallic iron, the Mössbauer parameters are not those of massive iron particles. The interpretation of these spectral features will be discussed later in this paper.

V.B.2. Volumetric Gas Phase Measurements - A primary objective of these measurements was to determine, after complete  $\text{Fe}(\text{CO})_5$  decomposition, the  $\text{Co(a)}/\text{Fe}$  ratio; where,  $\text{Co(a)}$  represents the number of CO molecules adsorbed on iron, and  $\text{Fe}_T$  represents the number of iron atoms produced by the decomposition process. This ratio is, in fact, a measure of the metallic iron dispersion (dispersion being defined as the fraction of the iron atoms that are surface atoms). Indeed, the calculation of this ratio is straightforward knowing the final pressure of CO in the gas phase and the initial amount of  $\text{Fe}(\text{CO})_5$  exposed to the Grafoil sample. The results of such determinations for Grafoil samples subjected to different pretreatments are summarized in Table 2. Listed therein are the parameters of the outgassing treatments given each sample, and the corresponding  $\text{Co(a)}/\text{Fe}$  ratios.

and times required to reach 99% of complete  $\text{Fe}(\text{CO})_5$  decomposition. It is clear from this table that the  $\text{CO(a)}/\text{Fe}$  ratio after complete decomposition is the same in all cases, approximately equal to 0.5. It can also be seen in Table 2 that the time required to complete the  $\text{Fe}(\text{CO})_5$  decomposition decreases as the outgassing (below 773 K) pretreatment becomes more rigorous. This result is consistent with the Mössbauer spectroscopy result. However, on the Grafoil sample treated at 1273 K the rate of decomposition is seen to be somewhat slower than the samples outgassed at 773 K and 673 K. This is explained in the discussion section.

As demonstrated by Mössbauer spectroscopy,  $\text{Fe}(\text{CO})_5$  and metallic iron are the only two iron-containing species present during the decomposition process. If it is assumed that the morphology of the metallic iron phase remains unchanged during the course of the decomposition (as will be discussed later), then it follows that the  $\text{CO(a)}/\text{Fe}$  ratio would equal 0.5 at all stages of  $\text{Fe}(\text{CO})_5$  decomposition. It is then possible to determine the extent of  $\text{Fe}(\text{CO})_5$  decomposition versus time by simply measuring the gas phase CO pressure versus time. Since five CO molecules are released when one  $\text{Fe}(\text{CO})_5$  molecule decomposes, and since  $\text{CO(a)}/\text{Fe}$  equals 0.5, it follows that 4.5 molecules of CO are released into the gas phase per molecule of  $\text{Fe}(\text{CO})_5$  decomposed. Accordingly, the extent of  $\text{Fe}(\text{CO})_5$  decomposition,  $x$ , is given by:

$$x = \frac{n_{\text{CO}}}{4.5 n_{\text{Fe}(\text{CO})_5}}$$

where  $n_{\text{CO}}$  is the number of gas phase CO molecules (in the manifold and sample cell) and  $n_{\text{Fe}(\text{CO})_5}$  is the number of  $\text{Fe}(\text{CO})_5$  molecules initially exposed to the Grafoil sample.

Figure 4 shows plots of  $x$  versus time for Grafoil samples subjected to various outgassing pretreatments. These curves show quantitatively that the rate of  $\text{Fe}(\text{CO})_5$  decomposition increases with the severity of the outgassing step (below 773 K). Figure 5 is a semi-log plot of  $(1 - x)$  versus time. After the initial stages of reaction,  $\text{Fe}(\text{CO})_5$  decomposition on Grafoil is a first order process, described by an exponential decay of  $(1 - x)$  with time.

#### V.C. DISCUSSION

V.C.1 Mössbauer Spectroscopy - As shown above, the results of Mössbauer spectroscopy indicate that only two iron-containing species are present during the course of  $\text{Fe}(\text{CO})_5$  decomposition over Grafoil: metallic iron and iron pentacarbonyl. Yet it was also noted that the Mössbauer parameters for the metallic iron phase were not identical to those of bulk metallic iron. This is shown quantitatively in Table 3, which is a summary of the results of computer fitting the spectra shown in Figures 2 and 3. For bulk metallic iron the magnetic hyperfine field should be 340 kOe, the line widths should be ca.  $0.25 \text{ mm s}^{-1}$ , and the isomer shift should be  $.120 \text{ mm s}^{-1}$  (relative to the isomer shift of metallic iron at 300 K). It can be seen in Table 3 that the spectra of metallic iron produced on Grafoil via  $\text{Fe}(\text{CO})_5$  decomposition have a smaller magnetic hyperfine

field, broader peaks, and a more positive isomer shift than the spectra of bulk metallic iron.

The origin of the reduced magnetic hyperfine field and the broadened peaks of metallic iron on Grafoil outgassed at 723 K has been discussed in detail in Part I of this investigation (8). In short, computer simulations were performed to analyze the Mössbauer spectra after complete decomposition of  $\text{Fe}(\text{CO})_5$ . It was suggested on the basis of these simulations that the iron particles produced were thin (high surface to volume ratio) "rafts" on the order of 1 nm thick and 10 nm in lateral dimension.

In the present investigation computer simulations were made of Mössbauer spectra after various extents of  $\text{Fe}(\text{CO})_5$  decomposition. This was done in order to determine if the morphology of the iron particles is the same at all stages of  $\text{Fe}(\text{CO})_5$  decomposition. Following the procedure established in Part I of the investigation, the metallic iron component of the spectrum was generated taking into account the combined effects of particle size and surface/interface effects. The spectrum of  $\text{Fe}(\text{CO})_5$  absorbed on graphite at 77 K was added to the metallic iron spectrum to complete the overall simulation.

The results of this procedure are shown in Figure 6 for the simulation of one observed spectrum (Figure 3C). The chosen distributions of particle volume and magnetic hyperfine field that adequately reproduced the metallic iron part of the observed spectrum are also shown in Figure 6. It can be seen in this figure that the simulation reproduces the reduced

magnetic hyperfine field and the broad background dip centered at zero velocity (both effects due to magnetic relaxation caused by the small particle size (11-15)), and it also reproduces the relative broadening of the outer peaks (due to the hyperfine field distribution caused by interface/surface effects (16-18)).

It is not implied that the distributions used for the simulation necessarily have quantitative validity. The important conclusion to be drawn is that the simulation procedure and parameters used to interpret the Mössbauer spectra from metallic iron particles produced after complete  $\text{Fe}(\text{CO})_5$  decomposition on Grafoil outgassed at 723 K are the same as those used to simulate the spectra from metallic iron particles produced after partial  $\text{Fe}(\text{CO})_5$  decomposition on less-rigorously outgassed Grafoil. It then follows that the morphology of metallic iron particles on Grafoil is the same after various outgassing pretreatments and extents of  $\text{Fe}(\text{CO})_5$  decomposition. While Mössbauer spectroscopy alone is consistent with the presence of thin, metallic iron rafts on all samples, it is the combined consideration of Mössbauer spectroscopy and volumetric gas phase measurements that clearly demonstrates that these thin rafts do, in fact, exist. This will be discussed below.

#### V.C.2. Volumetric Gas Phase Measurements

V.C.2.a. Metallic Iron Morphology - Titration of iron containing surfaces with CO has long been used as a means of measuring the iron surface area. Adsorption studies have shown that CO chemisorbs on small iron particles with the stoichiometry of one CO for every two surface iron atoms (19-21). Thus the

CO(a)/Fe ratio of 0.5 obtained repeatedly in these experiments after complete Fe(CO)<sub>5</sub> decomposition, suggests that essentially all of the iron atoms are surface atoms. This leads to the following conclusion: the metallic iron particles are present as thin rafts, probably one or two atomic layers thick. This conclusion is far more specific than that drawn from the Mössbauer studies. However, it is consistent with the conclusion drawn from those studies. Very small metallic iron particles containing ca. 10-20 atoms would be consistent with this CO(a)/Fe ratio; however, these particles would be superparamagnetic in the room temperature Mössbauer spectra, showing only a spectral singlet or a two-peak spectrum. Instead, the presence of thin metallic iron rafts explains both the observed CO(a)/Fe ratio and the six-peak Mössbauer spectra.

Generally small metal particles formed on refractory substrates are assumed to be three-dimensional (e.g. semi-spherical). However, there are several instances reported of metal particles forming thin, raft-like structures on refractory substrates. Ruckenstein and Chu (22) suggested that platinum crystallites supported on  $\gamma$ -alumina will spread to form two-dimensional structures when heated in an oxidizing atmosphere. It has also been found that for low metal loadings Ru, Os and Rh will form monolayer "rafts" on silica (23,24). Metal carbonyl decomposition has led to the production of very highly dispersed structures as well. Brenner et al. (25-28) reported that Mo(CO)<sub>6</sub> decomposed on hydroxylated  $\gamma$ -alumina produced mono-dispersed molybdenum species. Nagy et al. (29) contend that iron pentacarbonyl decomposition on HY zeolites at low

temperatures produces iron structures which are 100% dispersed. Howard and Nussbaum (30) suggest that the oxidation of  $\text{Fe}(\text{CO})_5$  on graphite creates a monolayer film of  $\text{Fe}_2\text{O}_3$ . Thus it is clear that there is precedent for suggesting that one or two layer thick metal iron particles could be formed at 383 K on Grafoil.

It is not possible to determine unequivocally the physical basis for the stability of the iron rafts. However, it seems unlikely that it results from a strong iron-graphite interaction as it has been shown (8) that the particles sinter at 450 K. Hence, it seems plausible to suggest that the raft geometry is metastable. That is, the energy required to desorb (or dissociate (8)) the chemisorbed CO as well as the energy required to break the weak bonds between iron and graphite may provide sufficient activation energy barriers to stabilize iron rafts at 383 K.

V.C.2.b. Decomposition Kinetics - In the following discussion it is assumed that particle nucleation and growth occur at a finite number of sites on the Grafoil surface. This assumption is consistent with previous studies of graphitic materials (discussed later). It is also reasonable to assume, since  $\text{Fe}(\text{CO})_5$  is only weakly adsorbed on Grafoil (8), that the flux of  $\text{Fe}(\text{CO})_5$  to the nucleation and growth sites is via a mobile, adsorbed species. Furthermore, the Mössbauer spectroscopy results indicate that only two species are present on the Grafoil surface at any time. Thus, the  $\text{Fe}(\text{CO})_5$  decomposition may be treated as a single step process: from molecular  $\text{Fe}(\text{CO})_5$  to metallic iron particle. Accordingly, one can



$$\frac{dn_{\text{Fe}(\text{CO})_5}}{dt} = -kA\rho n_{\text{Fe}(\text{CO})_5}$$

where  $n_{\text{Fe}(\text{CO})_5}$  is the number of  $\text{Fe}(\text{CO})_5$  molecules in the system,  $A$  is the Grafoil area that is swept out (on an average) by each  $\text{Fe}(\text{CO})_5$  molecule in one second,  $\rho$  is the number of nucleation and growth sites per unit area of Grafoil and  $k$  is the probability that a  $\text{Fe}(\text{CO})_5$  molecule will decompose upon encountering a nucleation and growth site. The observed exponential variation of decomposition rate with time follows simply from this rate expression:

$$\left[ 1 - \frac{n_{\text{Fe}(\text{CO})_5}}{n_{\text{Fe}(\text{CO})_5}^0} \right] \cong 1 - x = 1 - e^{-kA\rho t}$$

It should be remembered here that the decomposition kinetics are not first order during the initial stages of decomposition. The presence of this "induction period" may be attributable to the presence of gas phase  $\text{Fe}(\text{CO})_5$  at short reaction times, since the treatment of the experimental data assumes that all  $\text{Fe}(\text{CO})_5$  is adsorbed on the Grafoil surface at room temperature. It is also possible that the rate constant  $k$  does not reach a constant value until the iron particles have attained a certain size.

In the present study it is important to note that the decomposition rate increases as the Grafoil outgassing becomes more rigorous (below 773 K). In terms of the above model for the first order decomposition kinetics, this would be interpreted as a dependence of  $kA\rho$  on outgassing conditions. For the sake of discussion, this factor will be divided into two terms:  $kA$  and  $\rho$ . The first term,  $kA$ , is the decomposition rate

per nucleation and growth site and the second term,  $\rho$ , is the number of such sites per unit area of Grafoil.

V.C.2.c. Effects of Grafoil Outgassing - Through analysis of the Mössbauer spectra it is possible to suggest which of the factors in the kinetic rate expression (i.e.  $kA$  and/or  $\rho$ ) are modified during outgassing of Grafoil. Table 3 contains the results of computer analyses of the spectra contained in Figures 2 and 3. For the series of spectra on the sample having experienced the low temperature outgassing (Figure 3), the average magnetic hyperfine field decreases, the line width increases and the isomer shift becomes more positive as the  $\text{Fe}(\text{CO})_5$  decomposition process proceeds. Since it is expected that the metallic iron particle size grows with continued  $\text{Fe}(\text{CO})_5$  decomposition, it seems reasonable to correlate these systematic variations in Mössbauer parameters with increasing particle size. In this case it becomes possible to use in situ Mössbauer spectroscopy for the comparison of iron particle sizes on Grafoil surfaces subjected to various outgassing treatments. Table 3 shows this comparison. It can be seen that the Mössbauer parameters for metallic iron on the more rigorously outgassed Grafoil (sample 2; spectrum 2B) are well within the range spanned by the Mössbauer parameters for the series of metallic iron particles on less-rigorously outgassed Grafoil (sample 1; spectra 3B, 3C, 3D). In fact, the Mössbauer parameters for metallic iron on sample 1 after complete  $\text{Fe}(\text{CO})_5$  decomposition are very close to those on sample 2 after ca. 80%  $\text{Fe}(\text{CO})_5$  decomposition. It is, therefore, suggested that the thin iron rafts are of similar size on both samples after comparable

It was concluded above that  $kA$  and/or  $\rho$  increase as the Grafoil outgassing becomes more rigorous. However, since the results of Mossbauer spectroscopy suggest that the iron particle size is similar on all samples, it follows that  $\rho$  must be essentially independent of the Grafoil outgassing treatment. Hence, it must be the term  $kA$  in the kinetic rate expression that varies with sample pretreatment. That is, as the outgassing treatment becomes more rigorous (below 773 K), the number density of nucleation and growth sites remains essentially constant, but the reactivity of the Grafoil surface increases. This may reflect a higher reactivity of the sites themselves (increase in  $k$ ) and/or a faster rate of diffusion for the mobile  $\text{Fe}(\text{CO})_5$  species on the surface (increase in  $A$ ). For example, water, which could serve as a diffusion barrier, is known to desorb from graphite between 300 and 900 K (31,32).

It seems likely that the nucleation sites are "oxygen free" edge and/or defect sites on the Grafoil surface. There are three reasons to suggest this model. First, this model is consistent with previous TEM studies which show particles forming preferentially along graphite edges (8). Second, previous studies have shown that the only significant chemical change which occurs on a graphite surface at relatively low outgassing temperatures (less than 1000 K) is the removal of oxygen-containing species, presumably from edges and defects (33-36). Finally, other investigators have reported that the reactivity of graphite is reduced by high temperature treatment (e.g. 1273 K) due to the annealing of basal plane dislocations initially introduced during mechanical processing

in the rate of  $\text{Fe}(\text{CO})_5$  decomposition when the Grafoil outgassing temperature is increased from 773 to 1273 K.

#### V.D. CONCLUSIONS

Interpretation of the Mössbauer spectra suggests that the metallic iron particles formed following decomposition of  $\text{Fe}(\text{CO})_5$  on Grafoil at 383 K consist of many iron atoms, yet these particles possess a high surface to volume ratio. Volumetric gas phase measurements indicated that following complete decomposition of  $\text{Fe}(\text{CO})_5$ , one molecule of CO was absorbed on the sample for every two atoms of metallic iron formed. These results suggest that the metallic iron particles are thin rafts, probably one or two atomic layers thick, covered by a chemisorbed layer of CO. By comparison, previous studies of the formation of metallic iron particles on graphitic material using an impregnation technique have shown that only large (ca. 40 nm), three-dimensional particles can be made in that manner (39).

It has also been shown that the decomposition of iron pentacarbonyl on Grafoil is a first order process which takes place on edges and other defects on the Grafoil surface. Furthermore outgassing of the Grafoil at temperature below 773 K was found to increase the rate of decomposition without significantly changing the number of decomposition sites. Outgassing at 1273 K was found to reduce the reactivity of Grafoil, probably due to the annealing of surface defects which previously had acted as nucleation sites.

## V.E. REFERENCES

- [1] M. Bretz, J. G. Dash, D. C. Hickernell, E. O. Mclean and O. E. Vilches, Phys. Rev. A8 (1973) 1589.
- [2] J. K. Kjems, L. Passell, H. Taub, J. G. Dash and A. D. Novao, Phys. Rev. B13 (1976) 1446.
- [3] R. L. Elgin and D. L. Goodstein, Phys. Rev. A9 (1974) 265.
- [4] S. Bukshpan, Phys. Lett. A62 (1977) 109.
- [5] S. Bukshpan, T. Sonnino and J. G. Dash, Surf. Sci. 52 (1975) 466.
- [6] J. K. Kjems, L. Passell, H. Taub and J. G. Dash, Phys. Rev. Lett. 32 (1974) 724.
- [7] H. Schecter, J. G. Dash, M. Mor, R. Ingalls and S. Bukshpan, Phys. Rev. B14 (1976) 1876.
- [8] See Appendix B; J. Phillips, B. S. Clausen and J. A. Dumesic, J. Phys. Chem. 84 (1980) 1814.
- [9] K. Sørensen, Lab of Applied Physics II, Tech. Univ. of Denmark, Lyngby, Denmark, Internal Report #1 (1972).
- [10] K. Farmery, M. Kilner, R. Greatrex and N. N. Greenwood, J. Chem. Soc. A. (1969) 2339.
- [11] S. Mørup and H. Topsøe, Appl. Phys. 11 (1976) 63.
- [12] S. Mørup, H. Topsøe and J. Lipka. J. Phys. (Paris) Colloq. 37 (1976) C6-287.
- [13] S. Mørup, J. A. Dumesic and H. Topsøe, in: Applications of Mössbauer Spectroscopy, Ed. R. L. Cohen, Vol. 2 (Academic Press, in press).
- [14] A. Aharoni, Phys. Rev. A135 (1964) 447.
- [15] W. F. Brown, Phys. Rev. 130 (1963) 1677.
- [16] H. Topsøe, J. A. Dumesic and S. Mørup, in: Applications of Mössbauer Spectroscopy, Ed. R. L. Cohen, Vol. 2 (Academic Press, in press).
- [17] T. Shinjo, IEEE Trans. Mag. 12 (1976) 86.
- [18] S. Mørup, B. S. Clausen and H. Topsøe, J. Phys. (Paris) Colloq. 40 (1979) C2-78.
- [19] J. A. Dumesic, H. Topsøe, S. Khammouma and M. Boudart, J. Cat. 37 (1975) 503.

- [21] N. Nahon, V. Perrichon, P. Turlier and P. Bussiere, *Reaction Kinet. Catal. Lett.* 11 (1979) 28.
- [22] E. Ruckenstein and Y. F. Chu, *J. Cat.* 59 (1979) 109.
- [23] E. B. Prestridge, G. H. Via and J. H. Sinfelt, *J. Cat.* 50 (1977) 115.
- [24] D. J. C. Yates, L. L. Murrell and E. B. Prestridge, *J. Catal.* 57 (1979) 41.
- [25] R. L. Burwell, Jr. and A. Brenner, *J. Mol. Cat.* 1 (1976) 77.
- [26] A. Brenner and R. L. Burwell, Jr., *J. Cat.* 52 (1978) 353.
- [27] A. Brenner and R. L. Burwell, Jr., *J. Cat.* 52 (1978) 364.
- [28] A. Brenner and R. L. Burwell, Jr., *J. Am. Chem. Soc.* 97 (1975) 2565.
- [29] J. B. Nagy, M. Van Eenoo and E. G. Derouane, *J. Cat.* 58 (1979) 230.
- [30] D. G. Howard and R. H. Nussbaum, *Surf. Sci. Lett.* 93 (1980) L105.
- [31] R. B. Anderson and P. H. Emmett, *J. Phys. Chem.* 56 (1952) 753.
- [32] R. B. Anderson and P. H. Emmett, *J. Phys. Chem.* 51 (1947) 1308.
- [33] G. R. Hennig, in: *Proceedings of the Fifth Conf. on Carbon*, Vol. 1 (Pergamon Press, N.Y., 1962) pg. 143.
- [34] H. H. Harker, J. B. Horsley and D. Robson, *Carbon* 9 (1971) 1.
- [35] N. R. Laine, F. J. Vastola and P. L. Walker, Jr., *J. Phys. Chem.* 67 (1963) 2030.
- [36] S. S. Barton and B. H. Harrison, *Carbon* 10 (1972) 245.
- [37] S. Mrozowski and J. P. Andrew, in: *Proceedings of the Fourth Conf. on Carbon*, Vol. 1 (Pergamon Press, N.Y., 1960) pg. 207.
- [38] S. Barton, B. H. Harrison and J. Dollimore, *J. Phys. Chem.* 82 (1978) 290.

LIST OF TABLES

Table 1: Sample Preparation for Mössbauer Spectroscopy

Table 2: Kinetics of  $\text{Fe}(\text{CO})_5$  Decomposition

Table 3: Computer Fit Parameters for Mössbauer Spectra of  
Metallic Iron Particles Formed from the Thermal  
Decomposition of Iron Pentacarbonyl on Grafoil

TABLE 1 - SAMPLE PREPARATION FOR MÖSSBAUER SPECTROSCOPY

<u>MÖSSBAUER</u> <u>SAMPLE</u>	<u>FIGURE</u>	<u>MASS</u> <u>(g)</u>	<u>OUTGASSING CONDITIONS</u>		
			<u>PRESS.</u> <u>(Pa)</u>	<u>TEMP.</u> <u>(K)</u>	<u>TIME</u> <u>(hr)</u>
1	2A,3	5.1	$6.5 \times 10^{-3}$	295	5
2	2B	7.9	$1.5 \times 10^{-2}$	723	10



TABLE 2 - KINETICS OF  $\text{Fe}(\text{CO})_5$  DECOMPOSITION

KINETICS SAMPLE	SYMBOL KEY (Figs. 4 & 5)	MASS (g)	OUTGAS			TIME REQUIRED TO COMPLETE DECOMPOSITION (hr)	CO(a)/Fe AFTER COMPLETE DECOMPOSITION
			PRESS. (Pa)	TEMP. (K)	TIME (hr)		
1	x	1.58	$6.5 \times 10^{-3}$	773	4.5	.5	1.97
2 <sup>‡</sup>	-	1.50	$6.5 \times 10^{-3}$	673	5	.5	2.05
3	○	2.72	$1.5 \times 10^{-2}$	573	6	3	2.01
4	□	2.53	$1.5 \times 10^{-1}$	473	2	6	2.00
5	+	2.57	$1.5 \times 10^{-1}$	383	2.5	~100	1.98
6	△	1.89	$1.5 \times 10^{-1}$	383	5	*	*
7 <sup>‡</sup>	-	2.92	$1.5 \times 10^{-2}$	1273	1	3	1.91

<sup>‡</sup> Samples used only to determine times required to complete  $\text{Fe}(\text{CO})_5$  decomposition and CO(a)/Fe ratios after complete decomposition.

\* Kinetics only measured for times up to 14 hr; however, in Figs. 4 and 5 it can be seen that samples 5 and 6 show similar kinetics.

TABLE 3 - COMPUTER FIT PARAMETERS FOR MOSSBAUER SPECTRA OF METALLIC IRON PARTICLES FORMED FROM THE THERMAL DECOMPOSITION OF IRON PENTACARBONYL ON GRAFOIL

SPECTRUM	SPECTRUM TEMP. (K)	SEXTUPLET			PERCENT OF TOTAL SPECTRAL AREA
		AVG. HYPERFINE FIELD (kOe)	ISOMER SHIFT (mm/sec) (Relative to Fe)	LINE WIDTHS (mm/sec) 1,6/2,5/3,4	
2A, 3A	77	-	-	-	0
3B	77	333	.019	1.1/1.2/2.2	55
3C	77	326	.158	1.6/1.7/1.4	80
3D	77	306	.226	2.2/2.1/0.7	100
2B	77	329	.140	1.5/1.2/0.7	100
1 mil Fe foil	77	340	.120	0.28/0.25/0.23	-

LIST OF FIGURES

- Figure 1: Glass Apparatus for Volumetric Gas Phase Analysis. A) Glass appendage for partial pressure analysis. B) Quartz sample cell. C) Molecular sieve trap (13X). D) Iron pentacarbonyl transfer bulb. E) Texas Instruments precision pressure gauge. F) Main manifold. G) Vacuum line. H) Purified gases.
- Figure 2: Effect of Outgassing on the Rate of  $\text{Fe}(\text{CO})_5$  Decomposition. Mössbauer spectra of  $\text{Fe}(\text{CO})_5$  decomposed at 383 K for one hour on Grafoil which had been (A) outgassed at 295 K (Table 1 - sample 1) and (B) outgassed at 723 K (Table 1 - sample 2).
- Figure 3: Mössbauer Spectral Record of Iron Containing Surface Species Present after Various Stages of  $\text{Fe}(\text{CO})_5$  Decomposition on Grafoil Outgassed at 295 K (Table 1 - Sample 1). (All spectra recorded at 77 K.) A) After 1.0 hour at 383 K. B) After 4.5 hours at 383 K. C) After 14 hours at 383 K. D) After 25 hours at 383 K.
- Figure 4: Extent of  $\text{Fe}(\text{CO})_5$  Decomposition at 383 K as a Function of Time and Temperature of Grafoil Outgassing. The key to this figure is given in Table 2.
- Figure 5: Kinetics of  $\text{Fe}(\text{CO})_5$  Decomposition on Grafoil at 383 K. The key to this figure is given in Table 2.
- Figure 6: Computer Simulation of Combined Effects of Hyperfine Field Distribution and Magnetic Relaxation on the Mössbauer Spectrum of Metallic Iron. Iron pentacarbonyl, representing 20 percent of the total spectral area, was added to the six-peak metallic iron spectrum. A) Mössbauer spectrum (same as Fig. 3C) taken at 77 K after 19 hours of  $\text{Fe}(\text{CO})_5$  decomposition at 383 K on Grafoil outgassed at 295 K (Table 1 - sample 1). B) Simulated Mössbauer Spectrum. C) Assumed hyperfine field distribution. D) Assumed particle radius distribution (for semi-spherical particles). In the simulation it was assumed that the anisotropy energy constant was  $5 \times 10^5 \text{ ergs/cm}^3$ ,  $T = 77 \text{ K}$  and the peak area ratios for the six-peak pattern were 3:3:1:1:3:3.

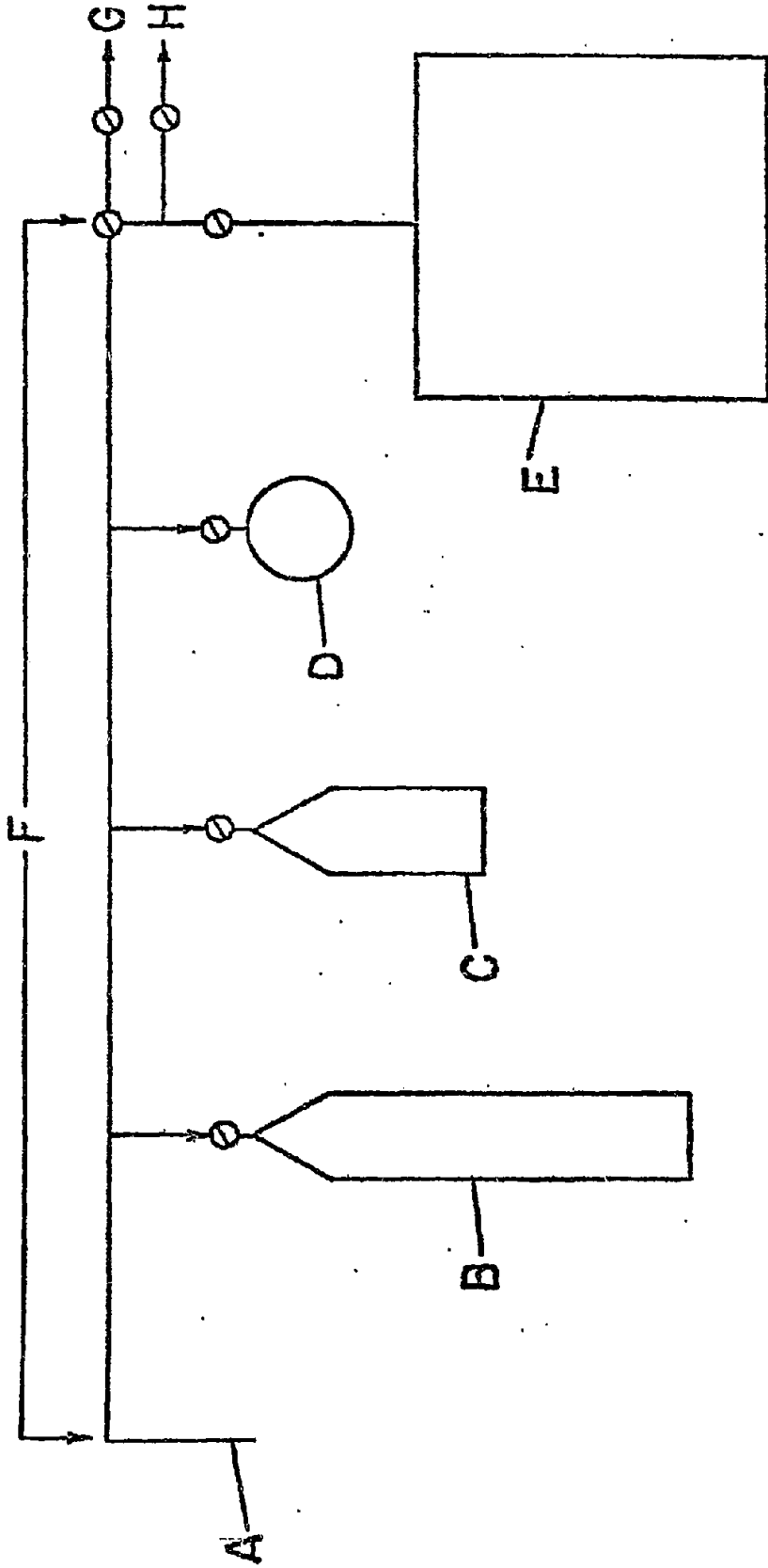


Figure 1

Figure 2

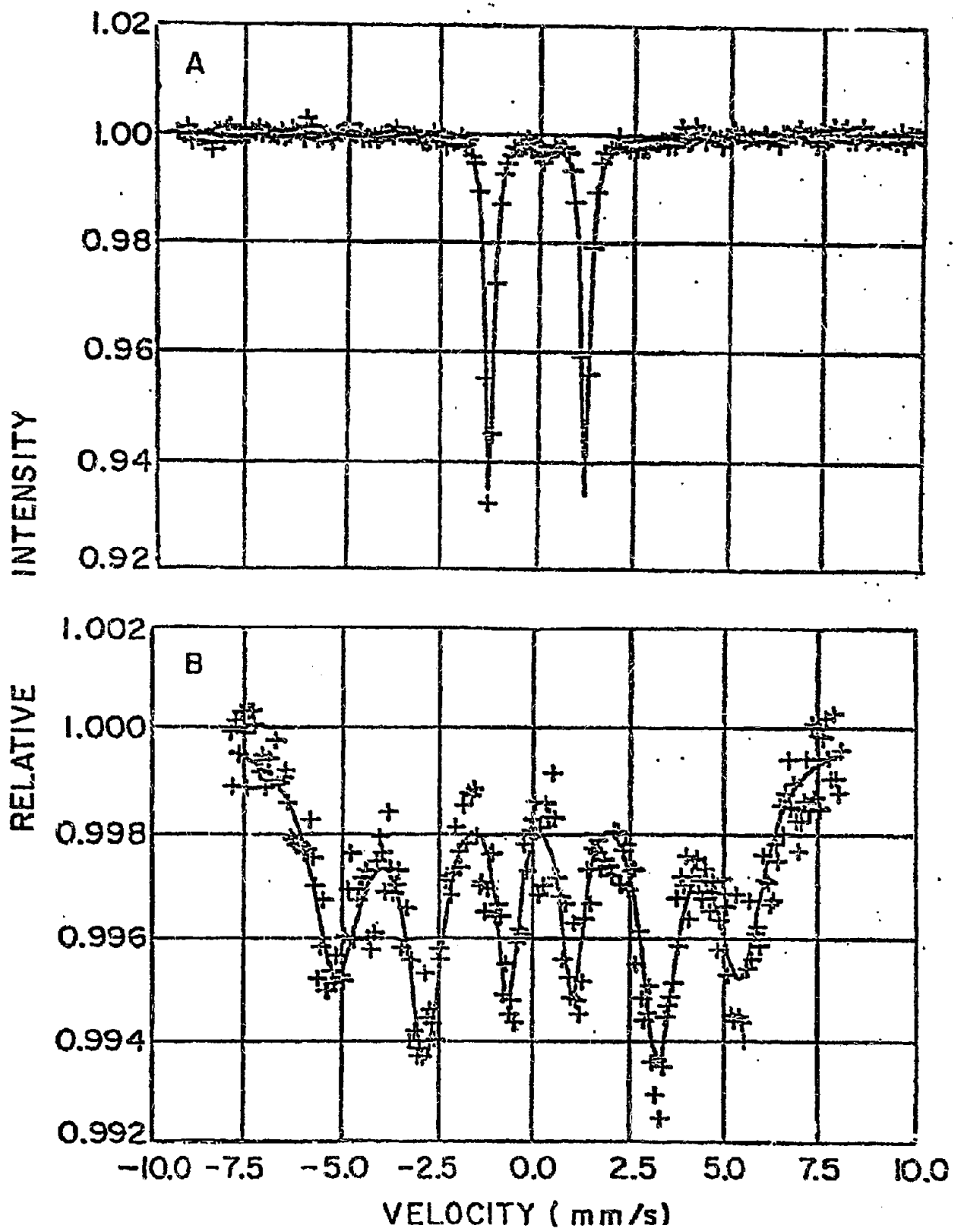
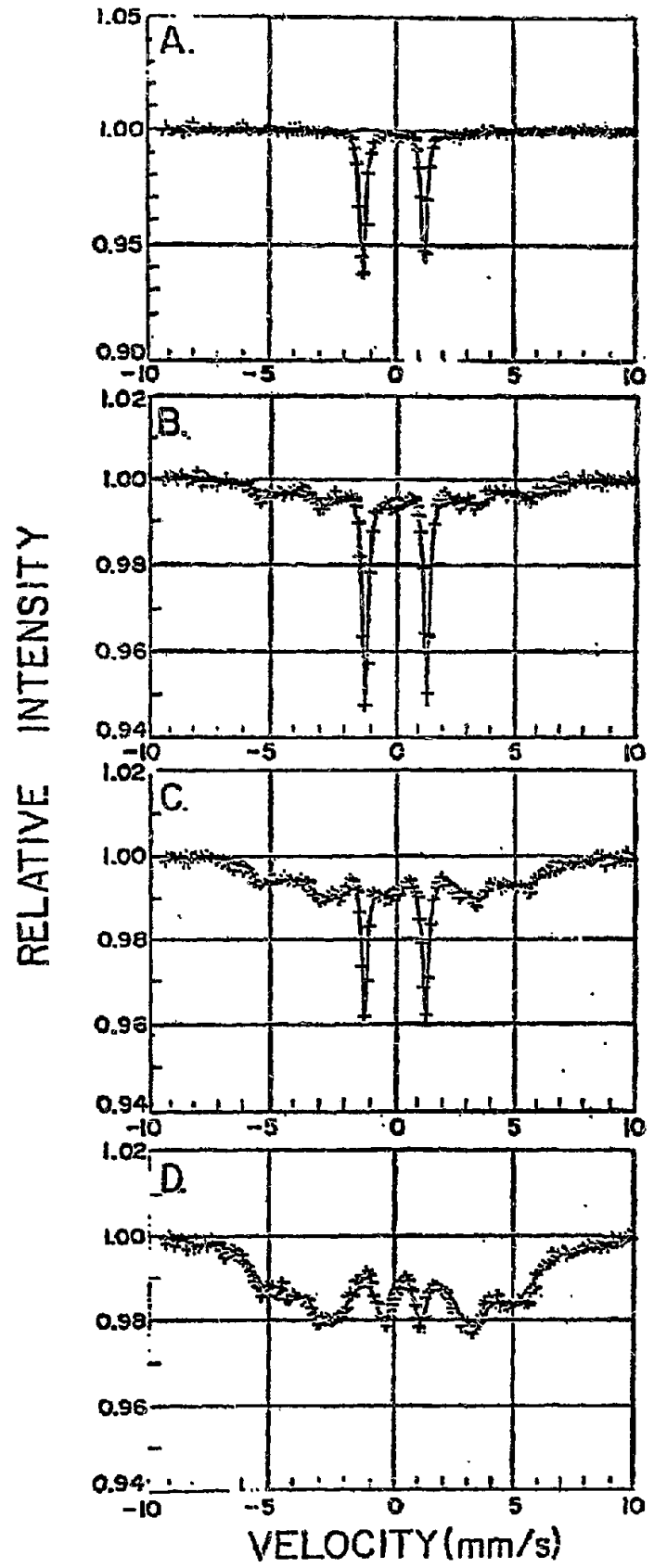


Figure 3



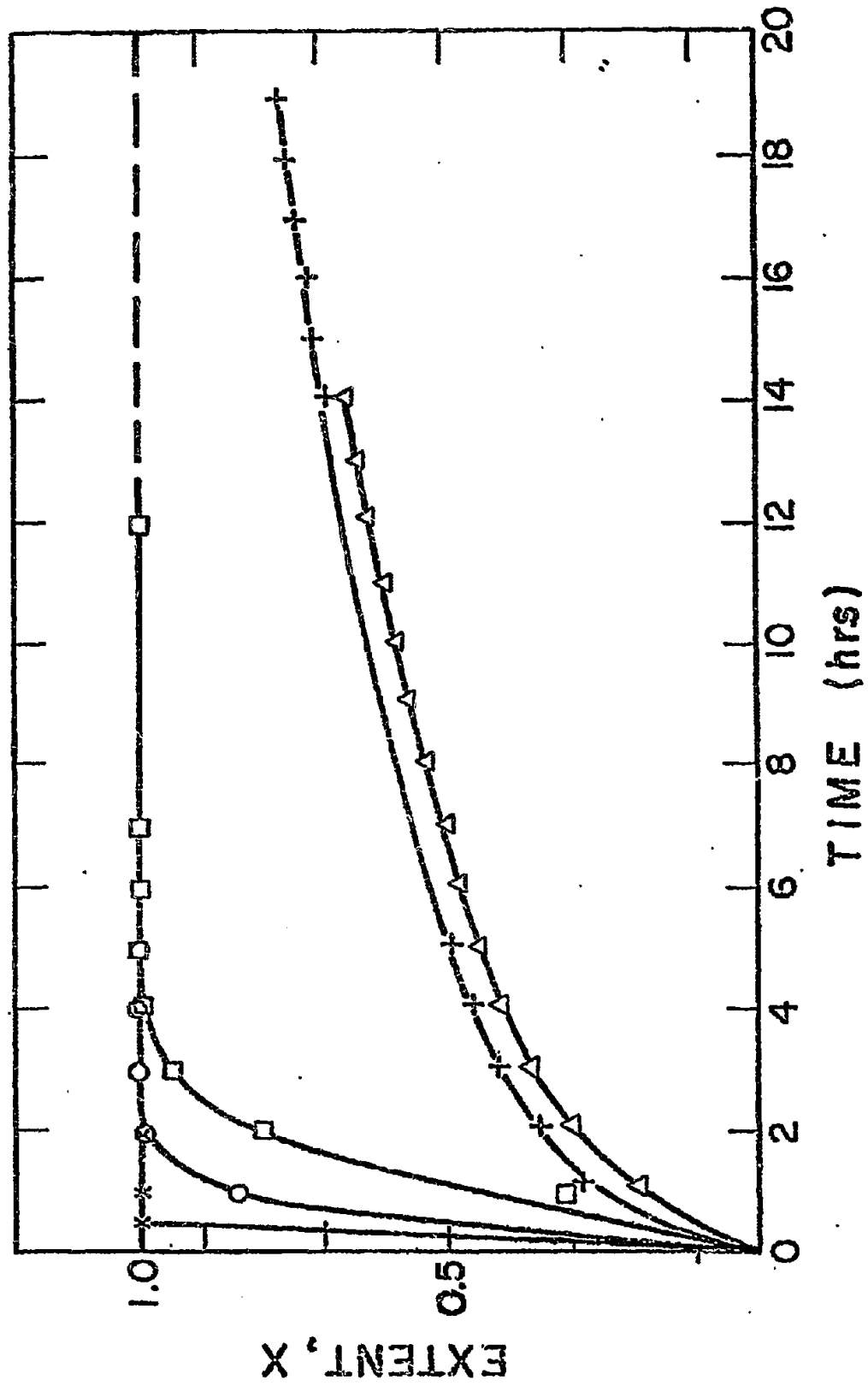


Figure 4.

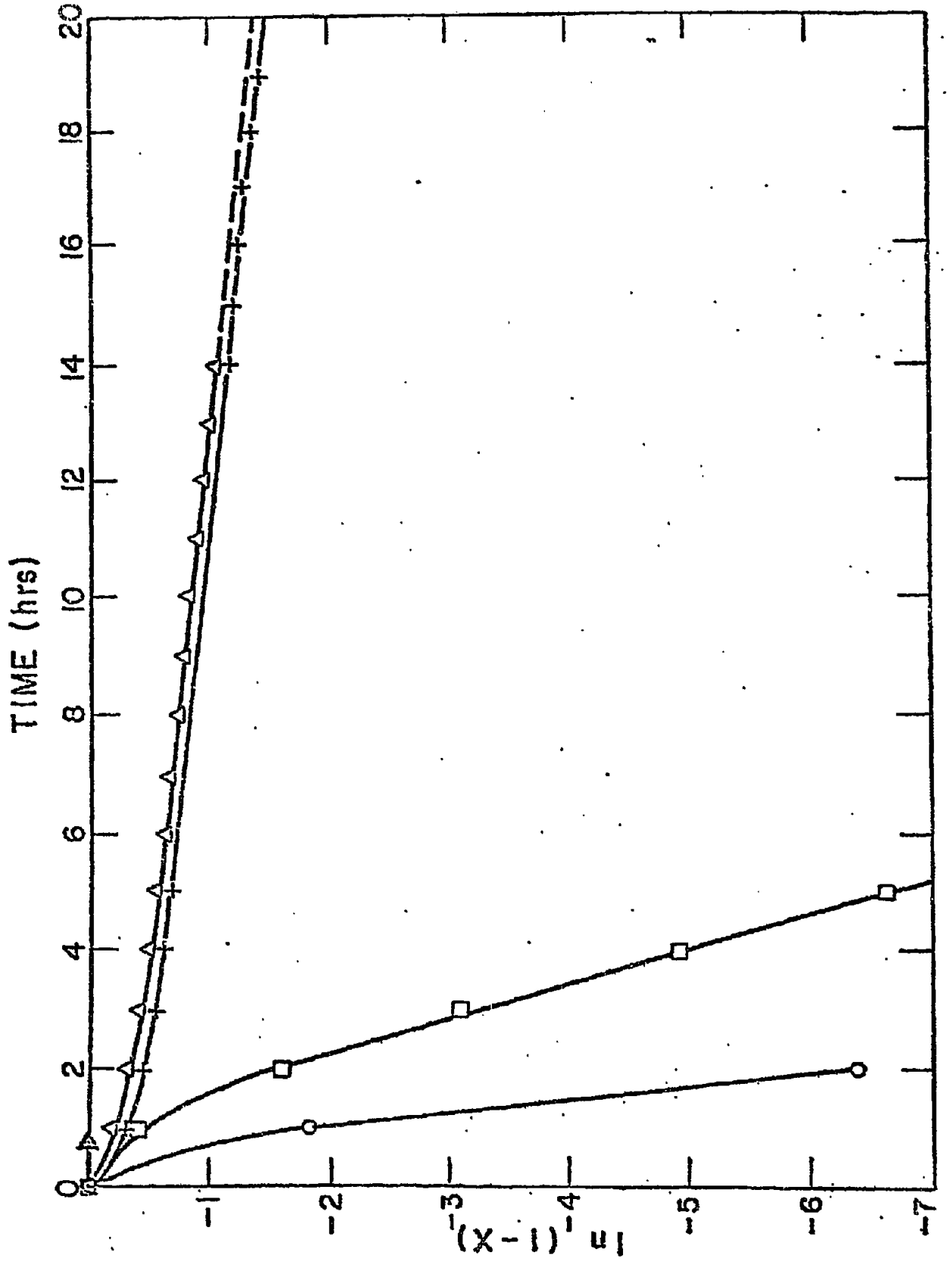


Figure 5



Fig 6

